2009-12-01

Investigation of Velocity Profiles in Anatomically Realistic Renal Artery Flow Phantoms by Physiological Flow Experimentation

Deepa Chari
Technological University Dublin

Recommended Citation

Chari, D.(2009). *Investigation of Velocity Profiles in Anatomically Realistic Renal Artery Flow Phantoms by Physiological Flow Experimentation*. Masters dissertation. Technological University Dublin. doi:10.21427/D7QP5H

Investigation of velocity profiles in anatomically realistic renal artery flow phantoms by physiological flow experimentation

Deepa Chari

M.Sc.

A thesis submitted to the Dublin Institute of Technology for the degree of Master of Philosophy

Supervisors: Dr Jacinta Browne, Dr. Andrew Fagan, Prof. Vincent Toal

School of Physics,
Dublin Institute of Technology,
Kevin St, Dublin 8
Dec 2009

Abstract

Renal Artery stenosis is one of the major causes of curable renovascular hypertension. An early investigation of renal artery stenosis helps in the management of renovascular hypertension by alternative, less-invasive methods such as drug treatments, thereby reducing the risk involved in the surgery. Therefore an early investigation of renal artery stenosis has been always an attractive goal for the physicians.

The renal artery stenosis affects the blood velocity profile in the renal artery. These profiles can be investigated by quantitative Doppler Ultrasound measurements obtained by flow experimentations and can be used as a tool for the identification of renal artery stenosis.

In the present study, the velocity profiles produced in anatomically realistic renal artery wall-less flow phantoms were investigated by physiological flow experimentations. The renal artery flow phantoms mimic renal vasculature anatomically and acoustically as well as representing symmetrical (30%, 50% and 70%) and asymmetrical (25%, 35% and 45%) stenosis conditions. A physiological flow of velocity between 2 – 40 cms^{-1} was produced in each renal artery flow phantom. The blood mimicking fluid (BMF) velocity was determined at regular axial and radial intervals of 1mm, using Siemens Antares Ultrasound system with a broadband curvilinear transducer (C5-2). The physiological velocity profiles in each phantom were investigated. By studying the characteristics of the physiological velocity profiles in the anatomically realistic renal flow phantoms, a greater understanding of renal flow behavior in the normal and diseased conditions can be obtained. These flow characteristics can serve as a basis for identification and quantification of the degree of stenosis. The flow characteristics in the investigated velocity profiles may lead to earlier detection of renal artery stenosis using non-invasive ultrasonic methods.

Subcutaneous fat is a well documented limitation of renal imaging. Recent studies have indicated that the subcutaneous fat introduces an error in the maximum velocity estimation and thereby in the quantification of degree of stenosis. In the present thesis, the effect of a fat mimicking layer on: a) physiological velocity profiles and b) the shape and profile of Spectral Doppler velocity waveforms was studied. The knowledge of how the subcutaneous fat affects the physiological waveforms and thereby the clinical diagnosis is important while using the physiological flow waveforms and the physiological velocity profiles as a criteria for identification of renal artery stenosis.

Declaration

I certify that this thesis, which I now submit for examination for the award of the degree of Master of Philosophy (MPhil), is entirely my own work and has not been taken from the work of others unless cited and acknowledged within the text of my work.

This thesis was prepared according to the regulations for postgraduate studies by research of the Dublin Institute of Technology and has not been submitted in whole or in part for an award in any other Institute or University.

The institute has permission to keep, to lend or to copy this thesis in whole or in part, on condition that any such use of the material of the thesis by duly acknowledged.

Signature   Date 14/4/10

(Deepa Chari)

Acknowledgements

I would like to thank my supervisors Dr Jacinta Browne and Dr Andrew Fagan for their help and for giving me the opportunity to undertake this research with the Medical Ultrasound Physics and Technology Group. In particular I would like to extend a special thanks to Jacinta for her support during the experimental work and for correcting the thesis. I would like to thank Andrew for his comments and suggestions while writing the thesis which helped me a lot to improve my scientific writing skills. I would also like to thank Prof Vincent Toal and Dr John Doran for allowing me to work within School of Physics. I would like to extend my warm thanks to Dr Deirdre King, Louise and John for their constant support and advice during the project. A special thanks to Deirdre for her day to day support and Louise for her help with the SAM system. I would also like to thank my fellow postgraduates in School of Physics and FOCAS for their support during the project especially in the final stages of my thesis work.

I am thankful to Michal Ring and Sean Keane for their assistance with the renal models. I am also very grateful for the help that I received from the School of Physics technicians.

Finally, I would like to thank my husband Mubarak, my mother, my sister Jyoti and my friends for their support. The production of this thesis has been an arduous process and I know without the support and encouragement of family and friends, it would have been substantially harder.

Thank you

List of Abbreviations

1D	One dimensional
α	Attenuation coefficient
η	Fluid viscosity
θ	Angle of insonation
ρ	Density
α	Womersley number
ω	Angular frequency
2D	Two dimensional
3D	Three dimensional
ADC	Analogue to digital convertor
BC	Benzalkoliumcholride
BMF	Blood mimicking material
c	Speed of sound
CAD	Computer aided design
CT	Computed tomography
CTA	Computed tomography angiography
c_w	Speed of sound through water
CW	Continuous wave
D	Diameter
DSA	Digital subtraction angiography
EDV	End diastolic velocity
EC	European Commission
f	Frequency

f_c	Centre frequency of the pulse
f_D	Doppler shift frequency
f_t	Transmitted frequency
f_r	Received frequency
f_R	Resonant frequency
FMD	Fibromuscular disease
IA-DSA	Intra-arterial digital subtraction angiography
IEC	International Electrotechnical Commission
IPEM	Institute of Physicists and Engineers in Medicine
ISB	Intrinsic spectral broadening
L	Length
MI	Mechanical index
MRA	Magnetic resonance angiography
MRI	Magnetic resonance imaging
PI	Pulsatility index
PRF	Pulse repetition frequency
PVA	Polyvinyl alcohol
PVA C	Polyvinyl alcohol cryogel
PSV	Peak systolic velocity
PW	Pulsed wave
Q	Volumetric flow
R	Radius
RAS	Renal artery stenosis
RBC	Red blood cells
RE	Reynolds number
$\mathbf{RE}_{\mathbf{crit}}$	Critical Reynolds number

RAR	Renal aortic ratio
RP	Rapid prototyping
RSR	Renal segmental ratio
RVH	Renovascular hypertension
SAM	Scanning Acoustic Macroscope
SE	Standard error
SV	Sample volume
TGC	Time gain compensation
TMM	Tissue mimicking material
UO	Overall uncertainty
UR	Random uncertainty
US	Systematic uncertainty
US	Ultrasound
VMM	Vessel mimicking material
WBC	While blood cells

Contents

List of Figures

List of Tables

Chapter 1 Introduction

Renal artery stenosis (RAS) is a narrowing of the major arteries that supply blood to the kidneys. The main cause of RAS is atherosclerosis which is characterised as the deposition of atherosclerotic plaque, on the innermost wall of the artery. Approximately 90% of RAS is due to atherosclerosis [1]. Atherosclerotic RAS disturbs the blood flow behaviour, reduces renal perfusion pressure and causes potentially curable renovascular hypertension (a type of secondary hypertension). Renovascular hypertension is present in 1-5% of all cases of hypertension and increases to 16% - 32% in populations selected in a clinical approach [2-3]. The prevalence of atherosclerotic RAS incresases with age and reaches approximately upto 20% in patients with caronary artery disease. Approximately 60 million people suffer from hypertension in the USA alone which highlights the magnitude of the problem. There has been incresed interest on the diagnosis and treatment of RAS as the renovascualr hypertension although low in praportion (1 - 5%) in all hypertensive cases, is a potentially curable type of hypertension. Current evidences also suggest that the atherosclerotic RAS is indicative of the presence of atherosclerotic plaque at other sites in the body such as carotid artery and coronary artery which emphasises the importance of diagnosis of RAS [87]. Further, RAS is a progressive disease and if left untreated could lead to several morbidities such as: progressive renal insufficiency, myocardial infarction, stroke and ultimately death [4]. The surgical treatments which are used to treat advanced cases of RAS are often associated with complications such as trauma or bleeding. Therefore, an early diagnosis of RAS is important as it has a potential to offer various drug treatments, which are less or non-invasive thereby reducing the risks involved in the surgery. The potential gains from treatment make the early diagnosis of RAS an attractive goal for physicians, particularly if it can be achieved with great accuracy and low risks [5].

Digital Subtraction Angiography (DSA) is considered as the 'gold standard' for the diagnosis of RAS [6-7]. It is however, an invasive technique and is associated with inherent morbidity. Consequently, many non-invasive imaging modalities such as Computed Tomography (CT), Magnetic resonance Imaging (MR) and Ultrasound (US) have been developed to evaluate the renal artery stenosis. Amongst the non-invasive imaging modalities used for RAS diagnosis, Ultrasound is the least expensive, does not use ionising radiation and is a widely available technique. Clinical studies involving ultrasound have reported sensitivity in the range of 80% to 97% and specificity varying from 54% to 92% in the diagnosis of RAS [8-10]. In a recent study based on meta-analysis of the sensitivity and specificity information of Duplex ultrasound and DSA, the peak systolic velocity parameter used for RAS diagnosis in Duplex Ultrasound has a sensitivity of 85% and a specificity of 92% [10]. The non-invasive nature, ionising radiation free character, widespread availability, good accuracy in RAS diagnosis and low cost make Duplex ultrasound an attractive option for the diagnosis of RAS [5].

Atherosclerotic RAS affects the blood flow and thereby the velocity profiles in blood vessels [11]. An understanding of the disease progression in the renal arteries can be obtained by studying the velocity profiles at different stages of disease (stenosis) [13]. Mapping of the velocity profiles at different stages of disease (stenosis) is therefore very important. The current knowledge in this area is contributed by *in-vivo* experimentation or clinical studies, *in-vitro* experimentation using flow phantoms and by developing computational fluid dynamic models. Clinical trials or *in-vivo* experimentation to study the flow profiles are simple and straight forward. However, these trials are often expensive to run, are time consuming and require the involvement of a large number of patients for statistical analysis. To study the blood flow dynamics in simple as well as complex arteries, a few computational fluid dynamic models have been developed - these have been reviewed elsewhere [12]. The main problems reported in the development of fluid dynamic models of complex arteries include difficulties in representing a) complex pulsatile flow b) mechanical properties of vessel wall and c) complex arterial structure involving curvatures, bifurcations and constrictions. Only a few models described in the literature have incorporated the pulsatile flow characteristics and certain complex geometrical features of the arteries such as curvature and constriction successfully [13-15]. Furthermore, these complex models require a lot of computational time. Additionally, a high degree of expertise is needed to interpret the information and understand the flow behaviour in the human arteries, based on this type of information. *In-vitro* experimentation using flow phantoms is a good option to investigate the velocity profiles in complex shaped and diseased arteries [16-17]. Developments in rapid prototyping techniques (RP) and computer aided designs (CAD) have allowed the anatomical reconstruction of complex, three dimensional (3D) arterial geometries from the medical 3D data obtained from either MR or CT data sets. Also, a pulsatile flow can be simulated in these anatomical flow phantoms using computer controlled pump systems [17]. The potential of the anatomically realistic flow phantoms to represent complexities in the arterial structure and to simulate physiological flow have made such flow phantoms ideal for *in-vitro* flow experimentation and for velocity profile investigation studies. These experiments can be performed in the laboratory and velocity information can be obtained, across the entire region of interest and mapped as a velocity profile.

Many different types of ultrasound flow phantoms have been developed to date, an in depth review has been carried out by Hoskins [17]. Ultrasound flow phantoms are readily reproducible in the laboratory. They can represent complex vasculature geometry accurately and can also represent the diseased conditions. Also, the flow parameters can be standardised in the laboratory before the flow experiments are carried out and then the velocity profiles can be investigated by flow experimentation [17]. In spite of several advantages of ultrasound flow phantoms in the studies investigating velocity profile, to date, due to the unavailability of renal flow phantoms, no *in-vitro* studies in an anatomically realistic phantom with physiological flow rate have been carried out. Recently, anatomically realistic wall-less renal artery flow phantoms representing a range of symmetrical stenosis were been developed by King [18]. These renal artery phantoms have shown considerable potential for use as a tool for steady flow experimentation. However, no studies using these phantoms involving physiological flow have been carried out. It is preferable to perform detailed flow experimentation using these renal flow phantoms with physiological flow, since, physiological flow is more reflective of the clinical situation and can therefore provide a better understanding of physiological flow behaviour in normal and diseased renal artery. Furthermore, in the clinical situation, the occurrence of asymmetric atherosclerotic stenosis is more common since atherosclerosis of the vascular wall does not spread uniformly but more often cause eccentric and irregular narrowing of the vessel lumen. Therefore, from a clinical perspective, a detailed study of physiological flow profiles in renal artery flow phantoms representing a range of asymmetrical stenosis would be important. The investigated flow profiles could then be used to identify the key characteristics of the flow in presence of a particular degree and type of stenosis. A detailed study of the systolic velocity profiles produced in normal and diseased renal artery flow phantoms could also be used as a basis to quantify the degree of stenosis in terms of flow characteristics. Therefore the measurement of physiological flow profiles could be used as a tool for

RAS identification and could also serve in the accurate characterisation of degree and topography of stenosis.

As the detection and quantification of a stenosis often forms the basis of a surgical intervention, the accuracy in the diagnosis and quantification of renal stenosis is very important. Peak systolic velocity is used as a key parameter for the diagnosis and identification of hemodynamically significant RAS in most Duplex ultrasound examinations [19] [10]. Therefore, knowledge of the factors affecting peak systolic velocity measurement is essential. Several factors affecting maximum velocity estimation have been identified, studied in detail and reported in the literature [20-23]. The presence of subcutaneous fat overlaying the renal arteries is a well known limiting feature in renal imaging. However, the studies investigating the effect of subcutaneous fat on maximum velocity estimation are very limited in number [24]. The inhomogeneous nature of fat and the lower speed of sound of subcutaneous fat (compared to that assumed by the ultrasound scanner) lead to an inhomogeneous tissue path, which has the potential to produce refraction of the ultrasound beam. Subcutaneous fat can also cause ultrasound beam distortion. Furthermore, it can cause significant attenuation of ultrasound beam thereby affecting the physiologic flow waveform. Browne *et al.* have investigated the effect of subcutaneous pig fat on the image quality and have also studied whether this effect could be reduced with newer imaging modalities [25]. Recently, King *et al.* investigated the effect of subcutaneous fat on maximum velocity estimation using both a string phantom and a simple vessel flow phantom using an overlying fat mimicking olive oil layer [24]. The presence of subcutaneous fat can lead to an overestimation of the maximum velocity and thereby, introduce an error in the quantification of degree of stenosis. Furthermore, the thickness of abdominal subcutaneous fat varies from patient to patient. Therefore, a detailed study to investigate the effect of varying thicknesses of subcutaneous fat on the magnitude of the error introduced in the systolic and diastolic velocities would be beneficial. The effect of this subcutaneous fat layer on systolic and diastolic velocities, determined across the entire renal artery in an anatomical model, could provide a greater understanding of the behaviour of physiologic flow profiles in presence of subcutaneous fat layer. The physiological waveform, captured in the Pulsed Wave (PW) Spectral Doppler mode, may be used to determine the peak systolic velocity. Therefore, the effect of a subcutaneous fat on the shape and the profile of the physiological flow waveform is important to study. A comparative study of the profiles of physiological waveforms can be performed to gain an understanding of how subcutaneous fat affects the intensity and velocity information and thereby, the clinical diagnosis obtained from this data.

The aims of this MPhil work discussed in the thesis were 1) to investigate the physiological velocity profiles in anatomically realistic renal artery flow phantoms representing a range of symmetric or asymmetric stenosis, and 2) to study the effect of subcutaneous fat of different thicknesses on a) the physiological velocity profiles and b) features of the physiological waveform.

Chapter 2 Theory and literature review

This chapter is devoted to the discussion of the theory of ultrasound and the key concepts which are relevant to the work described in this thesis. Section 2.1 describes the theory of Ultrasound (US) imaging and the Doppler effect in diagnostic ultrasound imaging. Section 2.2 discusses the physics associated with blood flow dynamics in human arteries. Section 2.3 is a literature review of a) the different imaging techniques used for renal artery stenosis (RAS) investigation b) the different flow phantoms used for the *in-vitro* flow studies in US imaging. This section also presents a review of the studies of how an overlying fat layer can effect the maximum velocity estimation. Finally, the aims and the objectives of the thesis are presented in section 2.4

2.1 Ultrasound Imaging and the Doppler Effect

Ultrasound

Ultrasound waves are high frequency mechanical waves and medical imaging systems use ultrasound waves in the range of 2-20 MHz. The transducer probe is the main component of every medical ultrasound imaging system. The transducer consists of piezoelectric crystals which exhibits the piezoelectric effect. The piezoelectric crystals when subjected to an alternating electric current vibrate rapidly and these vibrations produce ultrasound waves. Conversely, when ultrasound waves are incident on the piezoelectric crystal, the acoustic energy of these waves is converted to an electric signal. Therefore, the same piezoelectric crystals can be used to transmit and receive ultrasound waves. The transducer probe is encased in a plastic case for mechanical safety. The transducer consists of a dampening layer on its back face which dampens vibrations quickly after excitation and a single or multiple impedance matching layers on its front face which reduce the magnitude of reflection coefficient generated at the interface between the transducer face and soft tissue, thereby, improving the transmission of ultrasound waves into the body. The transducer, while in use, is acoustically coupled to the body using a coupling gel to eliminate air bubbles between the transducer output face and the body surface.

The ultrasound waves propagate through the body until all of their energy is dissipated in the tissues. These waves undergo four possible interactions with the tissue: reflection, refraction, scattering and absorption, the relative amounts of each depending upon the physical characteristics of the tissue. When the ultrasound waves encounter tissue interfaces and inhomogeneties, some of the ultrasound energy is reflected back towards the transducer face the magnitude of the reflection depending upon the acoustic impedance (z) of the tissues either side of the boundaries. The amount and type of reflection of the ultrasound waves also depend on the size of the interface and the wavelength (λ) of the ultrasound wave propagating into the tissue. Therefore, at the large area interface where the wavelength of the transmitted ultrasound waves is much less than the object size, specular reflection occurs whereas, at the intermediate size interfaces where (λ) is about the same size of the object, the ultrasound beam is scattered (Stochastic scattering). The red blood cells (RBCs), suspended in the blood plasma, typically have a diameter of between 5 and 7 μm which is very small in comparison with the wavelength of ultrasound waves and cause weak back scattering (Rayleigh scattering) of ultrasound waves in all directions.

A two dimensional (2D) B-mode image is constructed from the echoes which are generated by the reflection of ultrasound waves at these tissue interfaces and scattering from the inhomogeneties with the tissues. The images are constructed using a pulse-echo technique. In this technique, a single pulse of ultrasound is transmitted into the body and the echoes returning from the tissue interfaces are detected by the piezoelectric crystals in the transducer. The image is formed by sweeping the ultrasound pulse through the plane of tissue and repeating the echoes detection procedure in the entire plane. The detected echoes are converted into electrical signals which further undergo signal processing to form a 2D image. Each echo in the B-mode image is represented as a point. The position of the point in the B-mode image indicates the position of its reflector in the body and the intensity of the point (represented with different shades of grey) is related to the amplitude of the reflected echoes.

The renal vessels can be visualised directly in B-mode. In the diagnosis of renal artery stenosis, visualisation of the renal arteries in B-mode is important.

Doppler Ultrasound

The Doppler Effect is defined as a phenomenon in which a change in frequency is observed due to the relative motion of the source or the observer or both with respect to each other. When an ultrasound wave travels through the blood, the transducer which is the source as well as the observer is stationary while the RBCs in the blood are moving with respect to both the source and the observer. The ultrasound waves travelling through blood encounters the moving RBCs and scattering occurs. The Doppler shift, in the reflected frequency of the ultrasound wave, due to scattering from the moving RBCs can be calculated using a modified Doppler shift equation (Equation 2.1) which also gives the blood flow velocity information.

$$F_d = \frac{2 f_t v \cos(\theta)}{c} \qquad \text{Eq. (2.1)}$$

$$F_d = f_t - f_r \qquad \text{Eq. (2.2)}$$

where F_d is Doppler shifted frequency, f_t is the transmitted frequency, f_r is the received frequency, v is velocity of the target (blood), θ is insonation angle (angle between ultrasound beam and direction of the target's motion) and c is speed of ultrasound wave in the tissue. The $v\cos(\theta)$ term represents the component of velocity in the direction of the ultrasound beam. The average speed of the ultrasound wave in the tissue is 1540 ms^{-1}.

The blood flow information can be displayed in several different forms using different modes such as continuous wave (CW) or pulsed wave (PW) spectral Doppler, Duplex Doppler and Colour or Power Doppler.

Spectral Doppler

In spectral Doppler, the velocities determined from the Doppler shifted frequencies are plotted with respect to time. The CW Doppler spectral Doppler systems use two piezoelectric crystals – one acting as a transmitter and the other as a receiver. The transducer transmits and receives ultrasound waves continuously using the two piezoelectric crystals. A portion of the ultrasound waves reflected and scattered by the moving and stationary particles is reflected back towards the piezoelectric crystals of the transducer which re-converts the acoustic energy into electrical energy. This signal is further amplified by a radio frequency amplifier and mixed with a reference signal from the master oscillator. The low pass filtering of the mixed signal separates the Doppler shifted frequencies from the mixed signal which is then high pass filtered to remove high-amplitude low-frequency signals from the stationary targets and amplified further to obtain the demodulated signal [26]. Because of the continuous mode of transmitting and receiving, depth resolution is not possible in CW system [26]. In PW spectral Doppler systems, the same piezoelectric crystal of the transducer transmits and receives short pulses of ultrasound at regular intervals decided by an operator adjusted delay. PW Doppler systems require additional circuitry to gate the transmitted and received signal at appropriate time and to sample and hold the demodulated signal [26]. The demodulation process is similar to the CW system as explained above. In these systems, the delay determines the approximate depth from where the signal is received. The location and size of the sample volume can be adjusted depending upon region of interest. The main drawback using PW system is that the maximum velocity detection is limited by the finite pulse repetition frequency (PRF) employed and is subject to the nyquist limits otherwise aliasing occurs [26]. The maximum Doppler shifted frequency, a PW system is able to detect is the half of PRF. While visualising the vessels located deep within the body, the PRF must be decreased so as to allow the ultrasound pulses sufficient time for the complete journey in the body. With this reduced PRF, only the lower velocities may be detected in such vessels. In particular, this problem is severe for the velocity measurement in presence of severe stenosis where the blood flow velocities are highly elevated [26].

Duplex scanning combines PW Doppler mode with B-mode imaging. Using duplex Doppler, quantitative information (such as blood velocity) can be obtained from Doppler shift signal extraction from known anatomical location imaged in B-mode. Renal artery Duplex scanning allows anatomic assessment of the renal arteries by direct visualisation through B-mode imaging as well as functional assessment on the basis of PW Spectral Doppler measurements of various hemodynamic parameters.

Colour Doppler

In colour Doppler imaging, colour encoded velocities (obtained from mean Doppler frequency within each sample volume) are overlayed on the B-mode images. Each line of the image is made up of multiple adjacent sample volumes. The Doppler signal from these samples volumes is processed simultaneously [27]. For detection of mean Doppler frequency within the sample volume at least two pulses are required to be transmitted along each line. A typical colour Doppler image is formed using between four and sixteen pulses directed towards each line of sight. The requirement of several pulses per line to produce the colour image compared with a minimum of one in B-mode image reduces the frame rate (the rate at which image is updated) in comparison with B-mode image [28]. The frame rate can be improved by limiting the dimensions of colour box (the region for which the colour coded flow is displayed within the displayed B-mode image) to the region of interest (ROI) which allows fewer ultrasound pulses to be sent per colour frame thereby increasing the frame rate.

The colour encoding in colour Doppler images depends on the velocity and direction of flow relative to the transducer. Therefore, the colour Doppler technique can provide an estimate of mean velocity towards or away from the transducer. The variance is also high compared to the spectral Doppler due to the limited number of the transmitted pulses and their length. A brief review of colour Doppler imaging has been published by some researchers [26-28].

Power Doppler

Power Doppler imaging is an amplitude based colour flow mapping technique. In power Doppler, the power of the Doppler signal backscattered from blood is converted to a colour map and overlaid on the B mode images [26]. The power Doppler mode can be efficiently used for the visualisation of blood flow in small vessels and near vessel walls due to the following reasons. Firstly, the power of the background noise is very small compared to the power of the Doppler signal backscattered and distributed uniformly. Therefore, the power gain can be increased considerably compared to the colour gain in colour Doppler mode. Aliasing is not a problem in the power Doppler imaging as the pulse repetition frequency does not effect the total power of the signal and therefore significantly lower sampling rate (pulse repetition frequency) can be used which results in improved sensitivity in the visualisation of slow velocity flow near the vessel walls. Also power unlike frequency is angle independent and therefore the changes in the power Doppler image due to the Doppler angle are not prominent. A brief review of power Doppler imaging has been published by following researchers [26] [28].

Three dimensional (3D) Ultrasound imaging

The recent and ongoing advancement in transducer technology and digital processing have made 3D representation of arterial vasculature and the flow field possible [27]. The 3D Ultrasound imaging is based on reconstruction algorithms where the 3D images are assembled from a series of 2D images produced by 1D arrays of piezoelectric crystals of transducer. The set of 2D images are obtained by the operator either by a free-hand sweep of the transducer manually i.e. by moving the transducer over the surface of patient in the region of interest or by mounting the transducer on a mechanical assembly (mechanical localisers) and translating the transducer mechanically. The position and orientation of the transducer is measured by sensors with respect to a frame of reference which is fixed in relation to the patient, simultaneously, while acquiring the 2D images. By appropriate calibration of the spatial relationship in the system finally a 3D image is assembled. The mechanical assembly have following advantages: Firstly, the transducer can be translated in a linear fashion along the patient's skin as well as precise tilting of transducer is possible, tilting allowing 3D colour or power Doppler imaging. Further, the intervals between the digitised images can be adjusted for proper sampling, thereby making the reconstruction of the images more efficient. A brief review of 3D ultrasound imaging has been published by following researchers [91] [92]. The main clinical applications of 3D Ultrasound imaging are in gynaecology (for 3D fetal scanning) or cardiology (for measurement of chamber volume and wall motion) [27], but promising results have also been obtained in other areas such as vascular ultrasound e.g. for the measurement of the degree of arterial stenosis, vascular characterisation and mapping of blood flow patterns [89] [90].

2.2 Blood Flow Dynamics

Blood is a complex mixture consisting of RBCs, white blood cells (WBC) and platelets suspended in plasma. The RBCs are semisolid particles of diameter between 5 and 7 µm typically which comprises about 45% of the total blood volume. In capillaries defined as microvessels measuring 5 – 10 µm diameters, the blood does not exhibit constant viscosity at all flow rates. Newtonian fluid has a constant viscosity which is independent of shear rate at a fixed temperature. Therefore blood behaves as a non-Newtonian fluid in capillaries. The non-Newtonian behaviour of blood was studied by *in-vivo* and *in-vitro* studies where an axial accumulation of RBCs in arterioles was reported in one study [29] and in another; reduced particle concentration across walls of a 3 mm diameter vessel at low velocity was reported [30]. Both *in-vivo* and *in-vitro* observations have supported the non-Newtonian behaviour of blood in capillaries and small vessels (< 3 mm diameter). The arteries are however comparatively larger in diameter than capillaries. In large arteries, at high shear stress, the effect of viscosity dependence is not significant and the blood can be assumed to behave as a Newtonian fluid with a constant viscosity of 0.04 poise [29].

Several fluid dynamic models have been developed to explain (analytically) the steady flow behaviour in a tube [17] [29] [12]. Most of these models were based on the approximation that arteries are mechanically stiff and large in diameter and the blood flow in arteries was approximated as a Newtonian flow fluid in a long rigid tube. The basic model developed by Poiseuille [17] described the blood flow in a straight rigid artery using the following analytical expression:

$$Q = \frac{\pi R^4 (P_1 - P_2)}{8\mu L} \qquad \text{Eq. (2.3)}$$

where Q is the flow rate, R is the radius of the tube, $(P_1\text{-}P_2)$ is the pressure difference measured across the tube of length L and μ is the coefficient of viscosity [12]. The velocity at any point r in the rigid tube was expressed using equation 2.4,

$$V(r) = V_m \left(1 - \tfrac{r^2}{R^2}\right) \qquad \text{Eq. (2.4)}$$

where V_m is the maximum flow velocity

The Poiseuille's equation is valid only for steady, fully developed laminar flow. The profile of such a steady, fully developed laminar flow passing through a straight (rigid) artery was observed to be parabolic [17].

The effect of the presence of an occlusion or constriction in a rigid tube on the flow behaviour has also been studied analytically using Poiseuille's rigid tube model [12]. In the Poiseuille's equation, the flow rate (Q) is directly proportional to the fourth power of the radius of the tube which illustrates that the diameter of the tube is an important factor in determining the behaviour of the flow in the tube. In the presence of constriction in a rigid tube, the tube radius decreases and the flow velocity at the obstruction increases in order to maintain a constant volume flow rate through the narrowed area. The magnitude of the flow velocity depends upon the extent of the constriction. Immediately after the constriction, the tube resumes its original (normal) diameter, resulting in a reduction of the flow velocity by the distribution of flow energy across the entire radial cross section. Areas of flow reversal areas may be found immediate distal to the obstruction. The orderly pattern of the laminar flow thus gets disturbed in presence of constriction and results in nondeterministic and unorganised flow referred to as 'turbulence'. A non-dimensional parameter Reynolds number (Re) can be used to predict if the flow is streamline or turbulent and is defined as follows:

$$R_e = \frac{\rho v D}{\mu} \qquad \text{Eq. (2.5)}$$

where ρ is the density of the fluid, v is mean velocity of the flow, D is diameter of the vessel and μ is coefficient of viscosity [12].

The critical Reynolds number (R_{ecrit}) is the R_e at which the flow becomes turbulent. In relation to human arteries, the obstruction can occur due to deposition of plaque on the inner wall of the arterial wall reducing the lumen diameter. The R_{ecrit} for the renal artery is 700 [18].

In case of human arteries, the steady flow approximation is not valid since the blood flow in arteries is a complex pulsatile flow; its pulsatility is due to the cyclic flow nature of heart pump. The pulsatility generates complex flow profiles. Furthermore, the arteries are viscoelastic so the rigid wall approximation is not a valid approximation and therefore can not be used to describe the pulsatile flow behaviour in arteries.

It is very important to study the behaviour of flow entering the arteries. The blood flow at the origin of arteries is not fully developed and is similar to an entrance type of flow. The velocity profile in the entrance region is flat/blunt near the center and a large velocity gradient at the vessel walls due to frictions forces. As the flow propagates further, the viscous effect propagates towards the center and the accelerating centreline velocity accelerates in order to keep the flow rate constant resulting in a parabolic flow profile [26]. The flow in the entrance region is expressed using the Reynolds number (*Re*) and a second non-dimensional parameters called Womersley number (α) defined as

$$\alpha = R\sqrt{\frac{\omega}{\mu}} \qquad \text{Eq. (2.6)}$$

where R is tube radius, ω is angular frequency of the oscillations and μ is kinematic viscosity [31].

For lower value of α (1-10), viscous forces dominates the flow resulting in parabolic velocity profiles at the entrance region and the entrance length beyond which the flow is laminar is decided largely on the basis of R_e. For higher α (>10), the unsteady inertial forces are dominant indicating the inviscid (constant viscosity) nature of the fluid [29]. The velocity profile in this case is blunt at the central region with a steep velocity gradient at the vessel wall. The Womersley number for ascending aorta, abdominal aorta, inferior vena cava and main pulmonary artery are 21, 12, 17 and 20 respectively indicating that the fluid flow in most of the medium and large arteries is inviscid [12]. The flow at the origin of the arteries thus may or may not be fully developed and depends upon the magnitude of Reynolds number (R_e) and Womersley parameter (α). Many of the arteries being short, the entrance flow conditions strongly influence the flow field further downstream and affect the velocity profiles.

Most of the arteries in the human body are curved. At the curvature, the fluid flow experiences a centrifugal force and may develop secondary flow. The nature of the secondary flow depends upon the diameter of the artery, radius of curvature, viscosity and density of the blood and also on the flow behaviour before the curvature. The secondary flows affect the flow behaviour at the curvature and thus affect the flow profiles at the curvature and further downstream. The flow behaviour in the curved tube is described using a parameter called Dean Number [12] defined as following:

$$\text{Dean number} = 4R_e \cdot (2\delta)^{1/2} \qquad \text{Eq. (2.7)}$$

where R_e is Reynolds number and δ is given by,

$$\delta = \frac{\text{radius of tube cross setion}}{\text{radius of curvature}} \qquad \text{Eq. (2.8)}$$

If the flow entering in the curvature is fully developed, the high velocity central fluid layer with more inertia tries to follow its same straight line path and hence resists more the effect of centrifugal force compared to the low velocity flow near vessel wall. The result is a shift of higher velocity fluid layer towards the outer vessel wall resulting in a skewed profile (skew towards outer wall). In case of the flow entering at the curvature that is not fully developed, the flow across the cross section has more or less the same inertia. At the curvature, the pressure at the outer wall increases. In order to balance this pressure, the kinetic energy of the flow at the outer wall decreases with the higher velocity layers shifting towards the inner wall. In this case, the skew in the velocity profile at the curvature is towards the inner wall. The transient nature of the pulsatile flow at the entrance region (based on the magnitude of the Womersley, Reynolds number) and the arterial wall distensibility further complicates the flow behaviour at the curvature and thereby the velocity profiles [26].

Several numerical studies in which fluid dynamic models were developed to describe the complex pulsatile flow behaviour in straight as well as curved arteries have been reported in the literature [15] [14] [12]. These numerical models were based on solutions of the Navier-Stokes and continuity equation (expressed in cylindrical co-ordinate system) to obtain velocity and pressure values at every point in the flow and describe the flow numerically. Some of these models incorporate higher degrees of complexities such as elastic walls, viscoelasticity of the arterial walls and constriction of the tubes to mention just a few [15] [12]. The numerical solutions describe the flow quantitatively and are useful to study the pulsatile flow in arteries. However, these numerical solutions are very complex and need expertise to interpret the flow profile information from these solutions. Further, the other factors which need to be considered are that the arteries age and their performance under hemodynamic stress also changes with time. Incorporating such conditions in numerical model is difficult. Finally, the renal arteries incorporate a curvature and in the case of a diseased renal artery, the stenosis is quite often located in the proximal end of renal artery just before the curvature. The complex geometry of curvature and the stenosis would certainly have an impact on the velocity profile. Given these considerations and limitations of the modelling, experimental studies to investigate such complex pulsatile flow profiles in the arteries are thus the preferred approach. The study of such complex pulsatile velocity profiles investigated in normal and diseased renal arteries by experimental techniques have a potential to provide understanding of the disease progression in this important artery.

2.3 Literature review

2.3.1 RAS investigation using different imaging techniques

Renal artery stenosis (RAS) is the narrowing of the lining of the main arteries that supplies the kidney. These (renal) arteries branch from aorta on either side and extend to the each kidney. The mean maximum diameter of renal artery lumen is about 5-7 mm for a healthy adult. Before reaching to the hilus of the kidney, each artery divides into three to four branches. In the atherosclerotic RAS, the atherosclerotic plaque is deposited on the innermost wall of renal arteries resulting in the reduction of the arterial lumen and thereby affecting the blood supply to the kidneys. Figure 2.1 shows the deposition of atherosclerotic plaque on the innermost wall of the right renal artery.

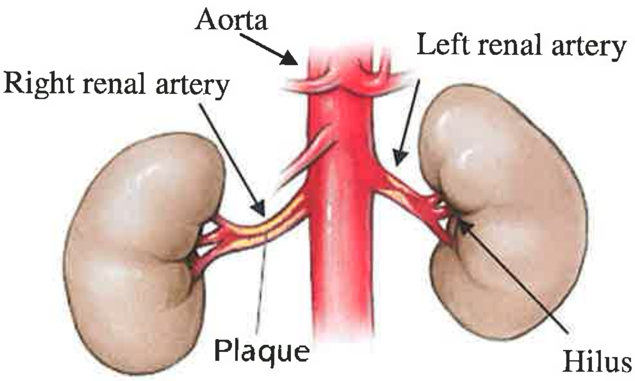

Figure 2.1 Deposition of atherosclerotic plaque on the innermost wall of the right renal artery. (Image adapted from http://www.healthsystem.virgenia.edu/ internet/vascular/ images/renal_arteries)

RAS is progressive in nature and if remains untreated can lead to end stage renal failure. Depending on the degree of narrowing (extent of stenosis) of renal arteries; patients can develop secondary hypertension- renal vascular hypertension (RVH). An early investigation of RAS is of clinical interest as RVH is curable type of hypertension [32] [33] [10] [4]. The different imaging modalities used for RAS investigation includes Intra-arterial digital subtraction angiography (IA-DSA) which is an invasive technique and duplex ultrasound, helical computed tomography angiography (CTA) and magnetic resonance angiography (MRA) all of which are non-invasive techniques. A review of these modalities is presented in this section.

Intra-arterial digital subtraction angiography (IA-DSA)

IA-DSA is considered as a gold standard for anatomical investigation of renal artery stenosis [7]. The technique involves a radiographic imaging system which obtains images of arteries before and after the injection of contrast agent. Using sophisticated image subtraction and processing algorithms, the images of arteries alone are obtained by subtracting the images of structures not containing the contrast agents. DSA images of the arteries are easy to interpret and therefore analyse the extent of stenosis. The technique however has several limitations for example it does not provide accurate characterisation and as a result has not been widely used for identification of blockages of lower than 70% [10]. Furthermore, the technique further can provide only anatomical information and no quantitative information such as flow velocity or pressure gradient developed due to stenosis can be obtained, so the functional implications of stenosis can not be studied. The technique, being invasive and involving use of contrast agents, is associated with several surgical complications such as bleeding, anaphylaxis and contrast material- induced nephropathy with a considerable complication rate of 2%-10% [10]. The invasive nature and associated surgical complications and the cost of diagnostic work-up limit the use of IA-DSA technique as a screening and surveillance tool for RAS [9].

Computed tomography angiography (CTA)

CTA is a non-invasive technique used for the visualisation and accurate assessment of renal arteries [34]. CTA can be used for patients with pacemakers, defibrillators and metal stents or implants (excluded from imaging using magnetic resonance imaging). CTA has an overall sensitivity of 64% to 94% and a specificity of 56% to 93% for the detection of RAS compared with IA-DSA [8] [32] [4]. The main disadvantage of the technique is that it involves the use of ionising radiation. Also it uses the iodinated contrast agent which may be nephrotoxic thus limiting the use of the technique in patients with renal insufficiency [34]. The long post-processing time (30-90 minutes), inability to image persons who weight more than 125 kg and a general tendency of false positive results (mainly due to overlying tissue artifacts and incomplete opacification of renal arteries) are other disadvantages of CTA [35].

Magnetic resonance angiography (MRA)

MRA is a non-invasive technique that allows direct visualisation of the renal arteries without the use of ionising radiation. The renal vessel image can be imaged in any plane providing more information about the morphology of the vessel by viewing it in the most optimal plane. Contrast–enhanced MRA involves use of a gadolinium-based contrast agent injected intravenously. The technique has been reported to be very useful for accurate assessment of the renal vasculature and also provides important hemodynamic flow information which is less-operator dependent compared to Doppler Ultrasound [36] [4]. Contrast-enhanced MRA has an overall sensitivity of 62% to 94% and a specificity of 70% to 84% in RAS investigation compared with IA-DSA [8] [32] [4]. Although the gadolinium contrast media is safe in most of the cases, studies have reported some adverse reaction to gadolinium up to 0.01% [37]. A serious adverse reaction called nephrogenic systemic fibrous, possibly resulting from exposure to the gadolinium contrast agent, has also been reported [38] [39]. Non-contrast MRA has been reported with a sensitivity of 78% and a specificity of 91% in RAS investigation compared with IA-DSA [33]. The limitations include: difficulties in visualisation of accessory renal arteries and overestimation of stenosis. Furthermore, patients with implants and claustrophobia can not be imaged using the MRA technique and the technique is relatively expensive.

Ultrasound (US)

Ultrasound is a non-invasive imaging modality which is widely used for evaluation of renovascular diseases. Duplex ultrasound which uses combination of B mode and Doppler mode blood flow measurement can be used to obtain the anatomical information of the renal arteries through B mode images as well as quantitative information such as velocity of the blood flow in the renal arteries using Doppler measurements. The technique is free from ionising radiation, inexpensive and widely available. US can be used for patients with stents as the ultrasound transmission through stents does not cause artifacts affecting clinical diagnosis. Ultrasound has an overall sensitivity of 80% to 97% and a specificity of 54% to 92% for the detection of RAS compared with IA-DSA [8-10]. The primary limitations include the large operator dependency, difficulty in visualisation of vessels in obese patients due to subcutaneous fat or in patients with intervening bowel gas, decreased sensitivity in detection of multiple stenoses downstream to the densely calcified first stenosis [40].

Amongst all the modalities used for RAS investigation described above, the ideal modality for RAS screening should be non-invasive, free from ionising radiations, relatively expensive, readily available and have good accuracy (sensitivity and specificity > 90%) in the identification of stenosis. Duplex ultrasound satisfies most of the criteria are hence is largely being used as the first line method for renovascular disease evaluation [41].

Clinical parameters used for RAS investigation in Ultrasound imaging modality

The diagnosis of RAS using Ultrasound imaging is primarily based on the information of velocity of blood flow, as the blood flow velocity increases (in order to maintain the flow rate constant when the area of cross section is reduced) at the stenosis. The extent of stenosis can be identified on the basis of maximum velocities measured at stenosis. The primary parameters used for the diagnosis of renal artery stenosis includes peak systolic velocity (PSV) of the main renal artery, a ratio of the peak systolic velocities of renal artery to that in the aorta (RAR), and pulsatility index (PI) calculated using systolic and diastolic velocities of the renal blood flow (in the main renal artery). The pulsatility index value assesses the conservation of pulsatility in the flow. PSV > 180 cms^{-1} has been reported to have an overall sensitivity of 83% to 95% and a specificity of 89% to 90% for the identification of "angiographic stenosis" (greater than 60% stenosis) [42-43]. RAR > 3.5 has been reported to have an overall sensitivity of 92% to 95% and a specificity ranging from 62% to 90% [42] [44].

The other parameters used for the identification of hemodynamically significant (≥50) RAS include: renal-renal ratio (RRR) – this is ratio of PSV measured at the proximal or mid segment and at the distal segment of the renal artery with a threshold value of 2.7 for an angiographic RAS > 50% [45]; resistive index (RI), which is the ratio of minimum diastolic and maximum systolic velocity with a cut-off value of 0.80 (normal RI < 0.70). the distal renal pressure to aortic pressure ratio (P_d/P_a) < 0.90 for a RAS > 50% [6]; and renal –segmental ratio (RSR)- which is a ratio of peak systolic velocity in the renal artery to that in the segmental artery with a cut-off value of 4.0 [46]. An end diastolic velocity (EDV) of 150 cms^{-1} or greater has also been reported signifying an extreme stenosis of 80% or greater [34].

Amongst all the criteria and parameters defined for RAS investigation, the most widely accepted criteria for identifying hemodynamically significant RAS are a) PSV greater than 180-200 cms^{-1} b) RAR ratio of 3.5:1 along with post stenotic turbulence [8] [9] [47].

Figure 2.2 below represents the percentage (degree) of stenosis and corresponding PSV relation as per the guidelines set in Institute of Physics and Engineering (IPEM), vascular Laboratory Practise Manual 2004 [48].

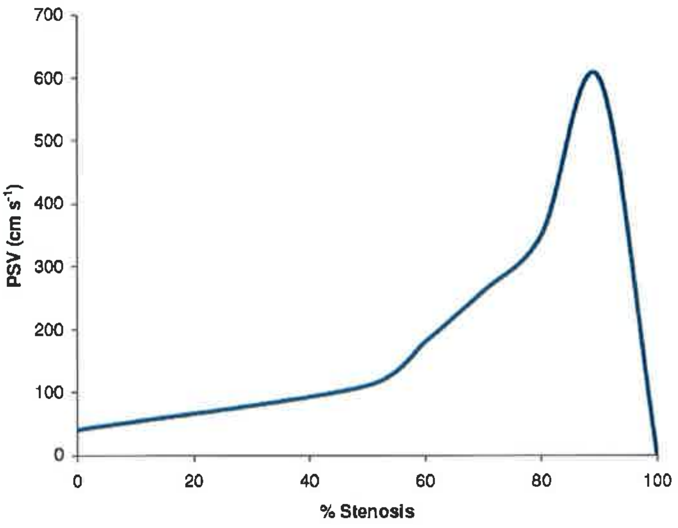

Figure 2.2 RAS quantification (followed from IPEM guidelines)

The most widely used parameters PSV and RAR and the other parameters such as RRR, RSR involves systolic velocity measured in the main renal artery. An accurate determination of systolic velocities is very important as an over or underestimation of the systolic velocity could lead to an error in the estimation of extent of stenosis ultimately leading to the mismanagement of patients for renovascularisation.

2.3.2 Flow phantoms

Flow phantoms mimic human vasculature physically and acoustically. They usually consist of a container filled with a tissue mimicking material (TMM) in which a vessel is embedded through which the blood mimicking fluid (BMF) is pumped. Figure 2.3 represents a schematic diagram of a simple flow phantom.

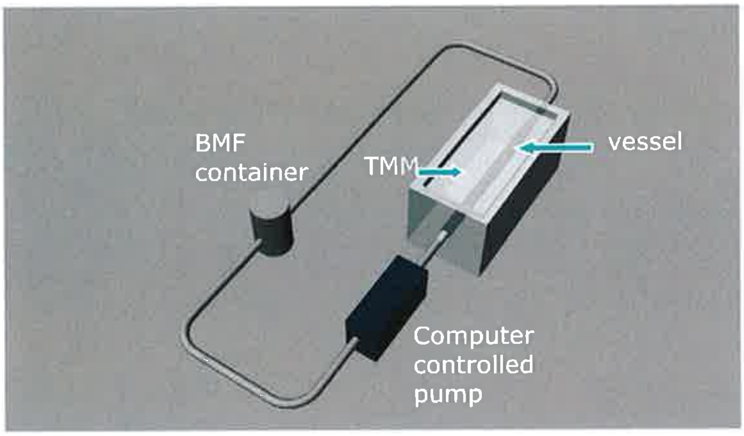

Figure. 2.3 Components of a basic flow phantom

The acoustic properties of the TMM, the vessel mimicking material (VMM) and the BMF in the flow phantom should mimic the acoustic properties of the human tissue, the vessel and the blood respectively. In the flow phantom, the vascular structure is chosen by selection of appropriate size and type of vessel mimicking material (VMM). The BMF is circulated in the vessel using a computer controlled pump. The computer controlled pump can simulate steady and physiological flow using a selected range of volume flow rate.

Flow phantoms are used to test the accuracy of ultrasound scanners in the maximum velocity estimation, a clinically important physical measurement. The values of the flow parameters in the flow phantom can be established accurately. The flow phantoms further can be designed to simulate complicated vascular structures such as vessel curvature, bifurcations and stenosis in the vessel. The well established flow parameters and the ability to represent complex vascular geometries facilitate the use of flow phantoms for the flow profile investigation studies in simple and complex vasculature. In addition, they can be used for repetitive flow experimentation so that the flow profiles can be investigated and studied in great depth. As a result, lengthy and expensive clinical trails can be avoided.

Components of flow phantoms

The three basic components of the flow phantom are the TMM, the BMF and vessel and the vessel made up of the VMM and each of these will be discussed in turn.

a) Tissue Mimicking Material (TMM)

The IEC has published recommendation [49] for the following physical properties of the TMM: density 1040 ± 100 kgm^{-3}; velocity 1540 ± 15 ms^{-1} and attenuation 0.5 ± 0.05 $\text{dBcm}^{-1}\text{MHz}^{-1}$ over 2-10 MHz frequency range with a linear dependence with frequency. A number of TMMs have been suggested so far in the literature [16] [50-53]. Lerski et al. suggested 'reticulated foam' as a TMM [54]. The attenuation of reticulated foam matched that of human tissue however it was observed that the reticulated foam did not represent an exact linear dependence with frequency [16]. The agar and gelatine based TMM have been observed suitable for mould formation and found to be reproducible and widely reported in the literature [51] [53][55-56]. Agar based TMM has also been well characterised [51] [57]. Some researchers have reported the difficulties with these TMM such as rupturing of the acute stenosis models due to insufficient mechanical strength to withstand the physiological pressure but have also commented that agar TMM were suitable to represent the lower stenosis geometry and also the models were observed stable during physiological flow experiments [56][50]. A konjac-carrageenan gel based TMM was used to develop carotid bifurcation phantom [50]. This TMM was reported to have a speed of sound of 1550 ± 6 ms^{-1} and an attenuation of 2.81± 0.08 dBcm^{-1} at 5 MHz [50]. Although this TMM was observed to be mechanically strong against the pressure developed in physiological flow, the authors reported problems related to insufficient adhesion between TMM and wall [50]. Polyurethane is a non-hydrogel based material used for

TMM formation and is used in commercial flow phantoms. It has a manufacture reported attenuation value of 0.50 ± 0.03 $dBcm^{-1}MHz^{-1}$ and speed of sound value of 1540 ± 15 ms^{-1}. The acoustic properties of this polyurethane based TMM used in ATS Labs' (Bridgeport, CT) phantoms has been independently assessed and reported to have a speed of sound of 1467 ± 1 ms^{-1} and an attenuation coefficient value of 0.43 ± 0.03 $dBcm^{-1}MHz^{-1}$ at 2.25 MHZ rising to 2.5 ± 0.03 $dBcm^{-1}MHz^{-1}$ at 15MHz [57]. The attenuation demonstrated a non-linear dependence with frequency [57]. A polymer based TMM Polyvinyl alcohol (PVA) TMM has been used recently in anthropomorphic brain phantom for Ultrasound and MR imaging [58]. This TMM was reported to have a speed of sound of 1520-1540 cms^{-1} and attenuation coefficients were in the range of 0.075- 0.28 $dBcm^{-1}MHz^{-1}$ for first to four freeze thaw cycles [58].

b) Blood Mimicking Fluid (BMF)

The next component in a flow phantom is the BMF. The IEC has published recommendation [49] for the following physical properties of the BMF: density 1050 ± 100kgm^{-3}; velocity 1570 ± 30 ms^{-1} and attenuation less than 0.1$dBcm^{-1}MHz^{-1}$, viscosity 4 ± 0.4 mPa s, scatterers' concentration >100 mm^{-3} and backscatter 1-10 x 10^{-31} $f^4m^{-1}sr^{-1}$ [49]. The BMF typically consists of particles suspended in the fluid. These particles behave like scatters and replicate the moving red blood cells (RBC) in the blood. The physical properties of the suspended particles (volume concentration, size) and the viscosity of the surrounding fluid decide the acoustic backscatter values of the particles. Several particles including cellulose pulver, starch, hardened RBCs, polystyrene microspheres, nylon and sephadex have been suggested so far [59] [26] [60]. The suspension fluid of BMF was mainly water however some researchers have also tried different combinations of oil based emulsions [61] [55]. The BMF developed in a European Commission project (phase 1) was found to have most acoustic and physical properties matching that of human blood [51]. This BMF consisted of 5 μm diameter nylon particles (Orgasol with a specified density of 1.03 $gmcm^{-3}$) as scatterers suspended in a water glycerol solution (10.25%) with dextran (3.42%), which was used to increase the kinematic velocity of BMF as per IEC standard and a surfactant (0.92%) for dispersing the scattering particles within the solution [51]. A commercial version of the above BMF recipe has been manufactured by Computerised Imaging Reference System (CIRS).

c) Vessel Mimicking Material (VMM)

The vessel is the next component used in the flow phantom. The IEC has stated the requirements of the physical properties of VMM similar to the TMM properties. However, in the healthy arterial wall has a speed of sound 1616 ± 30 ms^{-1} higher than actual soft tissue or the IEC specification of TMM [17]. Many different types of material including glass, heat shrink, Perspex, Teflon, latex have been proposed and used as vessel in the flow phantoms. The acoustic properties of these materials have been reviewed recently by Hoskins [16-17] and amongst the proposed materials for vessel the latex rubber tubing and C-flex have been widely used in the flow phantoms. The acoustic velocity of C-flex tubing and latex were observed to be 1556 ± 11 ms^{-1} and 1566± 12 ms^{-1} respectively, matching with the IEC recommendations for the speed of sound value of the vessel material. However the attenuation values for C-flex tubing and latex were 28± 4$dBcm^{-1}$ and 26± 3 $dBcm^{-1}$ respectively (measured at 5 MHz) were observed to be much higher compared with the standard value of 2.5 $dBcm^{-1}MHz^{-1}$ and presented a non-linear frequency dependence [16]. The high attenuation value of vessel material resulted in a distortion of the Doppler signal and this distortion was observed to be significant even for a 0.8 mm thick vessel [55]. The PVA-cryogel (derived after a series of freeze thaw cycle of aqueous PVA solution) has been used recently in the development of anthropomorphic ultrasound phantoms [18] [58]. The number and nature of freeze thaw cycles varies the acoustic properties of this material. PVA-c material is nontoxic, easily moulded into a desired geometry and it has been found to have similar acoustic and mechanical properties to that of healthy artery, both of which are considered to be an important characteristic of vessel mimicking material [18] [58]. However the main disadvantage using this material is considerable preparation time of minimum 2-3 days.

Flow phantoms designs

Many different designs of flow phantoms including a simple straight vessel and anatomical phantoms representing complex geometries such as curvature, bifurcation, symmetric and asymmetric stenosis, dual or multiple stenoses have been reported in the literature [17-18] [59] [62]. Flow phantoms having a vessel with vessel wall or even wall-less vessel flow phantom have been developed. The walled flow phantoms consisted of vessel made up of latex, C-flex tubing or PVA-cryogel. The stenosis could be introduced by attaching appropriate degree of plaque or calcification to the inner vessel wall or by producing a constriction in the vessel itself during the vessel development. A straight vessel flow phantom developed using C-flex tubing has been used to estimate the accuracy in the maximum velocity estimation [59]. Using PVA-c, a straight vessel flow phantom [62] and a range of anatomically realistic renal flow phantoms [18] have been developed very recently. The renal flow phantoms constructed using PVA-c have been used mainly for comparative studies in different imaging modalities.

Many of the commercially available vessel materials do not have acoustic properties matching to the actual vessel (except PVA-c which has recently been proposed). The wall-less flow phantoms had overcome this problem as they do not have any tubing material present in the phantom, causing distortions of the Doppler signal and can produce various geometrical shapes. Several designs in wall-less flow phantoms representing simple straight wall-less vessels to complex anatomical vessels have been developed to date [56] [55] [61] [63]. A straight wall-less flow phantom has been constructed using a straight metal rod [56]. The metal rod was placed in the container and TMM was poured and allowed to set. The removal of rod from the casted TMM produced a wall-less channel. The positioning of the rod and proper selection of its dimension provided a channel of appropriate diameter at desired depth in the TMM. A stenosed straight wall-less flow phantom was produced similarly except using a pair of detachable metal rods milled to have a definite degree of stenosis. The rods were pulled in opposite directions to keep the stenosis geometry intact [56] [64]. The important requirement for the wall-less flow phantoms is a very good seal where the inlet and outlet tubes are connected to TMM channel. The studies have reported a few attempts of using cylindrical end pieces fixed to the walls [55] or 'reticulated foam' seals [56] to prevent the leakage at the inlet and outlet. The 'reticulated foam' was observed to provide a good seal and reduced the problems associated with TMM leakage even for acute (75%) stenosis geometries under physiologic flow conditions.

The wall-less flow phantoms with more complex geometries such as dual stenosis and anatomically realistic vessels were constructed using a lost core technique [61] [63][65-66]. The lost core technique involves use of a low melting point alloy. The complex vessel models of low melting point alloy are constructed using an appropriate mould and the TMM is cast around it. The TMM once casted is heated at a temperature corresponding to the melting point of alloy at controlled condition and the molten metal mass was taken out. The removal of melted alloy results in a wall-less lumen with the required vessel geometry. To date, the complex structures including a vascular phantom with dual stenosis [65], carotid artery bifurcation [61] and carotid artery with stenosis [63] [67] have been developed using this lost core technique. Recently, a wall-less renal artery flow phantom representing a range of symmetrical stenosis conditions has been developed by King [18]. This phantom was used to assess the performance of CT, MR and US modalities in the diagnosis of RAS.

The wall-less flow phantoms have proven very useful in the study of stenosed vessels and for flow profile studies of various simple and complex geometries [56]. The problems associated with the rupture of the agar based wall-less flow phantoms under high physiological flow conditions, insufficient sealing in the case of konjac-carrageenan TMM flow phantoms are still the main limitations of this type of wall-less flow phantoms.

Few researchers have attempted the use of actual human vessels embedded in the tissue mimic in the flow phantom [68]. These vessels were excised during post mortem and preserved in formaldehyde. An example of one such real vessel flow phantom consisted of human iliac artery embedded in agar based tissue mimicking material filled in an acrylic container. The vessel ends were connected to an external flow system using small acrylic tubes at both ends which provided good mechanical support. The phantom was used to compare performance of x-ray angiography, CT and B-mode US modalities to visualise the diseased condition such as deposition of plaque and calcification [68]. An attempt at developing an anatomically realistic carotid artery phantom using clinical post mortem arteries has also been reported [69]. This phantom was used to investigate the flow profiles in carotid artery with severe atherosclerosis. The acoustic and geometric properties of such excised vessels vary if they are not preserved properly [70]. The preservation and acoustic and mechanical characterisation of the real vessels is difficult to achieve without damage being caused to the vessels. Also, obtaining multiple copies of the exact specified geometries is practically very difficult. Furthermore, the strict legislation about use of human tissues and the biological safety issues have limited the use of real vessels in a flow phantom.

Few of these anatomical flow phantoms have been used to investigate the complex velocity profiles in arteries by flow experimentation with a majority of them concentrated on carotid arteries [71] [69]. The physiologic flow profiles by flow experimentation in agar based carotid artery phantom bifurcation models with normal, 30%, 50%, 60% and 70% stenosis have been investigated by Poepping *et al.* [63] and more recently in a Teflon-base carotid bifurcation model with moderate eccentric stenosis by Wong Y W *et al.* [72] .These models have succeeded in providing the flow characteristics widely reported in the clinical literature as being present in the carotid bifurcation under various diseased conditions. To date no studies investigating the 3D physiological velocity profiles in anatomically realistic renal artery phantoms have been reported.

2.4 Subcutaneous fat layer and its effect on maximum velocity estimation

Subcutaneous fat refers to the fatty or adipose tissue layer lying directly under the skin layers. The presence of an abdominal fat layer is a major limiting factor in renal imaging as it cause excessive attenuation of the ultrasound beam and can produce signal distortion due to excessive attenuation and increased signal distortion thereby causing difficulties in imaging the flow in small vessels and in small areas such as stenosis. Subcutaneous fat affects the maximum velocity estimation an important criteria for RAS investigation [18]. An error in the maximum velocity estimation leads to an error in the estimation of stenosis. Recently, several studies were performed to investigate the effect of a subcutaneous fat layer on the maximum velocity estimation [24]. The studies however were limited to estimation of the maximum velocity. In the diagnosis of renal artery stenosis, the systolic as well as diastolic velocities, physiologic flow velocity profiles and the Doppler flow waveform are also considered important. Therefore, knowledge of how the subcutaneous fat layer affects the physiologic flow profiles and the flow waveforms is very important.

Many researchers have studied the accuracy of Doppler velocity measurements, in particular maximum velocity estimation and have discussed the possible factors affecting the accuracy in the measurement [20-23]. Some of the factors effecting maximum velocity estimation include: error in Doppler angle measurement, frequency dependent attenuation of ultrasound by the tissue, assumption of a single value of speed of sound (1540 ms^{-1}) in the image reconstruction algorithms, geometrical spectral broadening and refraction effects due to different tissue layers leading to errors in the Doppler angle measurement. These sources combine to form a maximum velocity error. A complete description of these factors contributing to these errors are summarised by Christopher *et al.* [20]. Hoskin have reported additional error factors such as intra-transducer variations and inter-machine variations in the maximum velocity estimation [21].

Doppler test object most frequently used to assess the accuracy in the velocity estimation is 'string phantom'. It consists of a string (loop of filament) mounted around wheels, one of which is a motorised wheel. The motor is computer controlled which drives the wheel and thus the string at the desired velocity. The string phantom is used in a tank filled with velocity-corrected degassed water at room temperature [73]. The velocity-corrected water was achieved using a water-alcohol solution (9.5% alcohol + 90.5 % water) with the speed of sound of 1540ms^{-1} at 20^{0}C similar to the speed of ultrasound in the soft tissue. Using a string phantom, the accuracy in the velocity estimation was estimated by comparing the measured velocity with the set string velocity [16]. Trough the use of a steady motion string phantom, Hoskins reported an error ranging from -4% upto 47% in the maximum velocity estimation, as a combined effect of sources of errors such as intra-transducer variation, Doppler angle mis-measurement and inter-machine variations. The string phantom however, does not mimic the actual *in-vivo* situation for the following reasons. The water-alcohol solution (9.5% alcohol + 90.5 % water) used in the string phantom is a single continuous medium. The speed of sound of water-alcohol solution is 1540ms^{-1} at 20^{0}C, which is similar to the speed of ultrasound in the soft tissue; however, it is a non-attenuating medium [73]. The ultrasound beam travelling in the body passes through layers of different tissues. The tissues attenuate the beam, with the attenuation being approximately proportional to the frequency of the ultrasound wave [74]. As a result, the higher frequencies get preferentially attenuated reducing the effective bandwidth [26]. However, ultrasound imaging systems do not take into account the reduced bandwidth and rather use the original transmitted frequency in the calculation of the Doppler shift frequency resulting in an error (underestimation) in the maximum velocity estimation. Flow phantoms mimic the *in-vivo* situation more closely and a few studies have been performed to estimate the accuracy in the maximum velocity estimation using such flow phantoms [59] [18]. Winkler *et al.* have reported an error in the maximum velcoity estimation as high as 40% because of intra- and inter-machine errors [88].

When the ultrasound beam travels through the body, it passes through several tissue layers such as skin, subcutaneous fat, tissue and blood. Figure 2.3 shows a typical path of ultrasound beam travelling in the abdominal area of the body.

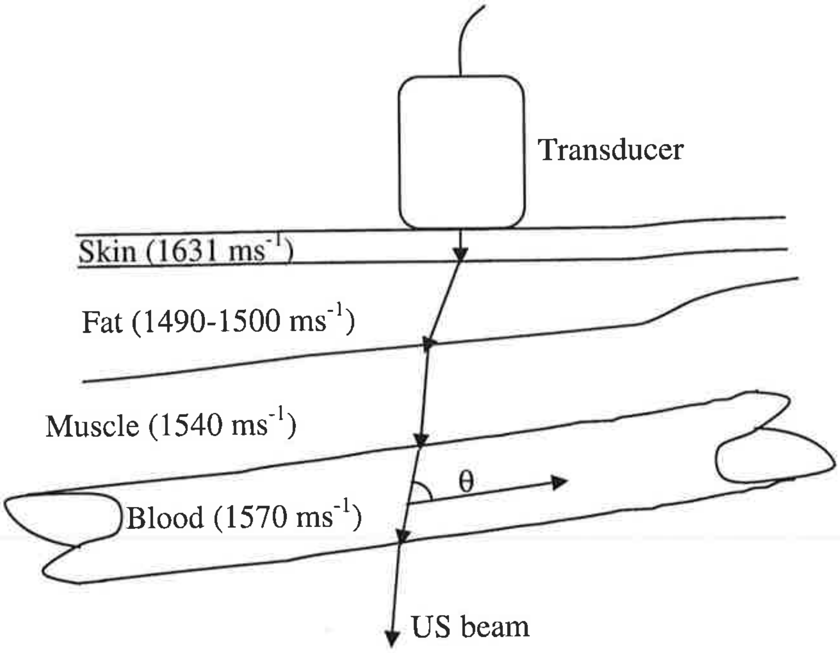

Fig. 2.3 Path of a ultrasound wave in the body

The speed of the ultrasound wave in each layer is different, with the speed of sound for subcutaneous fat reported to be in the range of 1430ms^{-1} to 1500ms^{-1} [75]. The ultrasound scanner generally assumes a single speed of sound of 1540ms^{-1} which is used to calculate the depth information for the reconstruction of the B-mode images distances from the time of flights [20]. Consequently, difference in the assumed fixed speed of sound (1540 ms^{-1}) in all tissues and the actual speed of sound in subcutaneous fat as well as other tissues results in incorrect distance measurement leading to inaccurate distances displayed on the B-mode images.

Furthermore, the ultrasound wave incident on the boundary between two different tissue layers with an angle of incidence, θ_i, (>0), undergoes refraction. The multiple layers of the tissue with different speed of sound result in multiple beam refractions.

The tissue layers with different speed of sound, causing multiple refractions of the incident and the reflected waves, result in distortion of the distances and angles in the displayed B-mode images. These distortions can lead to an error in the measurement of Doppler angle (which in practice is measured by the operator from the B mode image). The error in the Doppler angle measurement affects the maximum velocity estimation [20]. The combined effect of different speeds of sound in tissue and the blood and refraction on the maximum velocity estimation has been studied by Chirstopher *et al.* using a modified string phantom with two layers of materials with different speed of sound and an error of 8% in the maximum velcoity estimation has been suggested [20]. The effect of a subcutaneous fat on maximum velocity estimation was recently studied using a string phantom and a simple walled flow phantom by King *et al.* [24] and a signifcant overestimation ($p<0.05$) of maximum velocities was reported. In this study, an olive oil layer of fixed thickness was used to mimic the subcutaneous fat. The speed of sound and attenuation value of olive oil has been reported to be 1430 - 1500 ms^{-1} and 0.2 $dBcm^{-1}MHz^{-1}$ respectively [26]. Browne *et al.* reported the olive oil speed of sound and attenuation values as 1490ms^{-1} and 0.29 $dBcm^{-1}$ MHz^{-1} (measured at 3 MHz) respectively [25].

From a clinical perspective, it is very important to have a good understanding of the effect of subcutaneous fat of different thickness on the magnitude of the error in maximum velocity estimation. However, the effect of a subcutaneous fat of varying thicknesses on the physiologic velocity profiles in the renal arteries and on the physiological PW Spectral Doppler waveform has not been studied to date.

2.5 Aims and Objectives of the present study

The work in this thesis is focussed on the study of physiological velocity profiles in the renal artery investigated by detailed physiological flow experimentation using anatomically realistic renal artery flow phantoms. The renal flow phantoms used in the present study were previously successfully used to evaluate the performance of different imaging modalities for disease investigation in the renal artery [18]. Furthermore, some basic experimentation investigating the effect of fat mimicking layer on maximum velocity estimation have been performed using a steady flow of velocity 40 cms^{-1} in these phantoms [18]. In renal arteries, a physiological flow is more realistic. Therefore, it was considered necessary to investigate the velocity profiles in normal as well as simulated diseased renal arteries using physiological flow waveforms which it was hoped would provide a greater understanding of renal flow in normal and diseased conditions. In the future, the study of the physiological velocity profiles characteristics may be helpful to predict the hemodynamic flow in individual patients and thus could provide useful information for the management of patients who need to undergo renovascularisation. The measurement of velocity profiles could lead to a new diagnostic tool for renal artery disease investigations. The study of the fat layer effect on the measured physiologic velocity profiles and on the profile of the physiological Spectral Doppler velocity waveforms could also definitely contribute important information which may be useful while defining the physiologic velocity profiles and physiologic velocity waveforms as clinically important criteria for RAS investigation.

Specific Objectives:

- Investigate the 3D velocity profiles in anatomically realistic renal flow phantoms representing a range of symmetric and asymmetric stenosis, by physiological flow experimentation, focussing on the following specific conditions:
    - Normal, 30% symmetrical stenosis, 50% symmetrical stenosis and 70% symmetrical stenosis
    - 25% asymmetrical stenosis, 35% asymmetrical stenosis and 45% asymmetrical stenosis

- Investigate the effect of fat mimicking layer (of 20 and 30mm thickness) on the measured physiological velocity profiles in the renal artery flow phantoms.
- Investigate the effect of the fat mimicking layers on the shape and profile of the physiological velocity waveform

Chapter 3 Methodology

3.1 Introduction

This chapter describes the methodology followed to achieve the objectives of the thesis and to that end the following flow experiments were performed to investigate the velocity profiles in two types of flow phantoms: a) basic straight wall-less flow phantoms and b) anatomically realistic renal flow phantoms. Two basic straight wall-less flow phantoms, with no stenosis and 30% stenosis, respectively were constructed using the methodology described in section 3.2. Seven anatomically realistic wall-less renal artery flow phantoms of a normal renal artery and with 30%, 50% and 70% symmetrical stenosis and 25%, 35% and 45% asymmetrical stenosis, respectively. The construction of the anatomically realistic phantoms is described in section 3.3. Section 3.3 also includes the methodology for a) the acoustic characterisation of TMM b) the geometric accuracy assessment of the phantom development; and c) the assessment of the stenosis models stability. Section 3.4 describes the details of the flow experimentation and the protocol followed to investigate the velocity profiles in these phantoms. Furthermore, experiments to investigate the effect of varying thicknesses of fat layer on the physiological flow profiles and on flow waveform are described in sections 3.5 and 3.6, respectively.

3.2 Construction of the straight wall-less flow phantoms

The straight wall-less flow phantoms were developed using the IEC recommended agar based TMM described by Teirlinck *et al.* [51] and the IEC recommended BMF described by Ramnarine et al. [56].

Normal straight wall-less flow phantom construction

A plastic container of dimensions 230 mm x 135 mm x 103 mm (L x W x H) with a wall thickness of 2.6 mm was used for the flow phantom housing and a pair of plastic connectors (inner diameter 7.2 mm) were attached at the centre of the end walls of the container. The connectors served as an inlet and outlet port for the phantom. A piece of reticulated foam of dimensions 60mm x 60 mm x 10mm (L x W x H) was glued on the inner wall, surrounding the plastic connectors. The TMM could pass through the pores of reticulated foam. The reticulated foam was used to develop an effective seal surrounding the plastic connectors, preventing the leakage of the BMF. A rubber mat was placed at the bottom of the container to avoid strong reflection from the bottom of the plastic container while imaging the vessel lumen. A straight metallic rod (diameter 6.8 mm), slightly greased, was placed in the plastic container through the plastic connectors and was held tightly at the centre. The assembly is shown in figure 3.1(a). The IEC TMM was poured into the container and allowed to set as shown in figure 3.1(b). Once the TMM was set, the rod was pulled out care being taken not to disturb the surrounding TMM. The removal of rod from the set TMM resulted in a straight wall-less vessel embedded in the TMM. Figure 3.1 shows the steps involved in the development of straight wall-less flow phantom.

(a) (b) (c)

Figure 3.1 Illustrated the steps in the development of the straight wall-less flow phantom (a) metal rod placed centrally in the container (b) TMM surrounding the metal rod (c) constructed normal straight wall-less flow phantom

The phantom was preserved by maintaining a layer of water-glycerol solution (10% glycerol, 90% degassed water and 0.1% Benzalkoliumcholride (BC)) on the top and tightly fixing the lid of the phantom container while the phantom was not in use. The vessel lumen was also filled with the water-glycerol solution to prevent it from drying out. The water glycerol solution prevented the phantom from drying out and the antibacterial agent prevented bacterial growth in the phantom. The fully-constructed straight wall-less flow phantom with tubing attached at the inlet and outlet connectors is shown in figure 3.1(c).

30% stenosis straight wall-less flow phantom construction

The 30% stenosis straight wall-less flow phantoms was constructed using a similar process explained in the previous section above except a pair of rods was used instead of a single metal rod. Each rod was milled at one end to achieve a constriction of 30% over an axial length of 5 mm. The milled ends when coupled formed a symmetrical constriction of 30% (in diameter) over an axial length of 10 mm, at the centre, as shown in figure 3.2(b).

(a) (b)

Figure 3.2 Paired metal rods (a) separate milled rods, each having 5 mm constriction (b) Coupled rods representing a 10 mm axial constriction at centre

In this case, when the TMM had set, the two rods, were pulled in opposite directions by slow rotation in opposite directions, without disturbing the set TMM, resulting in a straight wall-less vessel with a constriction of 30% developed at the central portion of the vessel. The steps involved in the development of the 30% stenosis straight wall-less flow phantom are shown in figure 3.3.

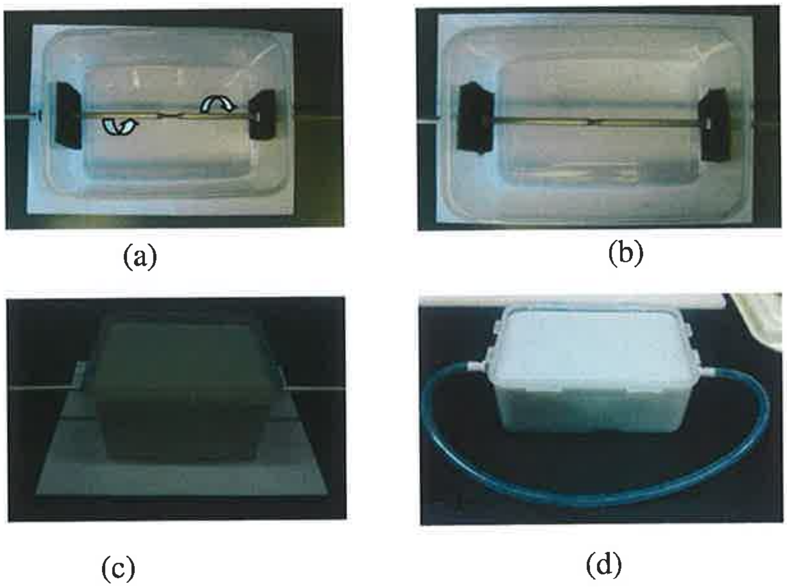

(a) (b)

(c) (d)

Figure 3.3 Steps in the development of straight wall-less flow phantom (a) metal rods coupled using a coupling screw (b) coupled rod positioned in the container (c) TMM surrounding the coupled metal rod (d) fully-constructed 30% stenosis straight wall-less flow phantom

3.3 Development of the anatomically realistic renal flow phantoms

The anatomically realistic wall-less renal artery flow phantoms were developed using IEC TMM [51], BMF [51] and metal models of a human renal artery. These metal models were constructed using a so-called "soft tool" of the renal artery, which was developed as a part of the Ph.D. thesis work by Dr.King [18]. The steps involved in the development of this soft tool of the renal artery are explained briefly in section 3.3.1. The construction of the metal models is explained in section 3.3.2 followed by a more detailed procedure of the renal artery flow phantoms' construction in section 3.3.3.

3.3.1 Renal artery soft tool –developmental steps

An abdominal scan using a 64-slice X-ray CT scanner was acquired covering the region of the renal arteries of a healthy volunteer with normal vasculature and imported in a commercial software package (MIMIC 6.3, Materialise, Leuven, Belgium). Using the software's digital masking technique and picture editing tools, the left renal artery portion in the (selected) image was highlighted. The digital mask applied set threshold to the selected grey-scale image such that only the pixels corresponding to the correct density were highlighted (renal artery). The segmented portion was rendered as a basic three dimensional (3D) model of normal renal artery. Based on the dimensional information of the renal artery (obtained from the basic 3D model), a 3D computer model of the normal renal artery (figure 3.4(b)) was developed in Solid Works software (Dassault Systèmes Solid Works Corp., MA, USA). Instead of developing a computer model of each diseased renal artery, a master computer model, which could represent normal renal vessel as well as accommodate various stenosis geometries was developed as shown in figure 3.4(c). This master model included a circular disc of 20 mm diameter at the desired location of the stenosis. The position of the circular disc in the master model was chosen at the proximal end just before the curvature as shown in figure 3.4 (c). The position was chosen such because it has been widely reported in the literature that upto 66% of atherosclerotic renal artery stenosis typically are located in the ostium and at the proximal 20 mm of the renal artery [18][85][86] and the fact was also iterated by several vascular technicians. A physical or prototype model of the renal artery (figure 3.4(d)) was developed by rapid prototyping of 3D master model of the renal artery described above. The rapid prototyping machine was a Zprint 3D printer. The printer software controlled the building of models in layers or slices of 0.1 mm thickness typically. The layers/slices were glued together simultaneously as the model was being built. The rapid prototype physical model of the renal artery was then used to develop the soft tool of the renal artery by vacuum casting the silicon rubber around the rapid prototype model. Once it had set, the silicon mould was cut into two symmetric portions along a horizontal plane passing through the centre of prototype model. A zigzag pattern cut symmetrical to the horizontal plane was made. This zigzag cut facilitated a firm sliding of the two portions of the soft tools over each other. The physical model of the renal artery was finally removed from the soft tool and the soft tool was cleaned. The developed soft tool is shown in figure 3.4 (f). The circular disc in the rapid prototype model provided a slot for positioning the stenosis insert pair in the soft tool. The insert pair was modelled such that its surfaces were tangential to the surface of the renal artery at the edges of the stenosis. The physical model of the inserts was prepared by rapid prototyping the 3D computer model of the inserts. The procedure was repeated to generate a series of geometrically similar inserts that differed only in the reduction in diameter.

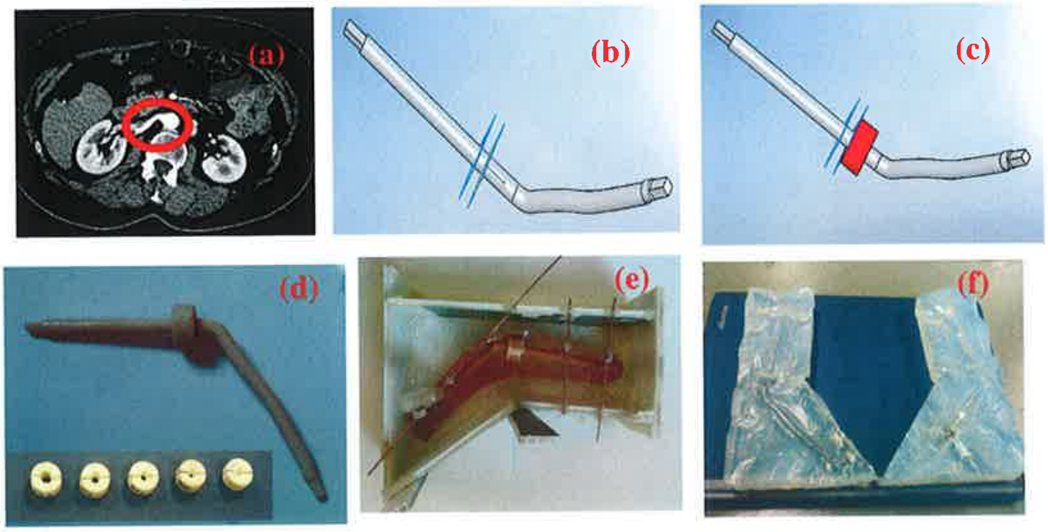

Figure 3.4 Steps in the development of renal artery soft tool (a) transverse abdominal X-ray CT image with left renal artery and aorta portion highlighted (b) 3D computer model of normal renal artery extracted from the CT image data (c) 3D computer model of renal artery with circular disk (highlighted) at the region of stenosis (d) rapid prototype model of a renal artery and the inserts using polyfil and a water based resin (e) fabrication of soft tool (f) renal artery soft tool made from silicon rubber

3.3.2 Construction of metal models of renal artery

Metal models of the renal artery were then constructed using a low melting point alloy (MCP 47 Mining and Chemical Products Ltd., Wellingborough, Northants, UK). This alloy has a melting point of 47^0C. To develop the metal model firstly, the appropriate insert pair was placed in the soft tool of renal artery. The inserts were placed tangential in the slot and remained perpendicular to the renal artery lumen as shown in figure 3.5(a). The soft tool was clamped together, which allowed the two parts of soft tool to slide tightly over each other as shown in figure 3.5(b). The low melting alloy was heated in a glass beaker up to 55-60^0C. The molten alloy was poured into the soft tool through the filling port and left to solidify. The example of a solidified model is shown in figure 3.5(c). The solidified metal model was then removed from the soft tool. Following this, the inserts were removed carefully and the metal model was hand polished using a soft brush attached to a drill rotating with very low speed to produce a smooth surface finish. In case of acute stenosis (for example 70%), the metal models were observed to be very fragile and prone to breakage at the acute constriction point while polishing. Therefore, for the acute stenosis models, the inserts were left intact first and the areas other than stenosis were polished. The inserts were then removed carefully and the metal model areas under the inserts and nearby were polished carefully. The low melting point alloy contains heavy metal therefore appropriate care was taken while handling and polishing the metal models to avoid any type of contamination. The steps that were followed in the development of metal models are shown in figure 3.5. The developed metal models with symmetric stenosis of 30%, 50% and 70% and asymmetric stenosis of 25%, 35% and 45% are shown in figure 3.6(a) and 3.6(b) respectively. These metal models were used in the construction of wall-less renal artery flow phantoms.

(a) (b) (c)

Figure 3.5 Development of renal artery metal model (a) soft tool with inserts positioned (b) clamped soft tool (c) solidified metal models with inserts attached (before polishing)

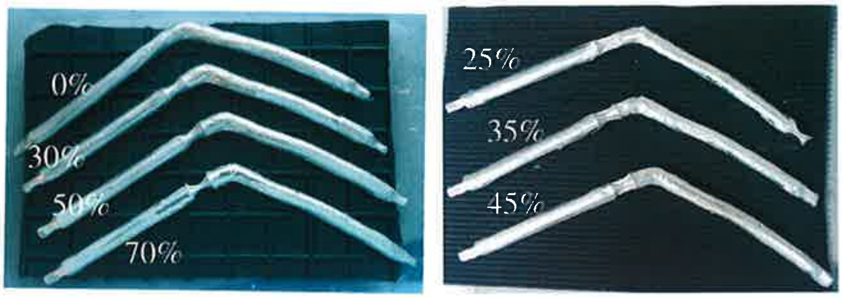

(a) (b)

Figure 3.6 Renal artery metal models (a) with symmetrical stenosis (b) with asymmetrical stenosis

3.3.3 Construction of the wall-less renal flow phantoms

The wall-less renal artery flow phantoms were constructed using the "lost core" technique [56]. In each case, the phantoms were housed in a plastic container of dimensions 230 mm x 135 mm x 103 mm (L x W x H) and a wall thickness of 2.6 mm. A pair of barbed connectors (7 mm inner diameter) were attached to the end walls of the container and reticulated foam of dimension (60mm x 60mm x 10mm (L x W x H)) was glued to the container end walls surrounding the connector on the inner wall of the container. The reticulated sponge, surrounding the connectors helped to prevent leakage at the inlet and outlet port. A thin strip of reticulated foam was glued across the entire inner wall of the container near the top surface. This additional thin strip of sponge helped to maintain good contact between and the walls of the container. A rubber mat was placed on the bottom of the phantom container to avoid strong reflection from the bottom of the container while imaging the vessel. The metal model was wrapped using a thin layer of cling-film which served to avoid a direct contact between the metal model and the TMM. Two sections of cling film were used, each part wrapping a section of the metal model of each side of the constrictions. The separate cling films facilitated the easy removal from the two sides without disturbing the vessel geometry developed at the centre of the container. The cling film was wrapped around the metal model keeping some extra wrap length at both ends to facilitate its removal later. The wrapped metal model was secured at the centre of the container as shown in figure 3.7(a). The TMM was then poured into the container and allowed to set (figure 3.7(b)). Once the TMM was set, the phantom container was placed in a temperature controlled water bath (maintained at 55°C) for approximately six hours. The controlled heating of the phantom resulted in the melting of the metal model which was contained in the cling film. The cling film wrap containing the molten alloy was then removed by carefully pulling the cling film out of the phantom container. Any remaining metal particles left in the lumen were removed by circulating hot water at very low velocity through the phantom. The fully-developed flow phantom is shown in figure 3.7(c).

(a) (b) (c)

Figure 3.7 Steps in the development of renal artery flow phantom (a) renal artery metal model with cling film wrap, positioned in the container (b) TMM surrounding the metal model (c) developed renal artery flow phantom

Seven renal artery flow phantoms representing a range of stenosis were constructed following the above procedure using a separate, appropriate metal model and the insert in each case. The constructed renal artery flow phantoms were imaged using B- mode ultrasound with a linear array transducer (5-13MHz) of a Siemens Antares Ultrasound system. The lumen was observed in the B mode images to determine if the lumen was free from metal residue. If necessary, the lumen was cleaned carefully using pipe cleaners with care being taken not to disturb the set TMM. The developed phantoms were stored at room temperature with a layer of water-glycerol solution (10% glycerol, 90% degassed water and 0.1% BC) on the top of the TMM and the lid fixed tightly in place while the phantom was not in use. The vessel lumen was also filled with a water-glycerol solution to prevent from drying.

3.3.4 Assessment of geometric accuracy in the renal artery flow phantom development

The accuracy in the development of the renal artery flow phantoms was tested by comparison of the renal artery diameters, measured at two stages during the construction process: (a) at the metal model and (b) renal artery lumen (developed in the renal flow phantom) stages and determining if there was any statistical difference in the diameters.

In stage (a), the diameter of the metal model was determined at three different locations (shown in figure 3.8) using a vernier callipers (accuracy ± 0.01mm). The three locations shown in the figure 3.8 are (i) at the stenosis (ii) 25 mm away from stenosis (towards the inlet), and (iii) 50 mm away from stenosis (towards the outlet) with the length measured along the central axis of renal model. Three copies of each metal model (representing same degree of stenosis) were developed and the diameters at the diameters in each location were determined.

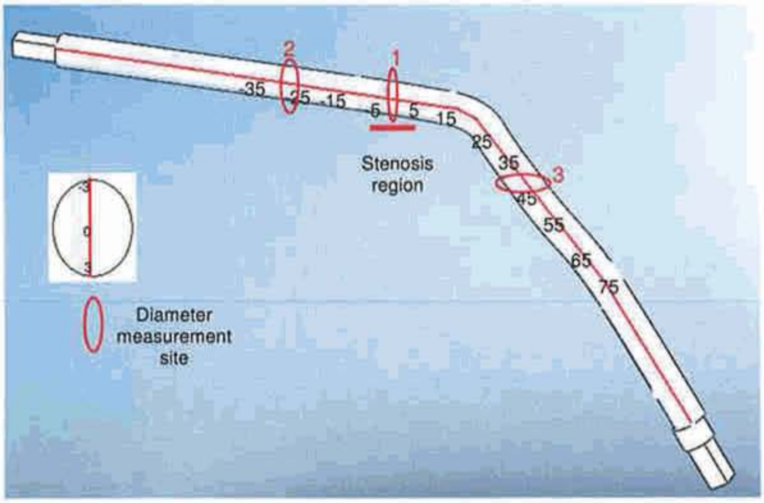

Fig 3.8 Diameter measurement sites in the renal artery metal model

In stage (b), the renal artery lumen diameter was measured using the optimised B- Mode Ultrasound image of each renal artery flow phantom developed. The B- Mode images were obtained with a linear array transducer (5-13MHz) of a Siemens Sonoline Antares Ultrasound system. The renal lumen diameter was measured using the system's electronic callipers (accuracy ± 0.1 mm).

The diameters measured at stage (a) and (b), at each measurement site, were compared using a paired t-test and the corresponding p value was determined at each measurement site for all the phantoms. In the paired t-test, the null hypothesis being tested was that there was no difference in the diameters of renal artery model determined at the two different stages. If $p < 0.05$, then the null hypothesis was rejected indicating a statistical difference in the diameter was measured at the two different stages ((a) and (b)). The statistical tests were performed using Sigma-plot software (Systat Software, Germany).

3.3.5 Assessment of geometric stability of stenosis models

The geometric stability of the stenosis models was assessed on the basis of visual observations used to identify signs of TMM fracture and BMF leakage during the flow simulation test. The renal artery flow phantom was connected to the computer controlled pump system and a pulsatile flow of velocity 2-40 cms^{-1} was established. The flow was maintained for three to four hours. The visual appearance of the TMM to identify if TMM remained intact and fracture of BMF leakages had occurred were noted at regular interval of 30 minutes. All the flow phantoms apart from the 70% stenosis renal artery flow phantom remained intact and withstood the pressure generated due to physiologic flow and did not show any signs of 1) fracture of TMM and 2) signs of BMF leakage. These renal artery flow phantoms were used for the physiological flow experimentation. The stability of the stenosis geometry was assessed by comparing the renal lumen diameters at the stenosis (determined from B- mode images using system's electronic callipers) initially and after 4 hours of continuous flow.

3.3.6 Acoustic characterisation of TMM samples

The speed of sound (c_s) and attenuation coefficient (α) of all the TMM samples were determined using an in-house developed Scanning Acoustic Macroscope (SAM) system applied to test samples from each batch of TMM that was produced. The SAM system consisted of a Panametrics pulse receiver (Model 5052PR), a linear actuator, a data acquisition card (NI PCI-5144), a broadband transducer of central frequency 7.5 MHz and a temperature monitored (degassed) water tank. The linear actuator controlled the transducer movement in a predefined area, with overall control performed via a Lab-View (version 7.1, NI, USA) program. The transducer was operated in pulse-echo mode. The technical properties of the broadband transducer are given in Table 3.1. A schematic diagram of the Scanning Acoustic Macroscope is shown in figure 3.9

Table 3.1 properties of the transducer

Transducer	7.5 MHz
Frequency Range	5.15 MHz – 9.44MHz
Focal Point	9.54cm
Crystal Diameter	12.7mm

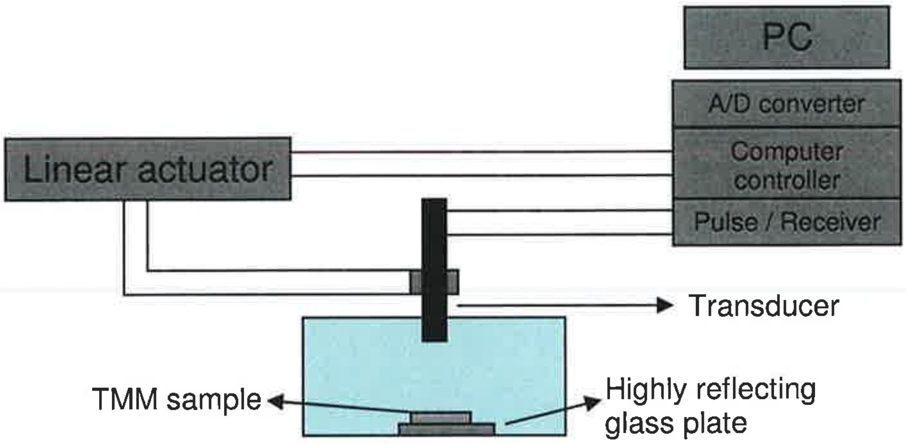

Fig 3.9 Schematic diagram of Scanning Acoustic Macroscope

Sample preparation:

The test samples of TMM were obtained during the production of the TMM for the phantoms, cast in a hollow cylindrical perspex sample holder of 12 mm long and 50 mm in diameter. A saran wrap was attached across the open faces using glue to hold the TMM intact while casting. An inlet of 4 mm diameter was drilled along the Perspex wall to facilitate injecting of the TMM into the sample holder which was held fixed in between two aluminium plates, which were held tightly using a clamp. The TMM was poured in the sample holder and allowed to set. All such TMM test samples were preserved in water glycerol solution (10% glycerol, 90% degassed water and 0.1% BC) to prevent them from drying out.

Data acquisition

The transducer was positioned in a water tank and focussed on the surface of the glass plate reflector. Using the programmed linear actuator, the transducer was moved, in an interval of 1 mm, in the predefined area and the ultrasound pulse was transmitted at each position and a delay was applied to facilitate the collection of the echo data. The reflected pulse returning to the transducer was digitised and the data was stored for off-line analysis. A reference data set was initially acquired first from a scan of the glass plate reflector. The TMM sample was then placed on the glass plate obstructing the space between the transducer and the glass plate. A sample data set was then acquired from with the TMM sample positioned over the glass plate. An in-house MATLAB program was used to analyse and plot the sample and reference data sets. A window size was chosen such that it accommodated both the sample and reference pulse as illustrated in figure 3.10. A further analysis of the sample and reference pulse was carried out using the MATLAB program, to determine the speed of sound and attenuation coefficients.

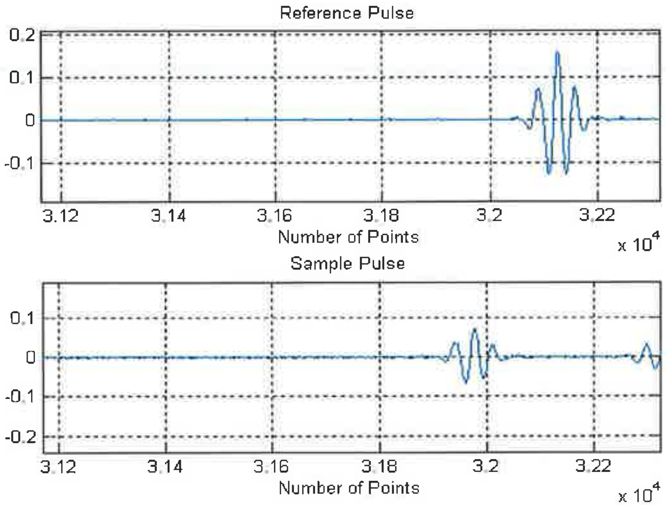

Figure 3.10 Plot of a typical reference and sample RF pulses

Speed of Sound

The speed of sound (c_s) of the TMM sample was calculated using Equation 3.1 [76].

$$c_s = \frac{c_w}{1 + \Delta t \frac{c_w}{2d}} \qquad \text{Equation 3.1}$$

where d is the thickness of the sample, c_w is the speed of sound in water and Δt is time shift (calculated as the difference of the peaks of the RF pulses from the glass plate reflector with and without the TMM sample in place).

Attenuation coefficient

The attenuation (α) of the TMM sample, measured at central frequency (f) of 7.5 MHz was calculated using Equation 3.2 [76].

$$\alpha(f) = -\frac{10}{2d}\log_{10}\frac{I(f)}{I_0(f)} \qquad \text{Equation 3.2}$$

where d is the sample thickness, $I(f)$ is the power spectrum intensity at frequency f and $I_0(f)$ is the power spectrum intensity (at frequency f), of the reference signal with no sample in the path.

3.4 Flow experimentation for both the straight and the anatomically realistic renal flow phantoms

3.4.1 Experimental set-up

The experimental set-up (shown in figure 3.11) consisted of the appropriate flow phantom connected in-line to the flow system, through which the BMF was circulated. The BMF was circulated through the flow system using a computer controlled pump.

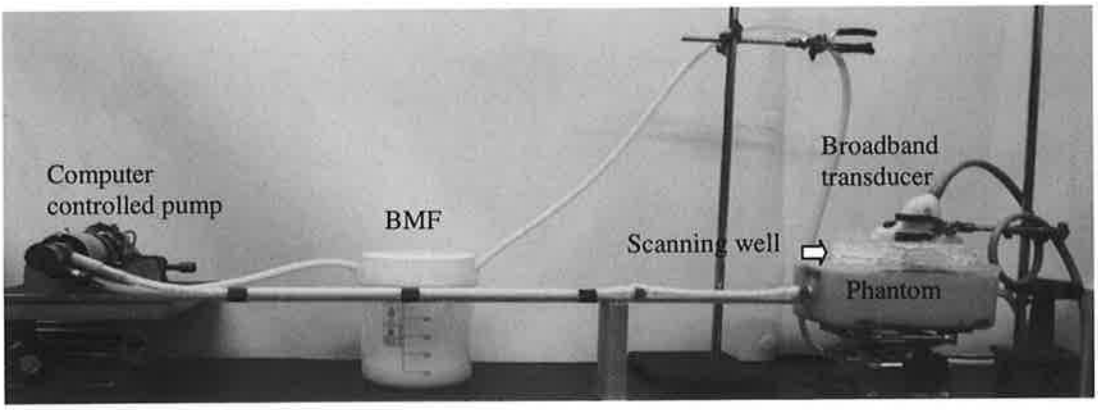

Figure 3.11 Experimental set-up for the flow experiments

Pump motor system

The pump that was used for the flow experiments described herein was a cavity style pump consisting of a rotor which when turned using a servo motor, transferred the BMF through small, fixed shape cavities. The cavity style pump offered low shear stress and therefore was considered to be ideal for circulation of the BMF. An amplifier (Aerotech Ltd., Berkshire, UK) controlled by a computer controller program was connected to the pump motor. The computer controller program could produce steady or arbitrarily shaped, or pulsatile flow rate waveforms with variable peaks or mean flow rates which were amplified in the amplifier and the resultant amplified signal was sent to the pump.

Computer controller program development

The computer controller program was developed in the Lab-VIEW software environment. In the program, a physiological flow waveform was generated using a Lab-VIEW measurement data file obtained by the following steps. Firstly, a spectral Doppler image of a renal flow waveform in a healthy volunteer was observed and the image was captured for offline analysis. The velocity information was then derived by a sampling method. This involved selection of pixels on the spectral Doppler waveform image and determining the velocities represented by these pixels manually using the velocity scale displayed on the image. Using these sampled velocities and the knowledge of pump flow rate, a data file consisting of a set of magnitudes of the controlled voltages was generated and stored as a Lab-VIEW measurement data file. The computer controller program when executed acquired this Lab-VIEW measurement file and generated a waveform. The waveform controlled the amplifier output and therefore the pump output and thereby producing physiological flow in the flow phantom. Examples of the program generated steady and physiological waveforms are shown in figure 3.12(a) and 3.12(c) respectively, and the response observed in the straight wall-less phantom using PW spectral Doppler are shown in figure 3.12(b) and 3.12(d) respectively.

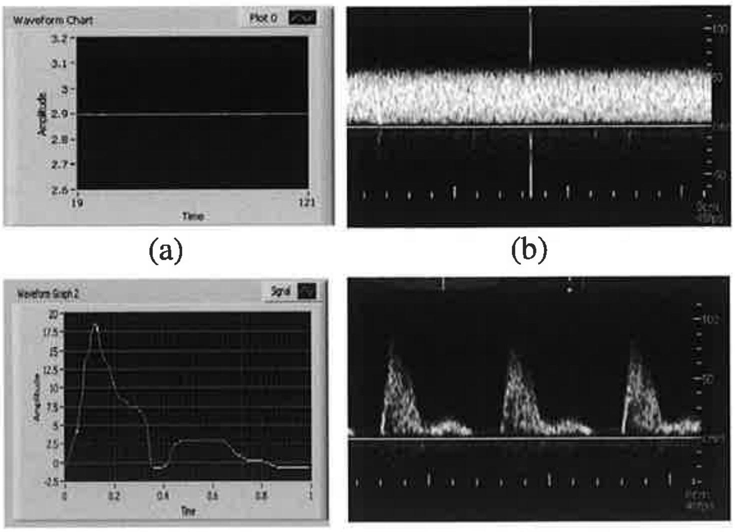

(a) (b)

(c) (d)

Figure 3.12 (a) Graphical User Interface (GUI) of the Lab-VIEW program showing a steady flow waveform (b) steady flow waveform response observed in the straight wall-less phantom using PW spectral Doppler (c) GUI of the Lab-VIEW program showing a physiological flow waveform (d) physiologic flow waveform response observed using PW spectral Doppler

Inlet length and selection of tubing

In order to maintain a laminar flow in the flow phantoms during the flow experimentation, the selection of an appropriate tube connecting the pump output to the flow phantom inlet port, which maintained sufficient inlet length was important. Beyond the inlet length, the steady velocity profiles or time-varying velocity profiles are stable with distance. The inlet length (*L*) was determined using Equation 3.3 [12]

$$L = 0.04 D R_e \qquad \text{Equation 3.3}$$

$$R_e = \frac{\rho v D}{\mu} \qquad \text{Equation 3.4}$$

where *D* is inner tube diameter (6.8cm), R_e Reynolds Number determined using equation 3.4, where v is mean velocity used (40cms^{-1}), ρ is density of BMF (1.037 gm cm^{-3}) and μ is viscosity of BMF (0.041gm cm^{-1} s^{-1}).

The inlet tubing was made from tygon and had external and internal diameter of 7.4 mm and 7.1 mm, respectively. This inner diameter was the closest available match to the actual renal artery diameter of 6.8 mm in the healthy volunteer. The inlet tube was mounted on a heavy wooden bench and maintained as straight as possible. Both the flow phantom and the pump were mounted on separate adjustable stands as shown in figure 3.11. The pump system, connecting the tubing (in particular the inlet tube) and the flow phantom were all maintained at the same height.

The BMF was circulated through the flow phantom using a steady flow of a velocity of 40 $\mathrm{cms^{-1}}$ produced in the flow phantoms for steady flow experiments or a physiological flow of a velocity between 2-40 $\mathrm{cms^{-1}}$ produced in anatomically realistic renal flow phantoms for physiological flow experiments. The temperature of the flow phantom and the BMF was maintained at 22 ± 1° C throughout the experiments.

3.4.2 B-mode and PW Spectral Doppler Optimisation

A Siemens Antares ultrasound system with a broadband curvilinear transducer (C 5-2), was used for the flow visualisation in Colour Doppler mode and for determining BMF velocity using PW Spectral Doppler mode during the flow experimentations. The curvilinear transducer was clamped to a micrometer manipulator mounted on a translational stage. The vessel lumen was imaged first using B mode. The transducer was angled to produce a beam-to-vessel angle of 60^0. A direct physical contact of the transducer surface with the phantom was avoided through the use of a scanning well. The scanning well consisted of a 20 mm thick layer of degassed water- glycerol (10% glycerol and 90% water) solution. The angled transducer was positioned such that the transducer face was covered with the water- glycerol solution in the scanning well and did not touch the phantom surface. The transducer therefore, could be easily translated in the x-y plane, without introducing any mechanical pressure on the phantom surface. The speed of sound in a) the water glycerol solution and b) agar based TMM at 20^0C were 1540 $\mathrm{cms^{-1}}$ and 1541 ± 3 $\mathrm{ms^{-1}}$, respectively [51]. Therefore, the water-glycerol solution provided a continuous medium of the same speed of sound for the ultrasound beam travelling from transducer surface into the phantom and eliminated any loss of ultrasound transmission into the phantom due to air gaps. The transducer position was adjusted to visualise the arterial lumen at the centre of the computer screen an the imaging depth was maintained as 10 cm. The B-mode image was optimised by positioning the focal zone at the centre of the vessel, maximizing the output power, represented by a Mechanical Index (M.I.) of 0.7 while the TGC control was adjusted to produce a uniform image of the phantom. The PW Spectral Doppler mode was turned on and the settings to optimize the spectral waveform were adjusted. The specific values of are presented in Table 3.2.

Table 3.2 Spectral Doppler settings

Imaging mode	Renal
Sample Volume size	1 mm
Doppler angle (Beam-vessel angle)	60^0
Output power	100%
Doppler gain	65%
Wall-filter setting	47 Hz (low)
pulse repetition frequency (PRF)	adjusted to set velocity scale in appropriate range without aliasing

The BMF velocity information in the sample volume was obtained from the Doppler velocity spectrum. The peak systolic and peak diastolic velocities were determined by manually positioning the cursor at the appropriate maximum and minimum positions within the spectra and furthermore were obtained at regular axial and radial intervals.

3.4.3 Basic flow experimentation studies

Basic flow experiments were performed to investigate steady flow velocity profiles in a) straight wall-less flow phantoms (normal and 30% stenosis and b) anatomically realistic wall-less renal flow phantoms (normal and 30% stenosis) and also physiological flow velocity profiles in c) straight wall-less flow phantom (normal and 30% stenosis).

I. Protocol for investigation of steady flow velocity profiles in straight wall-less flow phantom (normal and 30% stenosis) and anatomically realistic wall-less renal artery flow phantoms (normal and 30% stenosis)

A steady velocity of 40 cms^{-1} was developed in a normal straight wall-less flow phantom. The B-mode and PW Spectral Doppler settings were maintained as described in section 3.4.2. The range gate was initially positioned along the central axis of the lumen. The maximum and minimum velocities were determined from Doppler spectrum at regular axial and radial interval of 10 mm and 1 mm respectively across the entire vessel lumen. A coloured contour plot representing the radial distance along the x-axis, axial distance along the y-axis and the maximum velocity along the z-axis was plotted from the measured data. The flow experiments, following the same protocol, were performed in the 30% stenosis straight wall-less flow phantom, the normal renal artery flow phantom and the 30% stenosis renal flow phantoms and the velocity contours were plotted for each of them.

II. Protocol for investigation of physiological flow velocity profile in straight wall-less flow phantom (normal and 30% stenosis)

A physiological velocity of between 2 - 60 cms^{-1} was developed in a normal straight wall-less flow phantom. The B-mode and PW Spectral Doppler settings were maintained as described in section 3.4.2. The range gate was initially positioned at the centre of the vessel lumen. The peak systolic and peak diastolic velocities were determined at regular axial and radial interval of 10 mm and 1 mm, respectively, across the entire vessel lumen. A coloured contour plot representing the radial distance along the x-axis, axial distance along the y-axis and the systolic velocity along the z-axis was plotted. A similar procedure was repeated for 30% stenosis renal flow phantom.

3.4.4 Physiological flow experimentation in anatomically realistic renal flow phantoms

The physiological velocity profiles were investigated in a range of anatomically realistic renal flow phantoms with normal, 30%, 50% and 70% symmetrical stenosis and 25%, 35% and 45% asymmetrical stenosis, respectively. A physiological velocity of between 2 - 40 cms^{-1} was produced in each phantom and the geometric stability of the model was assessed as explained in section 3.3.5. The stable models which did not show any signs of TMM rupture or BMF leakage were selected for physiologic flow experiments.

A physiological velocity of between 2 - 40 cms^{-1} was maintained in the normal anatomically realistic renal phantom. The B-mode and PW Spectral Doppler settings were maintained as described in section 3.4.2. The systolic and diastolic velocities were determined at regular axial and radial intervals of 1mm across the entire renal lumen as shown in figure 3.13.

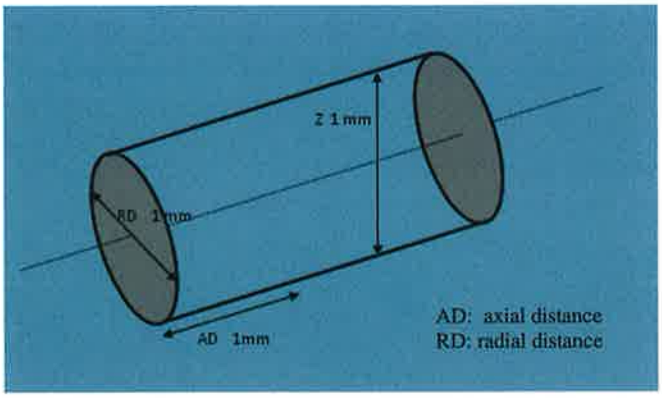

Fig 3.13 Axial and radial intervals selected in renal artery flow phantom

The radial positions, along the x-axis and z-axis were controlled using micrometer manipulator adjustment and the range gate positioning, respectively. The axial position, along the y-axis was controlled by micrometer manipulator positioning on the translational stage. The systolic velocities measured across the entire axial (y axis) and radial intervals (x-axis), with the range gate maintained along the central axis were plotted in the form of a coloured contour plot with the velocity represented as a colour. The physiological velocity profiles were investigated in each stenosis model of the of the renal artery flow phantom using the same measurement protocol.

3.4.5 Uncertainties in the velocity measurement

The overall uncertainty in the velocity measurement was determined on the basis of the systematic and the random uncertainties in the velocity measurement using the Equation 3.5.

$$\text{Overall uncertainity} = [(\text{Systematic uncertainity})^2 + (\text{Randon uncertainity})^2]^{1/2} \qquad \text{Eq. 3.5}$$

The sources of systematic uncertainties were calibration of pump and velocity resolution. The pump used for circulation of BMF was calibrated using time weighted collection of the BMF and the uncertainity in the calibration of pump was determined based on the uncertainties in the tachometer and stop-watch measurement used while calibrating the pump. The velocity resolution of Siemens Sonoline Antares system in Spectral Doppler mode was ± 0.3 cms^{-1}. The sources of random uncertainties include transducer positioning and electronic calliper positioning. These random uncertainties were determined by i) repositioning the transducer and ii) repositioning the electronic calliper on the maximum velocity pixels of velocity spectrum- displayed on the system's monitor for five times and determining the velocities each time and the standard error in the velocity measurement due to random uncertainities. The overall uncertainty in velocity measurement was estimated from random and systematic uncertainties using Equation 3.5.

3.4.6 Flow visualisation in Colour Doppler mode

A higher degree of stenosis introduces more complicated flow features such as turbulence and reverse flow in the post-stenosis region. These flow features can be visualised in Colour Doppler mode. In clinical practise, Colour Doppler is used to guide the clinician to the area of stenosis. The physiological flow developed in the renal flow phantoms was visualised using the Colour Doppler mode. Colour Doppler images of the renal flow phantoms were captured to compare the flow behaviour in the presence of the various degrees of blockages.

The flow was imaged in Colour Doppler mode using the Siemens Antares ultrasound system with a broadband curvilinear transducer (C5-2). Colour Doppler images were optimised for renal imaging by adjusting the instrument controls or settings. The instrument settings are given in Table 3.3. The same settings were maintained throughout the study and Colour Doppler images were obtained for each of the renal flow phantoms.

Table 3.3 Colour Doppler instrument control settings

Imaging depth	10 cm
Focal zone position	Near or below the vessel
Doppler angle (Beam-vessel angle)	60^0
Colour Doppler gain	1 dB
output power	63%
Persistence	medium
pulse repetition frequency (PRF)	adjusted to set velocity scale in appropriate range

3.5 Investigation of effect of a fat mimicking layer on the velocity profile

The effect of varying fat layer thicknesses on the physiological velocity profiles was studied using a 20 mm and 30 mm layer of degassed olive oil. The speed of sound and attenuation value of the olive oil has been reported to be 1490 ms^{-1} and 0.29 $dBcm^{-1}MHz^{-1}$ respectively at 3 MHz [25]. The olive oil replicated a simple fat mimicking layer. The effect of such a fat mimicking layer on the renal velocity profiles was investigated by comparing the velocity profiles for three experimental conditions: a) without an oil layer b) with a 20 mm oil layer and c) with a 30 mm oil layer for each renal flow phantom. The protocol for the investigation of the physiological velocity profiles as described in section 3.4.4 was used to investigate the physiological velocity profiles in the presence of a fat mimicking layer, the water-glycerol solution in the scanning well was replaced by the degassed olive oil layer of thickness 20 mm. The B-mode and PW Spectral Doppler settings as described in section 3.4.2 were used. The introduction of the oil layer produced a shift in the range gate position by 1 mm. The range gate was positioned initially at the center of the vessel. The beam-to-vessel angle was adjusted to 60^0. The systolic and diastolic velocities were determined at regular axial and radial intervals of 1 mm each across the entire vessel lumen. A coloured contour plot representing the radial distance along the x-axis, axial distance along the y-axis and the systolic velocity along the z-axis was plotted. A fat mimicking layer of 30 mm was then achieved by adding a further 10 mm olive oil layer in the scanning well to form a 30 mm thick layer. The transducer position in the scanning well was maintained at 30 mm (i.e. touching the oil layer surface). The range gate position was again initially adjusted to maintain it at the centre and the beam-vessel angle was adjusted to 60^0. The B-mode and PW Spectral Doppler settings were kept constant. The same protocol as previously described for 20 mm oil layer was repeated and the colour velocity contour was plotted. The protocol for all three experimental conditions was followed and the physiological velocity profiles for the three experimental conditions were investigated in each of the seven renal artery flow phantoms.

3.6 Investigation of the effect of a fat mimicking layer on shape and profile of physiological Spectral Doppler waveform

The effect of a fat mimicking layer on the shape and profile of the physiological Spectral Doppler waveform was studied by analysing the physiological waveforms using the ImageJ (version 1.40g, National Institutes of Health, USA) software package. The physiological Spectral Doppler waveform, in the normal renal artery flow phantom, was observed in PW spectral Doppler mode with the optimised settings. The physiological Spectral Doppler waveform displayed on the scanner's monitor was captured as an image using the systems image capturing facility. Images were captured for all three experimental conditions: a) without fat mimicking layer b) with fat mimicking layer of 20 mm thickness and c) with fat mimicking layer of 30 mm thickness. The procedure was repeated and the images of the physiological Spectral Doppler waveform at the location of the stenosis in each of the anatomically realistic renal flow phantoms for all three experimental conditions were captured. All of the captured grey scale images were converted into TIFF format and saved for offline analysis. Once opened in ImageJ software, the intensity and velocity information for two regions peak stenosis region (region 1) and the diastolic velocity region (region2), (shown in figure 3.14), were determined as follows:

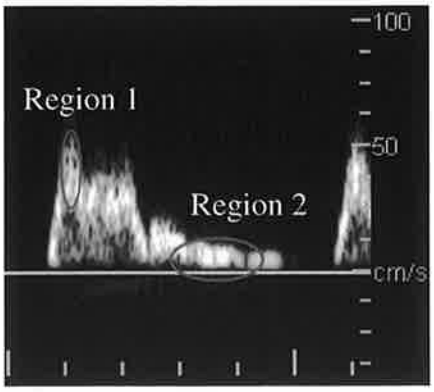

Fig 3.14 Physiological waveform analysis regions

The intensity of the pixels was manually determined by positioning the cursor at the pixel of interest with the intensity of the selected pixel being displayed on the active window in ImageJ software. The velocity of the pixel was identified using the velocity scale to the right of the waveform image. The intensity versus velocity information was obtained for 10 - 15 pixels for region1 and region 2 for all three experimental conditions. The intensity versus velocity data was plotted for all the three experimental conditions for regions, 1 and 2 respectively. The intensity and velocity data plotted for all three experimental conditions were compared in all the renal artery flow phantoms and the effect of the fat mimicking layer on the physiological Spectral waveform was analysed. The effect of the fat mimicking layer on the shape of the physiological velocity waveforms was analysed on the basis of visual observations of the shape.

Chapter 4 Results

4.1 Introduction

This chapter presents the results of the experimental work and the analysis carried out in the thesis. Sections 4.2 and 4.3 include the results of development of the straight wall-less flow phantoms and anatomically realistic renal flow phantoms respectively. The velocity profiles, investigated by flow experimentation using these phantoms, are presented in sections 4.4 and 4.5. Section 4.6 presents the physiological velocity profiles in the renal artery flow phantoms in the presence of the fat mimicking oil layer of varying thicknesses. The effect of the fat layer on the physiological Spectral Doppler waveform is presented in section 4.7.

4.2 Development of straight wall-less flow phantoms

Figure 4.1 shows the B-mode images of (a) normal and (b) 30% stenosis straight wall-less flow phantoms. The normal straight wall-less flow phantom represented a straight wall-less vessel of diameter of 6.8 mm as shown in figure 4.1(a). In the 30% stenosis straight wall-less flow phantom, a symmetrical stenosis was developed over an axial length of 10 mm, at the centre of the wall-less vessel, as shown in figure 4.1(b). B-mode images were acquired using the linear transducer (5-13MHz) on a Siemens Antares system.

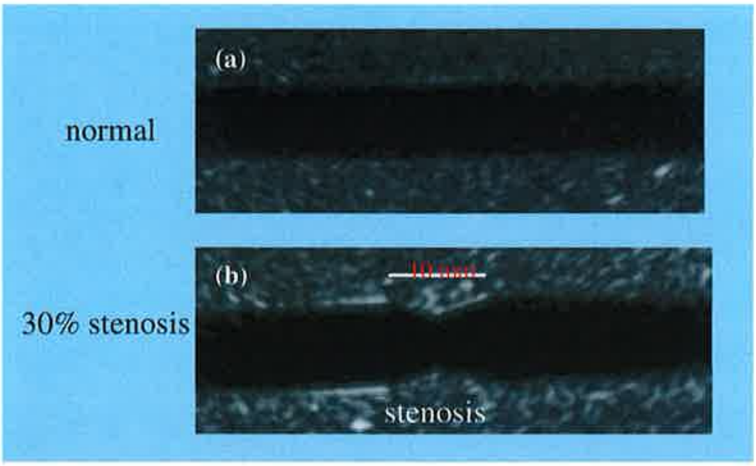

Figure 4.1 B-mode images of (a) normal (b) 30% symmetrical stenosis straight wall-less flow phantoms

4.3 Development of anatomically realistic renal flow phantoms

The range of anatomically realistic renal artery flow phantoms developed using the methodology described in section 3.3 and the B-mode images are shown in figure 4.2. The figure 4.2 (a) shows the inlet of the normal renal artery flow phantom while figures 4.2 (b-d) shows the inlet of the renal artery flow phantoms with the 30%, 50% and 70% symmetrical stenosis. Figure 4.2 (e-g) shows the inlet of the renal artery flow phantoms with 25%, 35% and 45% asymmetrical stenosis. The stenosis in each case was constructed at the proximal end of the wall-less vessel, just before the bend, over an axial distance of 10 mm.

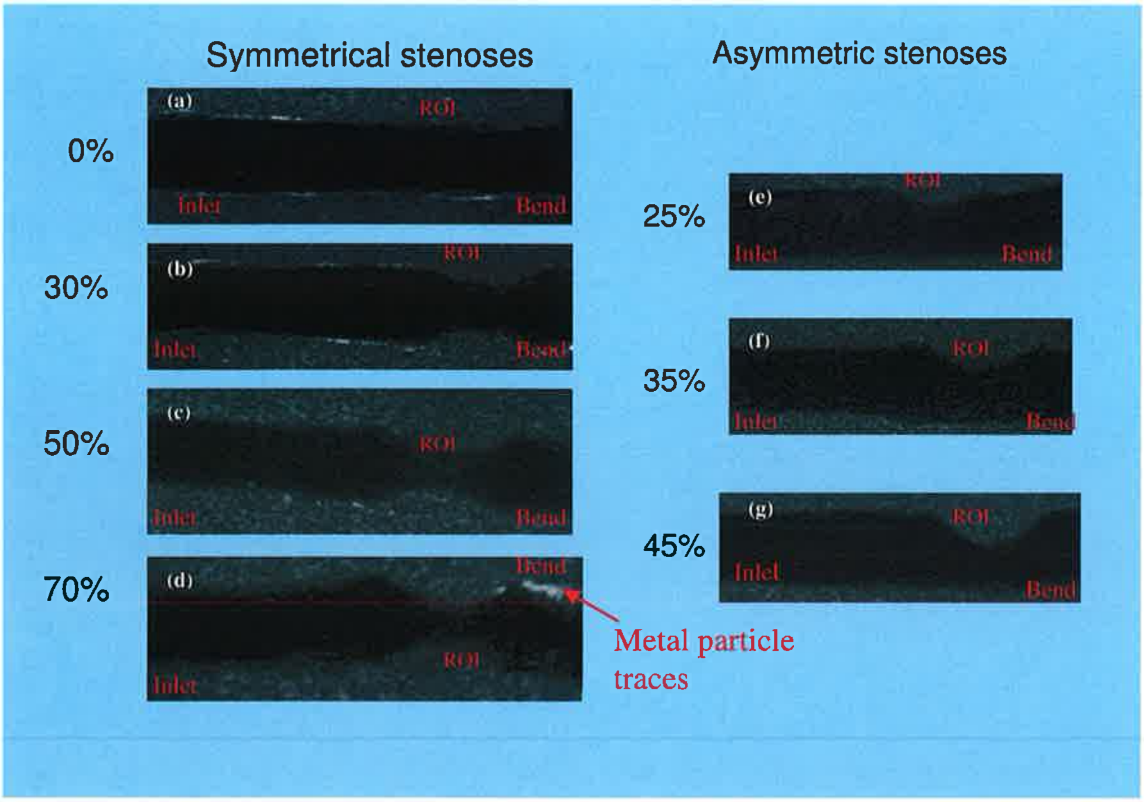

Figure 4.2 B-mode images showing the inlet of renal artery flow phantoms with varying degrees of stenoses (a) normal artery; (b) 30%,(c)50% and (d) 70% symmetrical stenoses; (e) 25%, (f) 35% and (g) 45% asymmetrical stenoses)

Particles of the low melting alloy which accumulated around the inner wall of the vessel during the construction of renal artery flow phantoms were removed by circulating hot water in the constructed renal flow phantoms, as described in section 3.3.3. Some traces of metal were still observed in the curvature region in 70 % renal artery flow phantom as shown in figure 4.2 (d).

4.3.1 Geometric accuracy findings in the flow phantom development

The geometric accuracy of the flow phantom development was determined by comparing the renal artery diameters measured at two different stages of development: a) at the metal core/model stage and b) the final renal lumen diameter in the flow phantom. The results for the renal artery metal model diameter measured at three sites for all metal models are presented in Table 4.1. Three metal models of each type of stenosis were selected and the metal model diameter was measured using a vernier callipers (accuracy ± 0.01 mm).

Table 4.1 Renal artery metal model diameter in [mm] (measured at three sites)

Metal model	Measurement site 1- at stenosis (± 0.01 mm)				Measurement site 2- near inlet (± 0.01 mm)				Measurement site 3- near outlet (± 0.01 mm)			
symmetric stenosis	**1**	**2**	**3**	**mean**	**1**	**2**	**3**	**mean**	**1**	**2**	**3**	**mean**
0%	6.86	6.85	6.88	**6.86**	6.85	6.88	6.89	**6.87**	6.86	6.88	6.91	**6.88**
30%	4.76	4.75	4.78	**4.76**	6.85	6.87	6.89	**6.87**	6.84	6.87	6.86	**6.86**
50%	3.40	3.42	3.43	**3.41**	6.84	6.85	6.86	**6.85**	6.85	6.85	6.86	**6.85**
70%	2.09	2.06	2.06	**2.07**	6.84	6.85	6.87	**6.85**	6.85	6.86	6.84	**6.85**
asymmetric stenosis	**1**	**2**	**3**	**mean**	**1**	**2**	**2**	**mean**	**1**	**2**	**3**	**mean**
25%	5.12	5.12	5.15	**5.13**	6.87	6.85	6.87	**6.86**	6.85	6.86	6.86	**6.86**
35%	4.45	4.43	4.43	**4.44**	6.85	6.91	6.86	**6.87**	6.85	6.86	6.84	**6.85**
45%	3.75	3.75	3.76	**3.75**	6.85	6.85	6.88	**6.86**	6.85	6.86	6.87	**6.86**

The results for the renal lumen diameter measured at three different sites in the renal flow phantoms are presented in table 4.2 represented. The renal lumen diameters were measured from B-mode images of the renal flow phantoms using ultrasound system's electronic callipers (accuracy ± 0.1 mm). The B-mode images were acquired using linear transducer (5-13 MHz) on a Siemens Antares system and three observations were recorded for each measurement site.

Table 4.2 Renal artery flow phantom (lumen) diameter in [mm] – measured using B-mode images

Stenosis model	Measurement site 1- at stenosis (± 0.1 mm)				Measurement site 2- near inlet (± 0.1 mm)				Measurement site 3- near outlet (± 0.1 mm)			
symmetric stenosis	**1**	**2**	**3**	**mean**	**1**	**2**	**3**	**Mean**	**1**	**2**	**3**	**mean**
0%	6.9	6.9	6.8	**6.9**	6.9	6.9	6.9	**6.9**	6.9	7.0	6.9	**6.9**
30%	4.7	4.8	4.8	**4.8**	6.9	6.9	6.9	**6.9**	6.9	6.9	6.9	**6.9**
50%	3.4	3.4	3.4	**3.4**	6.8	6.8	6.9	**6.8**	6.8	6.8	6.8	**6.8**
70%	2.1	2.1	2.0	**2.1**	6.8	6.8	6.9	**6.8**	6.8	6.9	6.8	**6.8**
asymmetric stenosis	**1**	**2**	**3**	**Mean**	**1**	**2**	**2**	**Mean**	**1**	**2**	**3**	**mean**
25%	5.1	5.1	5.1	**5.1**	6.8	6.9	6.9	**6.9**	6.9	6.9	6.9	**6.9**
35%	4.5	4.4	4.5	**4.5**	6.9	7.0	6.9	**6.9**	6.8	6.9	6.9	**6.9**
45%	3.8	3.8	3.7	**3.8**	6.9	6.9	6.9	**6.9**	6.9	6.9	6.9	**6.9**

To assess the geometric accuracy of the flow phantom development, the metal model measurement and the renal lumen diameters measured in the B-mode images were statistically compared using a paired t-test. Ten observations for the diameter measured at the above mentioned stages were recorded and using a paired t-test the corresponding p values were determined, these p values are presented in table 4.3

Table 4.3 The p values calculated from a paired t-test for each metal model and phantom lumen

Stenosis model	p value (at stenosis-site 1)	p value (measurement site 2)	p value (measurement site 3)
symmetric stenosis			
0%	0.87	0.59	0.21
30%	0.92	0.47	0.09
50%	0.19	1.00	0.19
70%	0.92	0.67	0.46
asymmetric stenosis			
25%	0.09	0.40	0.07
35%	0.43	0.58	0.43
45%	0.75	0.54	0.15

In the paired t-test, the null hypothesis being tested was that there was no difference in the diameters of renal artery model determined at the two different stages. If $p<0.05$, then the null hypothesis was rejected indicating a significant difference. The p values determined in all of the cases were greater than 0.05 except for 25% asymmetrical stenosis renal model, where the p values were observed reaching to the significance. The p values reaching to the significance (in this particular case) could be a result of the hand-polishing technique (described in section 3.3.2) applied to the metal models of renal artery to produce a smooth surface finish. Nevertheless, the statistically insignificant difference between the renal artery metal model diameter and the renal lumen diameter measured in the B-mode images observed in all other cases emphasised that the phantom development method was reliable and the renal artery flow phantoms developed for flow experimentation were geometrically accurate.

4.3.2 Geometric stability assessment of stenosis models

The geometrical stability of the stenoses model renal artery flow phantoms was assessed on the basis visual observations used to identify any signs of the TMM fracture or the BMF leakage in the flow phantoms, as explained in section 3.5.3. During the assessment, for the initial two hours in the lower grade (<50%) stenoses flow phantoms, no signs of the TMM rupture or of the BMF leakage were observed and therefore, the normal and 30% symmetrical stenosis renal artery flow phantoms were found to be stable through the experimentation procedure. Similar stable behaviour was exhibited by the 25%, 35% and 45% asymmetric stenoses renal artery flow phantoms. The 50% wall less renal flow phantom ruptured at the vessel curvature after 3 days of experimentation. As a result, three 50% wall less renal artery flow phantoms were utilised to complete the flow experiments. The 70% renal artery flow phantom could not withstand the pressure generated and was ruptured at the stenosis location after 5 hours of experimentation on the first day. In total, five 70% renal artery flow phantoms were used to complete the flow experiments. The renal lumen diameters at the stenosis measured in each renal artery flow phantoms after one hour and four hours of continuous physiological flow were observed identical and therefore, the stenosis geometry in the renal artery flow phantoms was found to be stable during the flow experimentation.

From the assessment of the geometrical stability of the stenosis models, it was evident that the constructed stenosis models of renal artery flow phantoms could be used for the physiological flow experiments using velocities between 2 - 40 cms^{-1}.

4.3.3 Acoustic characterisation of TMM samples

The TMM samples poured and set during the construction of straight wall-less flow phantoms and the anatomically realistic renal artery flow phantoms were acoustically characterised to determine their speed of sound and attenuation coefficient using the in-house SAM system described previously in section 3.3.6. The speed of sound (c) and attenuation coefficient (α) values of the TMM samples are provided below in Table 4.4.

Table 4.4 acoustic properties of the TMM – measured at 7.5 MHz

Sample number	Speed of sound (ms^{-1}) ± 3 ms^{-1}	Attenuation coefficient ($dBcm^{-1}MHz^{-1}$) ± 0.03 ($dBcm^{-1}MHz^{-1}$)
1	1552	0.49
2	1548	0.52
3	1553	0.48
4	1551	0.47
5	1549	0.52
6	1548	0.51
7	1546	0.50
IEC TMM [49] (2-10 MHz)	1540 ± 15	0.5 ± 0.05

The acoustic properties of the TMM samples were within a valid range and compared favourably with the quoted values for the IEC TMM.

4.4 Basic flow experiments

The basic flow experiments were performed and the steady velocity profiles of velocity 40 cms^{-1} in: 1) the straight wall-less flow phantoms with a normal lumen and a 30% symmetrical stenosis and 2) the anatomically realistic renal flow phantoms with a normal lumen and 30% symmetrical stenosis were investigated, following the protocol described in section 3.4.3 (I). Further, the physiological velocity profiles using a physiological velocity of between 2-60 cms^{-1} in the straight wall-less flow phantoms with a normal lumen and a 30% symmetrical stenosis were also investigated, following the protocol described in section 3.4.3 (II). In the following sections, the velocity profiles are represented as coloured contour diagrams. The error (standard error (SE)) in the velocity measurement was ± 1.3 cms^{-1} (SE) or 3% (percentage error (PE)), determined using the Equation 3.5 described in section 3.3.5.

4.4.1 Steady velocity profiles in the straight wall-less flow phantoms

Figure 4.3 shows the steady velocity profiles in the normal and the 30% symmetrical stenosis straight wall-less flow phantoms. The scale for both contour diagrams is between 50 to 90 cms^{-1}.

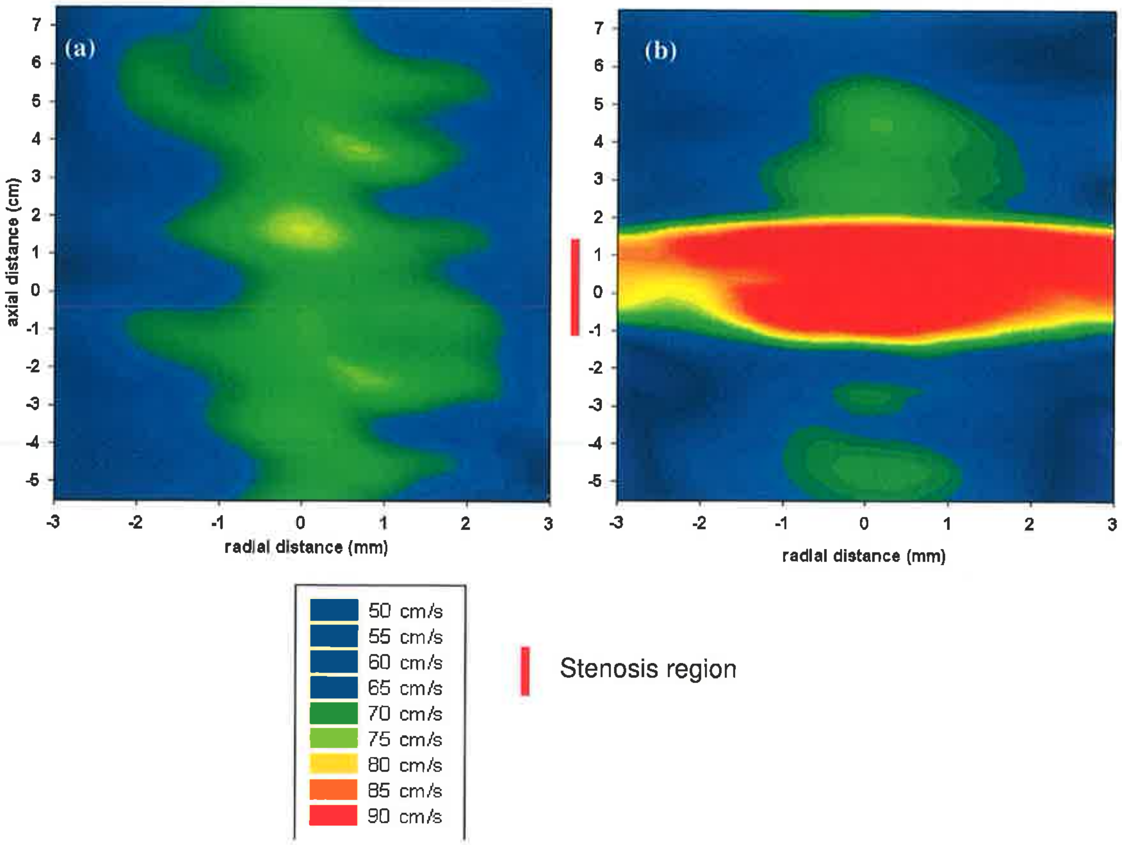

Figure 4.3 Steady velocity profiles in (a) normal and (b) 30% stenosis straight wall-less flow phantoms

In the velocity profile of the normal straight wall-less flow phantom, the maximum velocities were in range of 50-71 cms^{-1}. The velocity determined along the central axis was the highest and reduced slowly as a function of distance across the lumen radius. The radial velocity profiles at all the axial planes exhibited a parabolic velocity pattern as shown in figure 4.3 (a). In the velocity profile of the 30% stenosis straight wall-less flow phantom, shown in figure 4.3 (b), the same general features of the steady flow were observed except for an increase in the maximum velocity up to 87 cms^{-1} at the stenosis region. The higher velocities observed at stenosis rapidly decreased in the post stenosis region and resumed the parabolic velocity profile after an axial distance of 2 cm as illustrated in figure 4.3 (b).

4.4.2 Steady velocity profile in the anatomically realistic renal artery flow phantoms

Figure 4.4 shows the steady velocity profiles in the normal lumen and the 30% symmetrical stenosis renal artery flow phantoms. The stenosis was developed over an axial region of -0.5 cm to 0.5 cm. The vessel curvature occurred in the axial region of 1.5 cm to 2.5 cm, as indicated by vertical blue line in the figure. The scale in both contour plots was between 50 to 90 cms^{-1}.

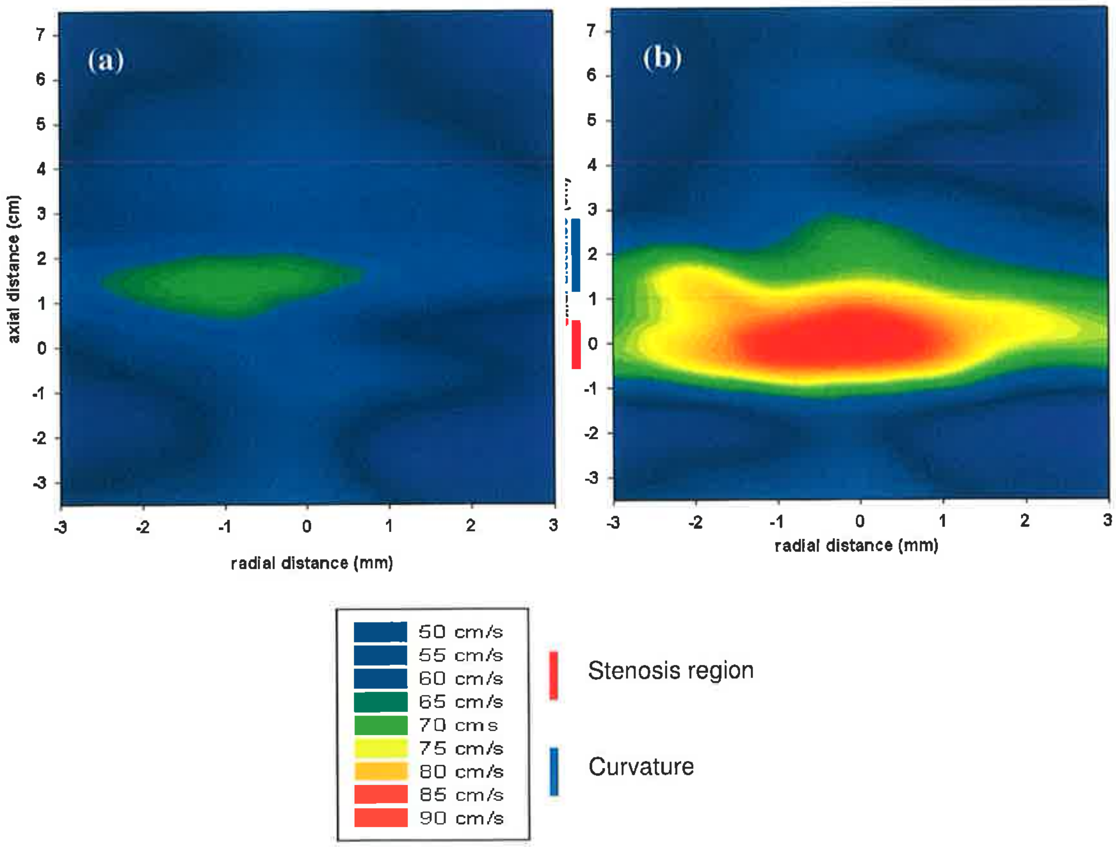

Figure 4.4 Steady velocity profiles in (a) normal and (b) 30% stenosis renal artery flow phantoms

In the steady velocity profile in the normal renal artery flow phantom, the velocities determined across entire axial length before the curvature were observed to be in the range of 50 - 63 cms^{-1}. The trend of the flow observed in this region was similar to that observed in normal straight wall-less flow phantom. At the vessel curvature (axial distance 15 - 25 mm), the measured velocities were found to be slightly higher in the range of 60 - 72 cms^{-1} and concentrated more towards the outer vessel curvature decreasing slowly in the radial plane. A slight skewing of the velocity profile towards outer vessel wall was observed. In the 30 % stenosis renal artery flow phantom, the velocities were elevated up to 76 - 88 cms^{-1} at the stenosis region. The peak velocity observed was 88 cms^{-1} at the centre of the stenosis region. The velocity decreased slowly in the post-stenosis region and continued as a parabolic velocity profile after an axial distance of 2.5 cm as illustrated in figure 4.4(b).

4.4.3 Physiological velocity profiles in straight wall-less flow phantoms

Figure 4.5 shows the physiological velocity profile in the normal and the 30% symmetrical stenosis straight wall-less flow phantoms. The scale for both contour plots was identical between 60 to 105 cms^{-1}.

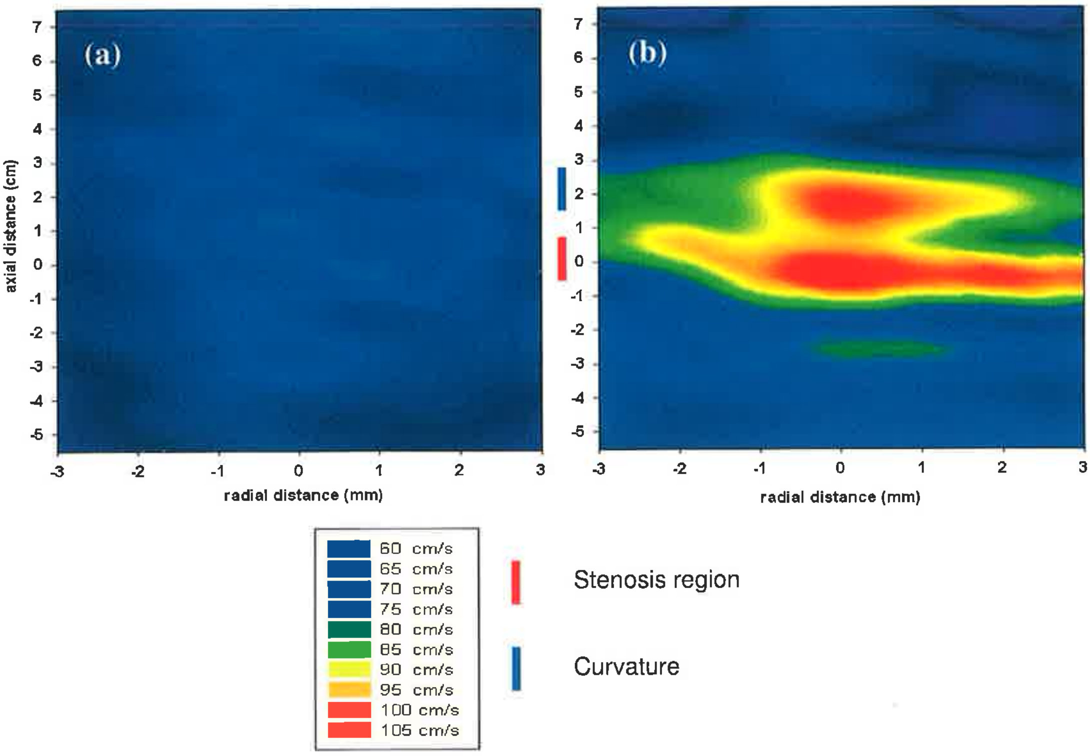

Figure 4.5 Physiological velocity profiles in (a) normal and (b) 30% stenosis straight wall-less flow phantoms.

Here, the measured velocity profiles were reasonably flat with the velocities in the range of 63- 75 cms^{-1}. In the 30% stenosis straight wall-less flow phantom, the velocities at the stenosis were observed in the range of 85 to 101 cms^{-1}. The velocities in the post-stenosis region were observed to be in the same range of 80 to 96 cms^{-1} up to an axial distance 2.5 cm (as shown in fig 4.5 (b)) and decreased slowly further downstream. The flat profile nature resumed after 3 cm along the axial length.

4.5 Physiological flow experimentation in the renal artery flow phantoms

4.5.1 Symmetrical stenosis models

Figure 4.6 [a-c] shows the physiological velocity profiles in the normal, the 30% and the 50% symmetrical stenosis renal artery flow phantoms. A common velocity scale of between 40 to 100 cms^{-1} was used for the contour plots to facilitate comparison of the velocity profiles. The error in the velocity measurement was ± 1.3 cms^{-1} (SE) or 3% (PE), determined using the Equation 3.5.

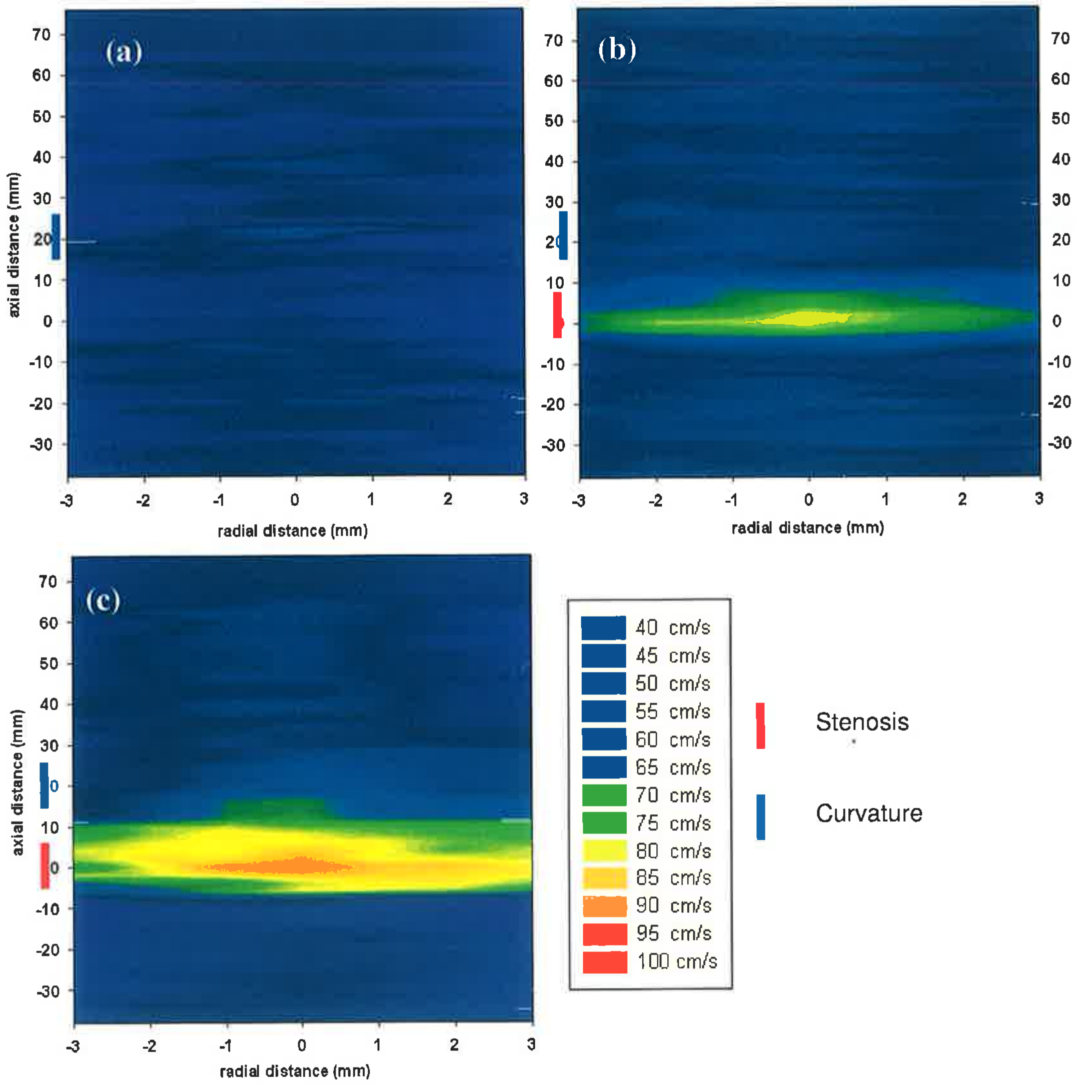

Figure 4.6 Physiological velocity profiles in (a) normal (b) 30% stenosis and (c) 50% stenosis renal artery flow phantoms

Figure 4.7 represents the physiological velocity profile in the 70% symmetrical stenosis renal artery flow phantom. A velocity scale of 40-145 cms^{-1} was selected for the contour plot in this case, given the considerably high flow rates measured in this phantom.

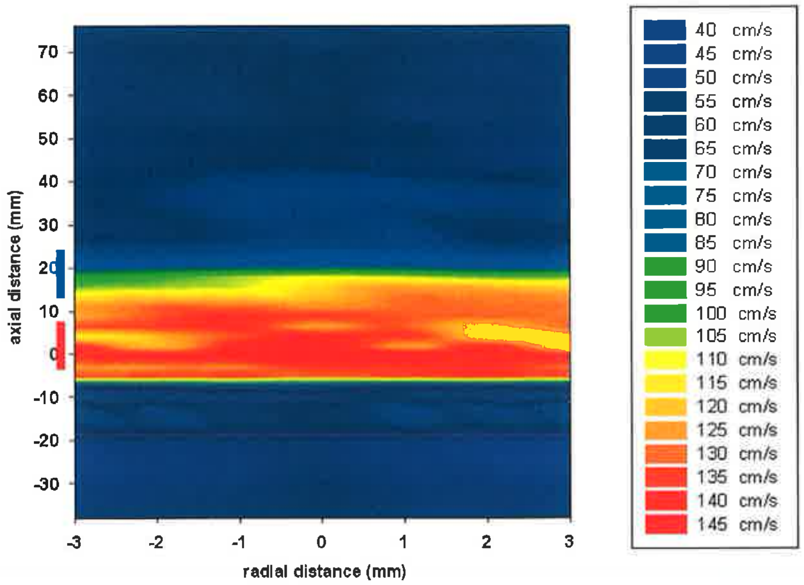

Figure 4.7 Physiological velocity profile in the 70% renal artery flow phantom

The physiological velocity profiles at the stenosis and the post-stenosis region was of main interest in all these physiologic velocity profiles investigated. In order to study the physiological flow characteristics in these regions in more detail, the physiological velocity profiles were plotted with greater velocity resolution for the stenosis and curvature regions only in the normal and the symmetrical stenosis models of 30%, 50% and 70%. The velocity profiles at the stenosis region and at the curvature region are presented in figure 4.8 and figure 4.9 respectively.

Flow observed at the stenosis region in the symmetrical stenosis renal artery flow phantoms

Figure 4.8[a-d] shows the physiological velocity contours, plotted only for the stenosis region in normal, 30%, 50% and 70% symmetrical stenosis renal artery flow phantoms. The stenosis was developed over an axial length of 10 mm in each of the renal artery flow phantoms.

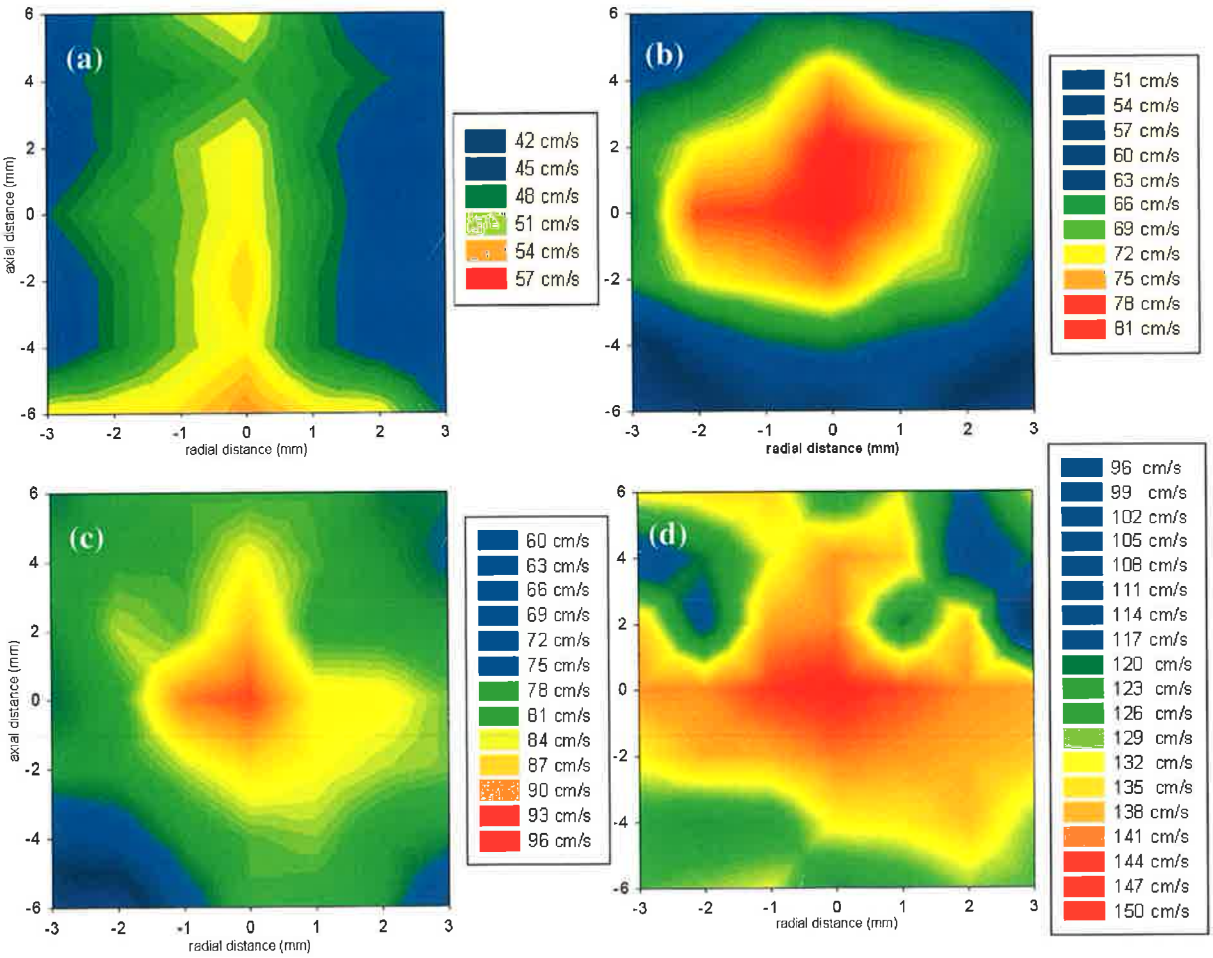

Figure 4.8 Physiological velocity profiles at the stenosis region in (a) normal (b) 30% stenosis (c) 50% stenosis and (d) 70% stenosis renal artery flow phantom

Flow observed at the vessel curvature in symmetrical stenosis renal artery flow phantoms

Figure 4.9[a-d] shows the physiological velocity contours, plotted specifically at the vessel curvature in normal, 30%, 50% and 70% symmetrical stenosis renal artery flow phantoms. The vessel curvature was observed at an axial distance of 15 mm to 25 mm (shown in figure3.8) in the renal artery flow phantoms.

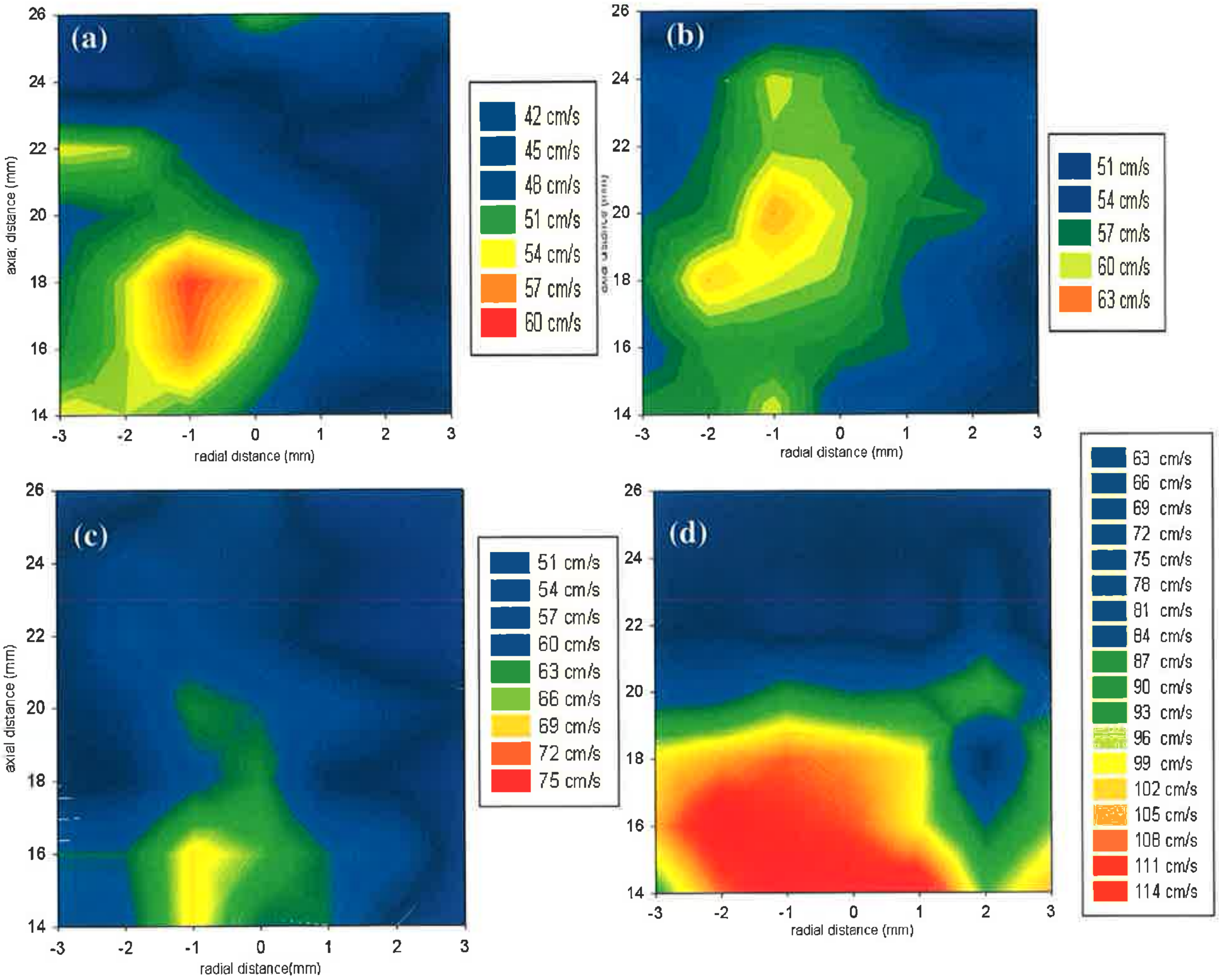

Figure 4.9 Physiological velocity profiles at the curvature in (a) normal (b) 30% stenosis (c) 50% stenosis and (d) 70% stenosis renal artery flow phantoms

The velocities in the physiological velocity profile of the normal renal artery flow phantom were measured in the range of 40 - 60 cms^{-1}. The velocity profile was flat in nature. The velocities determined at the vessel curvature were observed to be higher by 4 - 6 cms^{-1} compared to the central line velocity and showed a small degree of skewing towards the outer vessel curvature, as shown in fig 4.9 (a). The velocities in the physiological velocity profile of the 30% symmetrical stenosis renal artery flow phantom were measured to be in the range of 63- 78 cms^{-1}, as shown in figure 4.8 (b). The physiologic flow velocity profile was similar to the profile of normal renal artery flow phantom, except for slight increase in the velocities measured in a range of 63 - 76 cms^{-1} at the stenosis region. The peak velocity determined at stenosis region was 78 cms^{-1} and dropped very rapidly in the post-stenosis region, where the vessel regained its original diameter (6.8 mm) value. A slight skewing towards the outer vessel curvature was also observed, as shown in figure 4.9 (b). The higher velocities were observed at the vessel curvature in all radial planes up to the axial distance of 25 mm corresponding to the end of vessel curvature. A shift of the higher velocities, from vessel curvature towards the central axis was also observed after the curvature region. The velocity profile was blunt further downstream. The velocities at the stenosis region in the physiological velocity profile of the 50% symmetrical stenosis renal artery flow phantom were observed as being increasingly elevated up to a velocity 96 cms^{-1} as shown in figure 4.8 (c), dropping to 60-81 cms^{-1} in the post stenosis region. A small variation of velocities, ranging from 60-76 cms^{-1}, was observed at the vessel wall immediately following the stenosis region. This variation indicated a mixing of flow in at the vessel wall immediately following the stenosis. The velocities at the vessel curvature were observed in the range of 56 - 74 cms^{-1} as shown in figure 4.9 (c). In the physiological velocity profile of the 70% symmetrical stenosis renal artery flow phantom, the systolic velocities were extremely elevated in the range of 120-140 cms^{-1} as shown in figure 4.8 (d). A strong central flow with extreme velocities concentrated along the central axis was measured. The velocities remained strongly elevated, along the central axis, in the post-stenosis region. A wide variation of the velocities of 79 - 115 cms^{-1} was observed at the vessel wall and near the vessel wall region in the immediately following the stenosis and also in the curvature region as shown in figure 4.9 (d).

4.5.2 Asymmetric stenosis models

Figure 4.10[a-c] shows the physiological velocity profiles in the 25%, 35% and 45% asymmetrical stenosis renal artery flow phantoms. A common velocity scale of between 40 to 90 cms^{-1} was used for the contour plots to facilitate the direct comparison of the velocity profiles. The error in the velocity measurement was ± 1.3 cms^{-1} (SE) or 3% (PE), determined using the Equation 3.5.

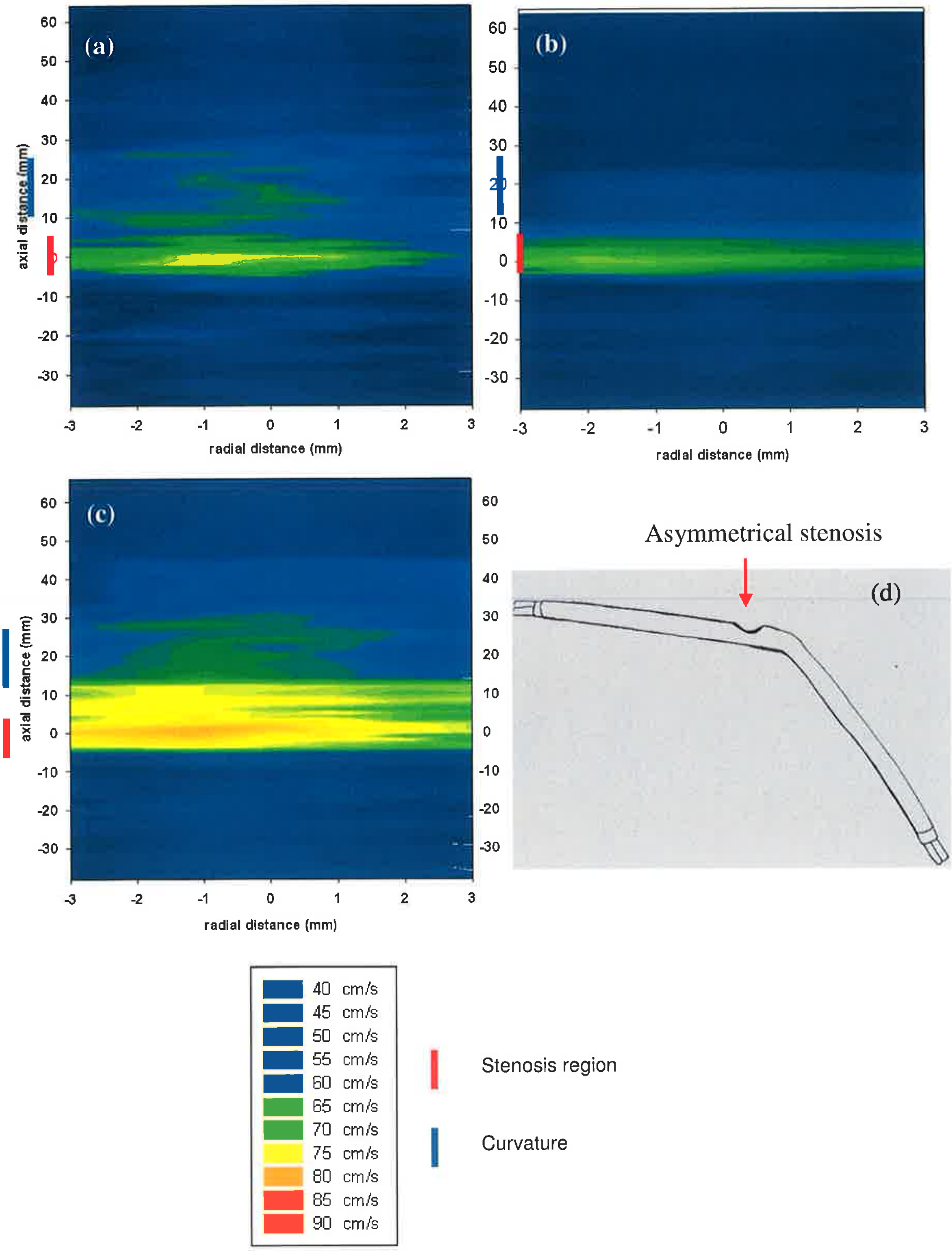

Figure 4.10 Physiological velocity profiles in (a) 25% (b) 35% and (c) 45% asymmetrical stenoses renal artery flow phantoms. (d) Position of asymmetrical stenosis in renal artery model

Flow observed at stenosis in asymmetrical stenosis renal artery flow phantoms

Figure 4.11 [a-c] shows the physiological flow velocity profiles, plotted for the stenosis region in the 25%, 35% and 45% asymmetrical stenoses renal artery flow phantoms. The stenosis was developed over an axial length of 10 mm in each of the renal artery flow phantoms.

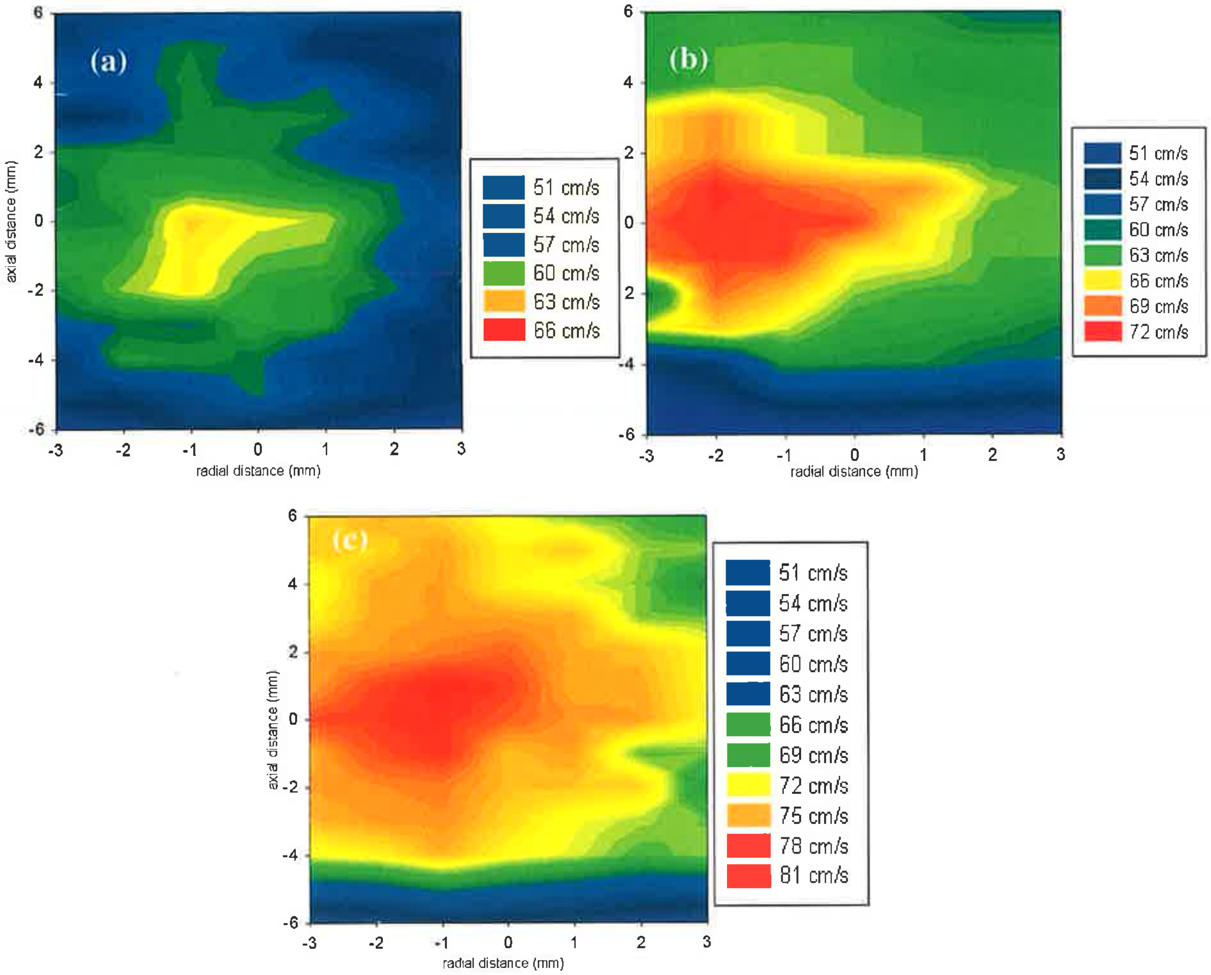

Figure 4.11 Physiological velocity profiles at stenosis region in (a) 25% (b) 35% and (c) 45% asymmetrical stenosis renal artery flow phantoms

Flow observed at curvature in asymmetrical stenosis renal artery flow phantoms

Figure 4.12 [a-c] shows the physiological velocity profiles plotted for the vessel curvature region in the 25%, 35% and 45% asymmetrical stenoses renal artery flow phantoms. The vessel curvature occurred over an axial distance of 15 mm to 25 mm as shown in figure3.8 in the renal flow phantoms.

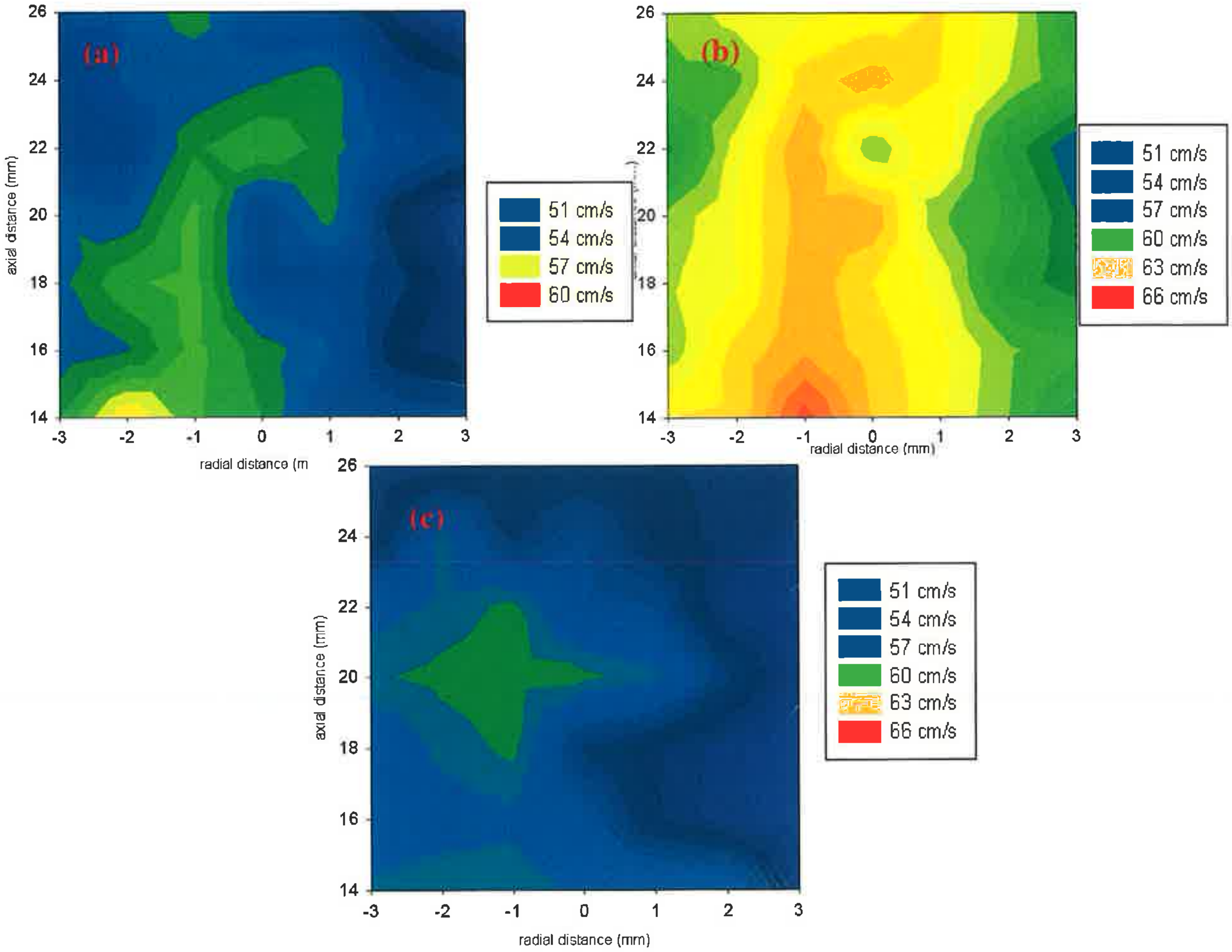

Figure 4.12 Physiological velocity profiles at curvature in (a) 25%, (b) 35% and (c) 45% asymmetrical stenosis renal artery flow phantoms

In the physiological velocity profile of the 25% asymmetrical stenosis renal artery flow phantom, the velocities at the stenosis region were observed in the range of 51-66 cms^{-1} and these higher velocities were observed to be slightly shifted towards the outer vessel wall, as shown in figure 4.11 (a). A small skewing of the velocity profile towards the outer vessel wall, at the vessel curvature was observed as shown in figure 4.12 (a). A similar behaviour was observed in the physiological velocity profile in the 35% asymmetrical stenosis renal artery flow phantom. The peak velocities measured at the stenosis region were in between 57 - 72 cms^{-1}, with a skewing towards the outer vessel wall as shown in figure 4.11 (b). The skewed nature of the velocity profile was also evident at the curvature with the velocities observed in between 56 – 67 cms^{-1} as shown in figure 4.12 (b). In the physiological velocity profile in 45% asymmetrical stenosis renal artery flow phantom, the velocities at the stenosis were elevated up to a velocity of 81cms^{-1} as shown in figure 4.11 (c). In the post stenosis region, the velocities at the outer and near the outer wall were observed to have a wide range of velocities between 45 - 73 cms^{-1}, indicating a mixing of the flow in this region as shown in figure 4.10 (c).

4.5.3 Flow visualisation in Colour Doppler mode

The flow at the stenosis and in the post-stenosis regions in each of renal artery flow phantom was visualised in Colour Doppler mode using the curvilinear transducer (C5-2) on a Siemens Sonoline Antares system. The settings in the Colour Doppler mode were maintained constant, as described in section 3.4.6. A physiological velocity between 2-40 cms^{-1} was used for the flow experiments. Figure 4.13[a-g] shows the Colour Doppler images of the physiological flow at the stenosis and in the post-stenosis region observed in the normal; the 30%, 50% and 70% symmetrical stenosis; and the 25%, 35% and 45% asymmetrical stenosis renal artery flow phantoms.

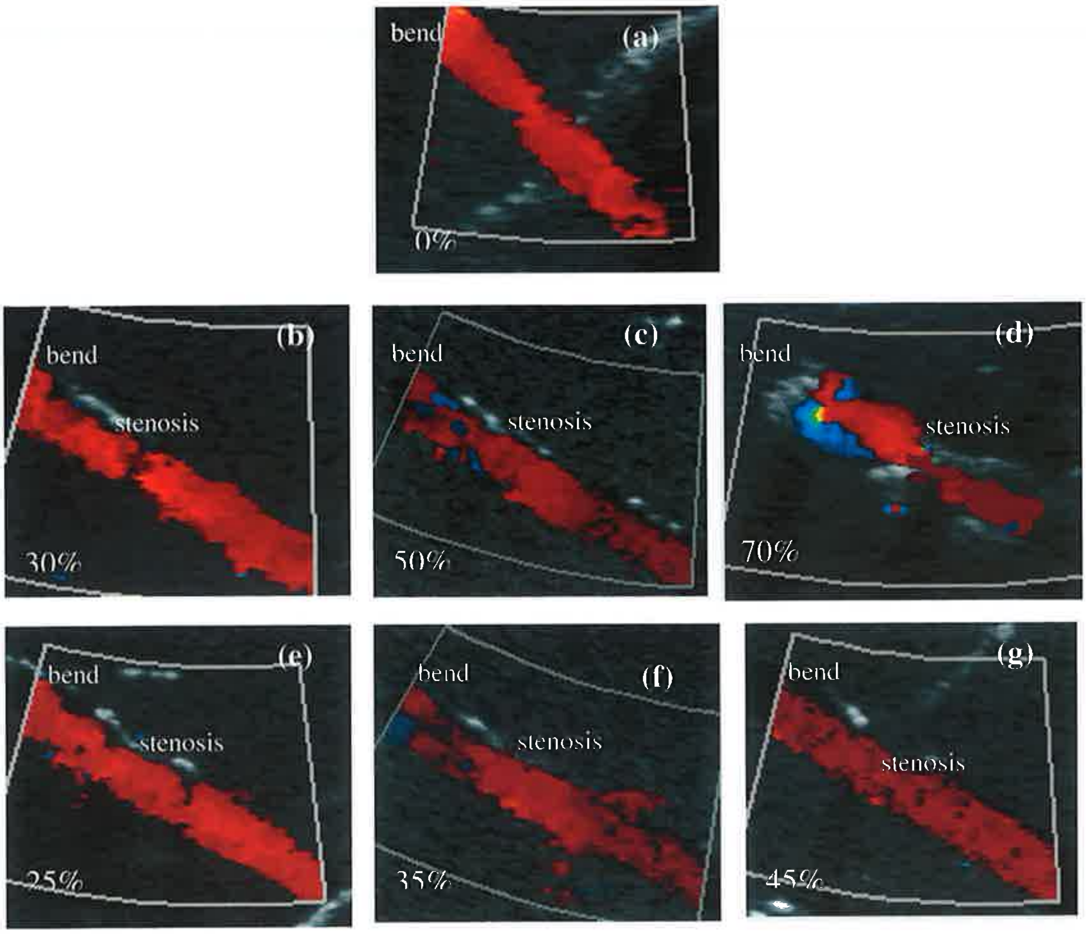

Figure 4.13 Colour Doppler images of the flow at stenosis and post-stenotic region in (a) normal (b) 30% symmetrical stenosis (c) 50% symmetrical stenosis (d) 70% symmetrical stenosis (e) 25% asymmetrical stenosis (f) 35% asymmetrical stenosis (g) 45% asymmetrical stenosis renal artery flow phantoms

In the 25%, the 45% asymmetrical stenosis and the 30% symmetrical stenosis renal artery flow phantoms the physiological flow didn't appeared to be disturbed after the stenosis region. However, a mixing type of flow was observed in the 35% asymmetrical stenosis and the 50% symmetrical stenosis renal artery flow phantoms. In the 70% symmetrical stenosis renal artery flow phantom, a strong mixing type of flow and reverse flow at the vessel walls, in the post-stenosis region was observed.

4.6 Effect of the fat mimicking oil layer of varying thicknesses on the physiological velocity profiles

The physiological velocity profiles were investigated in the presence of varying thicknesses of fat mimicking layer, as explained in section 3.5. The fat mimicking layer was produced using a degassed olive oil layer. In the normal and the 30% symmetrical stenosis renal artery flow phantoms, the physiological velocity profiles were investigated for the two experimental conditions: 1) without fat mimicking layer and 2) with fat mimicking layer of 20 mm thickness only. Figure 4.14 [a-b] and Figure 4.15 [a-b] show the physiological velocity profiles in normal and 30% symmetrical stenosis renal artery flow phantoms respectively, investigated for these two experimental conditions. In the 50% and the 70% symmetrical stenosis renal artery flow phantoms and the 25%, 35% and 45% asymmetrical stenosis renal artery flow phantoms, the physiological velocity profiles were investigated for the three experimental conditions: a) without fat mimicking oil layer b) with a fat mimicking oil layer of 20 mm thickness and c) with a fat mimicking layer of 30 mm thickness. The results are presented in Figure 4.16- 4.20. The error in the velocity measurement was ± 1.3 cms^{-1} (SE), determined using Eq. 3.5.

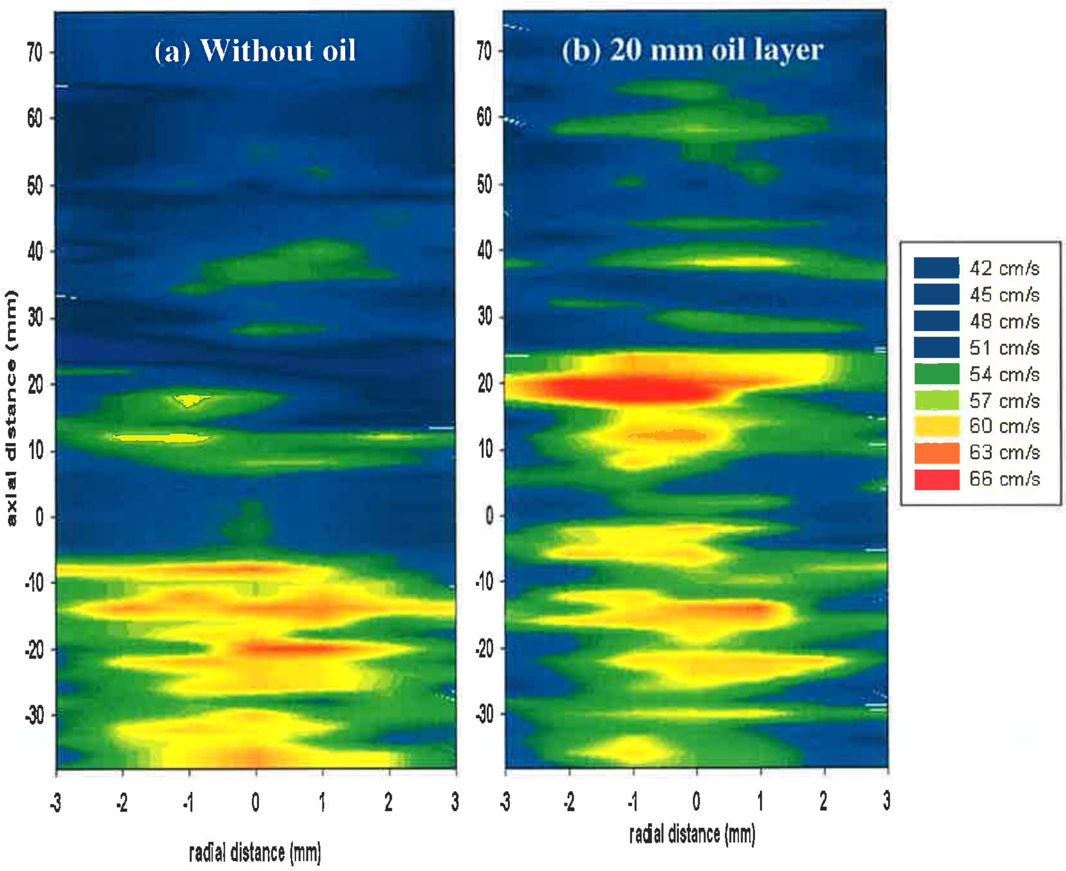

Figure 4.14 Physiological velocity profiles in the normal renal artery flow phantom (a) without fat mimicking layer and (b) with 20 mm thick fat mimicking layer

In the normal renal artery flow phantom, in the presence of a 20 mm thick fat mimicking layer, the velocities determined along the central axis and at the vessel wall were higher by 4 - 5 cms^{-1} and 2 - 4 cms^{-1} respectively, compared to the velocities determined without fat mimicking oil layer corresponding to an overestimation of between 4% - 12%.

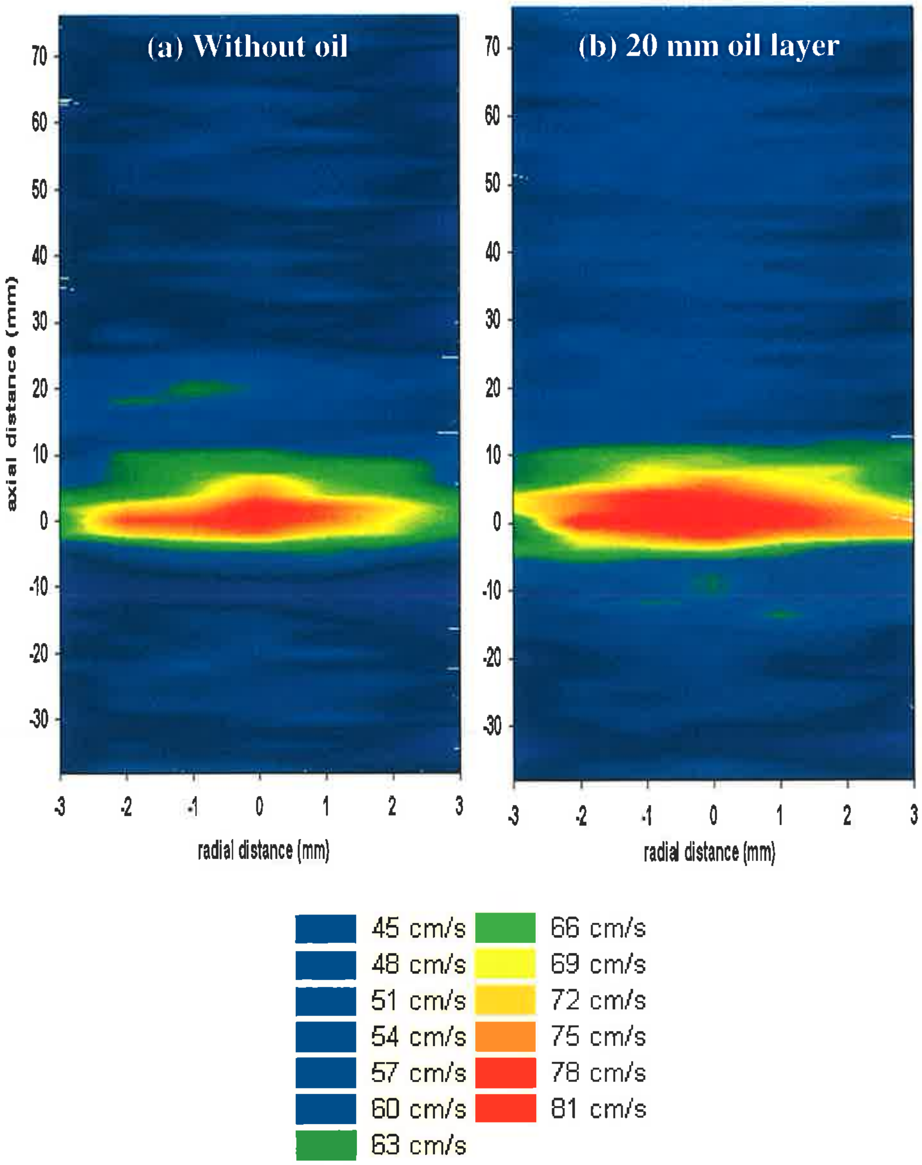

Figure 4.15 Physiological velocity profiles in the 30% symmetrical stenosis renal artery flow phantom (a) without fat mimicking layer and (b) with 20 mm thick fat mimicking layer

In the 30% symmetrical stenosis renal artery flow phantom, in the presence of 20 mm thick fat mimicking layer, the velocities determined along the central axis and at the vessel wall were higher by 4 - 5 cms^{-1} and 3 cms^{-1}, compared to the velocities without fat mimicking oil layer corresponding to an overerestimation of between 4%-13%.

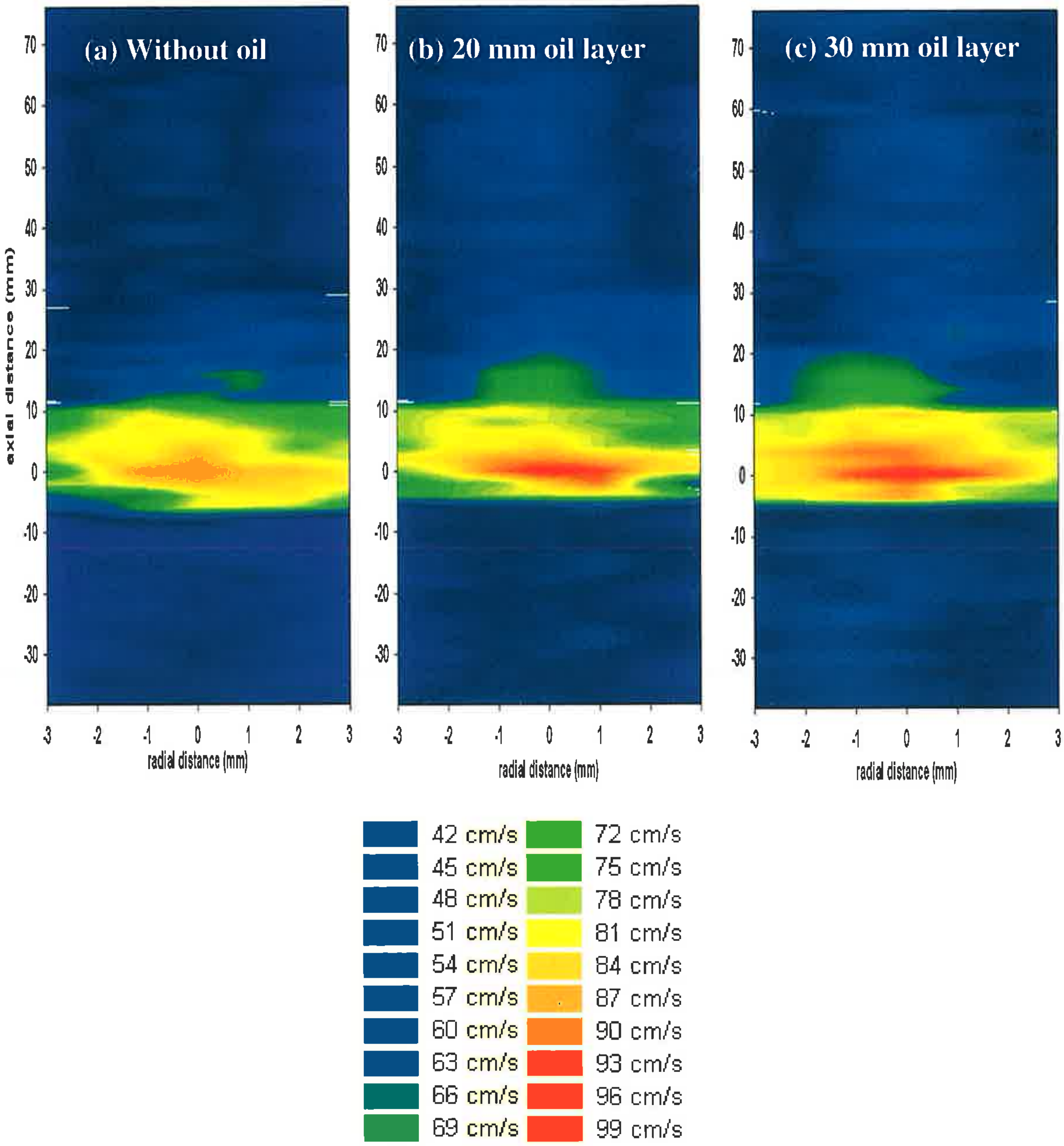

Figure 4.16 Physiological velocity profiles in the 50% symmetrical stenosis renal artery flow phantom (a) without fat mimicking layer, (b) with 20 mm thick fat mimicking layer (c) with 30 mm thick fat mimicking layer

In the 50% symmetrical stenosis renal artery flow phantom, in presence of 20 mm thick fat mimicking layer, the velocities determined along the central axis and at the vessel wall were higher by 4 - 5 cms^{-1} and 2 - 4 cms^{-1}, compared to the velocities without fat mimicking layer. With 30 mm thick fat mimicking oil layer, the velocities along the central axis and vessel wall were higher by 5 – 6 cms^{-1} and 3 – 6 cms^{-1}, compared to the velocities without fat mimicking layer corresponding to an overestimation of between 4% - 13% and 4% -18%. A similar trend of overestimating the velocities, in presence of fat mimicking layer, was observed in the other renal artery flow phantoms.

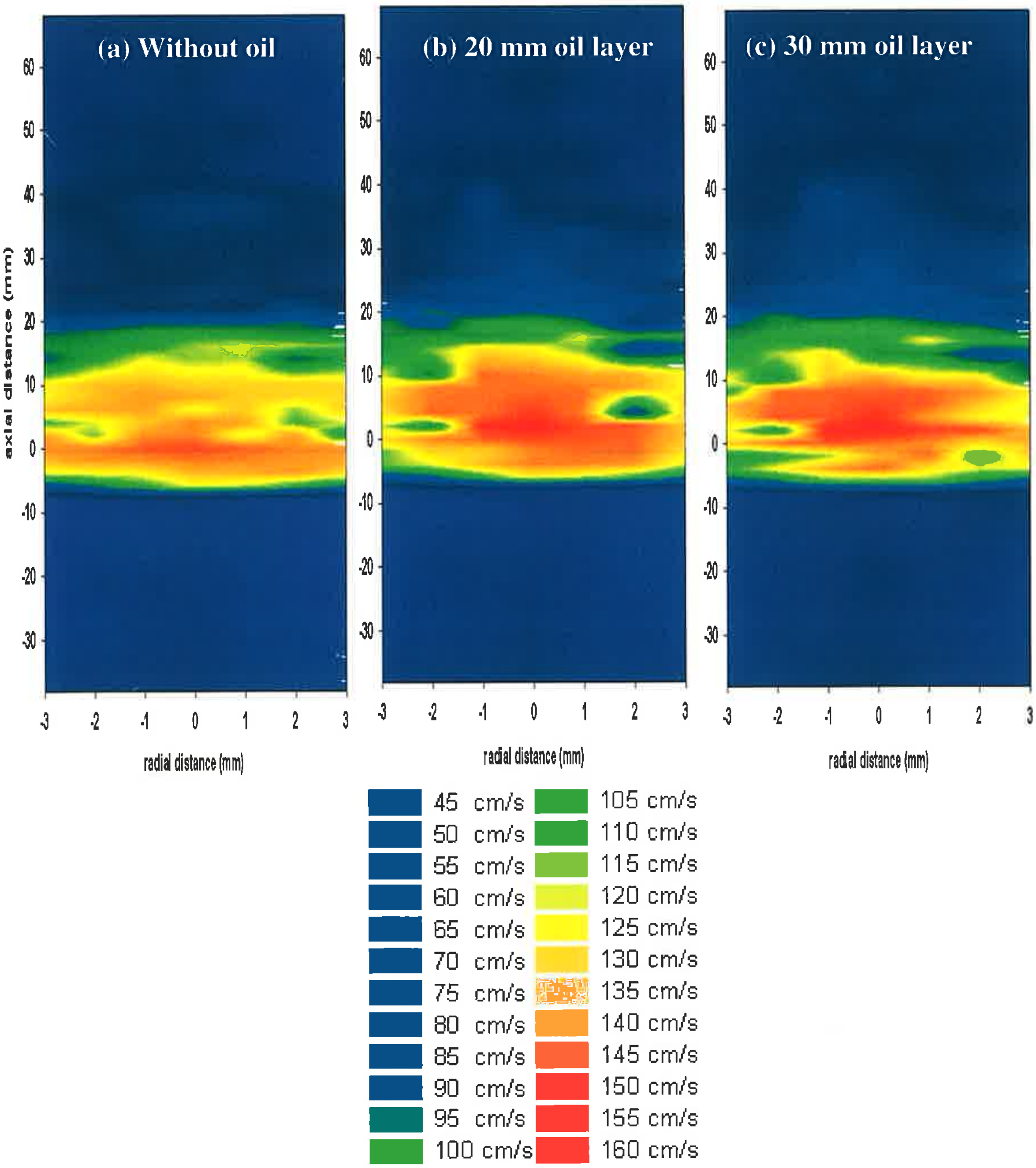

Figure 4.17 Physiological velocity profiles in the 70% symmetrical stenosis renal artery flow phantom (a) without fat mimicking layer (b) with 20 mm thick fat mimicking layer (c) with 30 mm thick fat mimicking layer

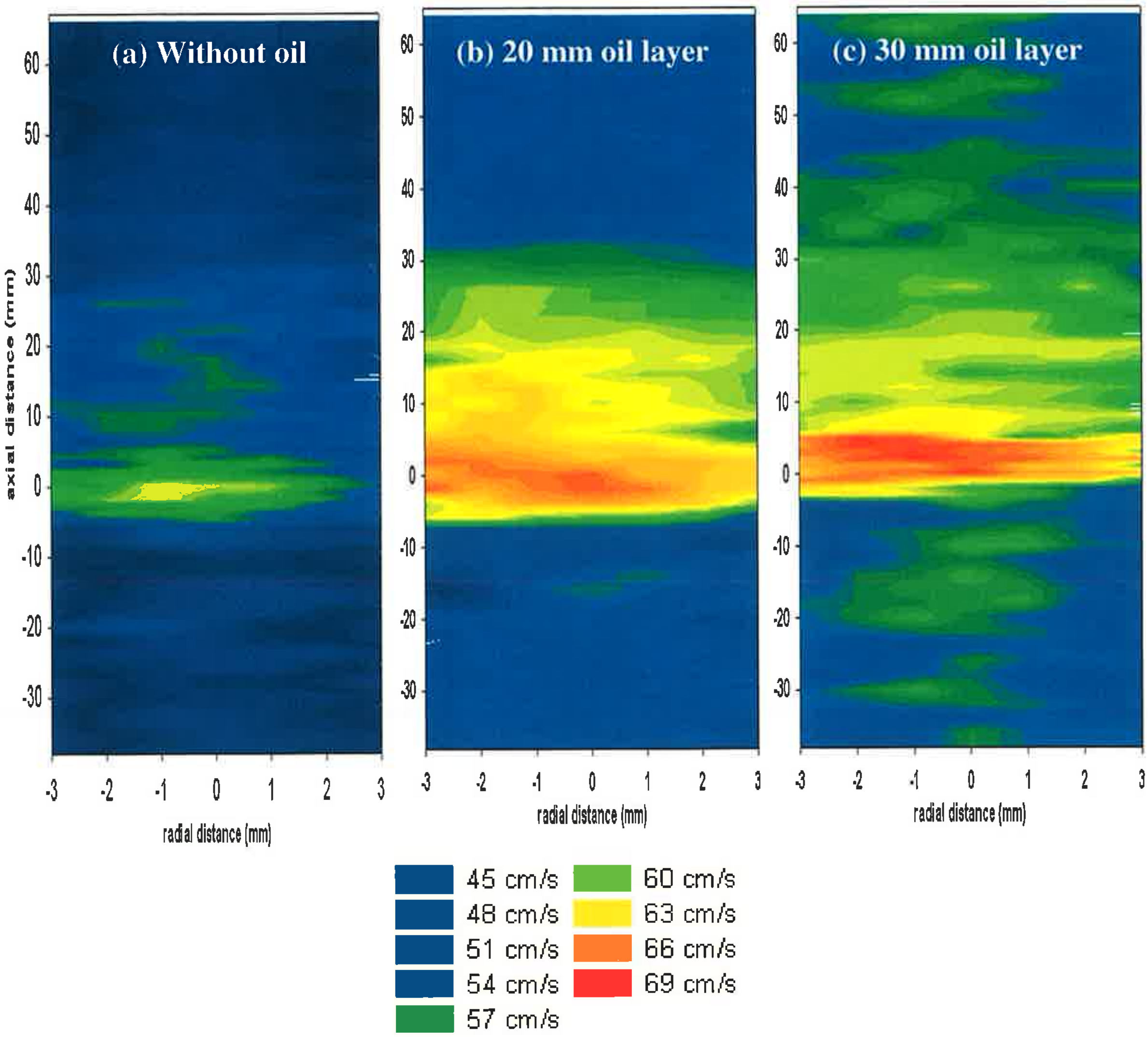

Figure 4.18 Physiological velocity profiles in the 25% asymmetrical stenosis renal artery flow phantom (a) without fat mimicking layer, (b) with 20 mm thick fat mimicking layer (c) with 30 mm thick fat mimicking layer

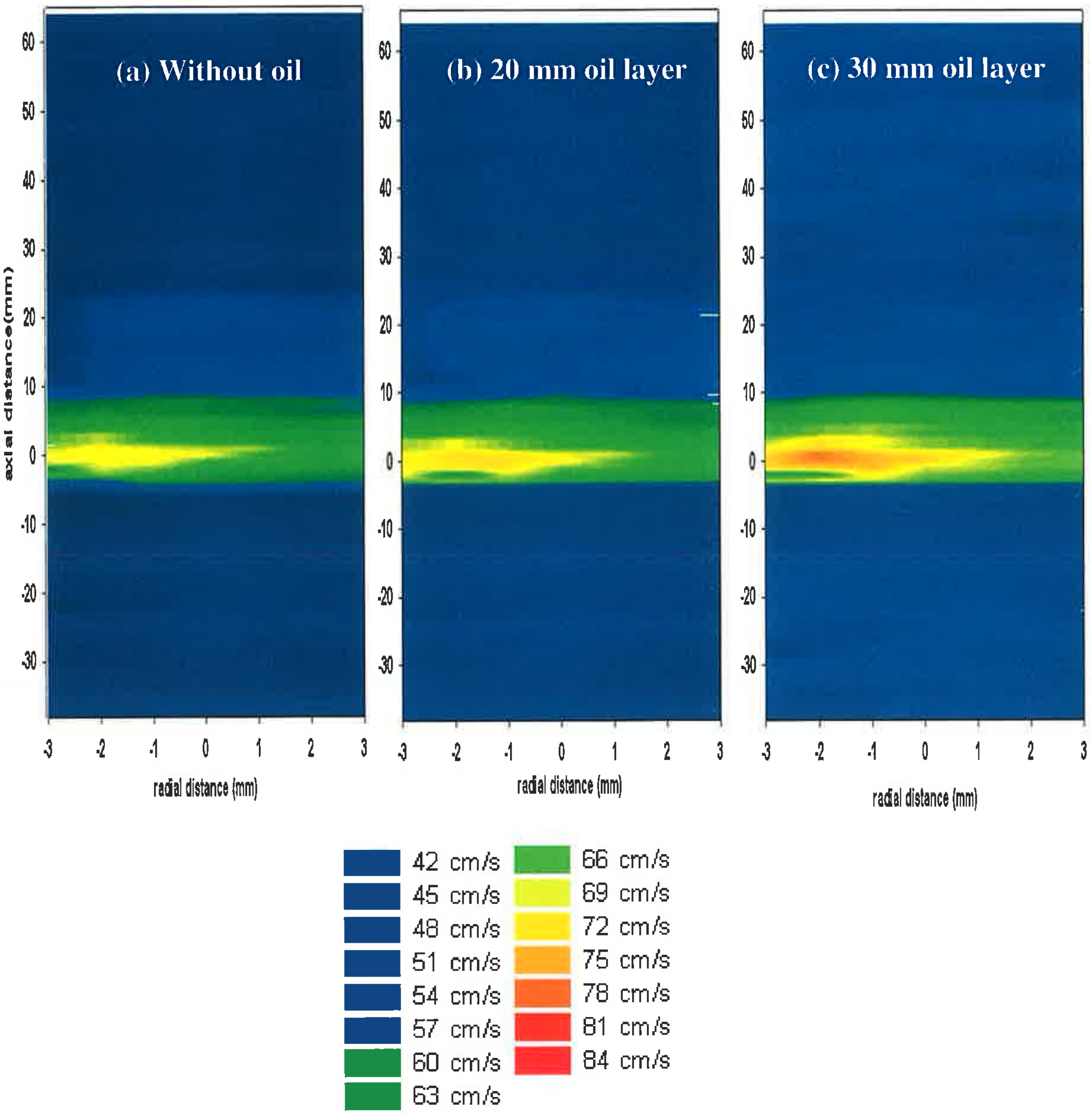

Figure 4.19 Physiological velocity profiles in the 35% asymmetrical stenosis renal artery flow phantom (a) without fat mimicking layer, (b) with 20 mm thick fat mimicking layer (c) with 30 mm thick fat mimicking layer

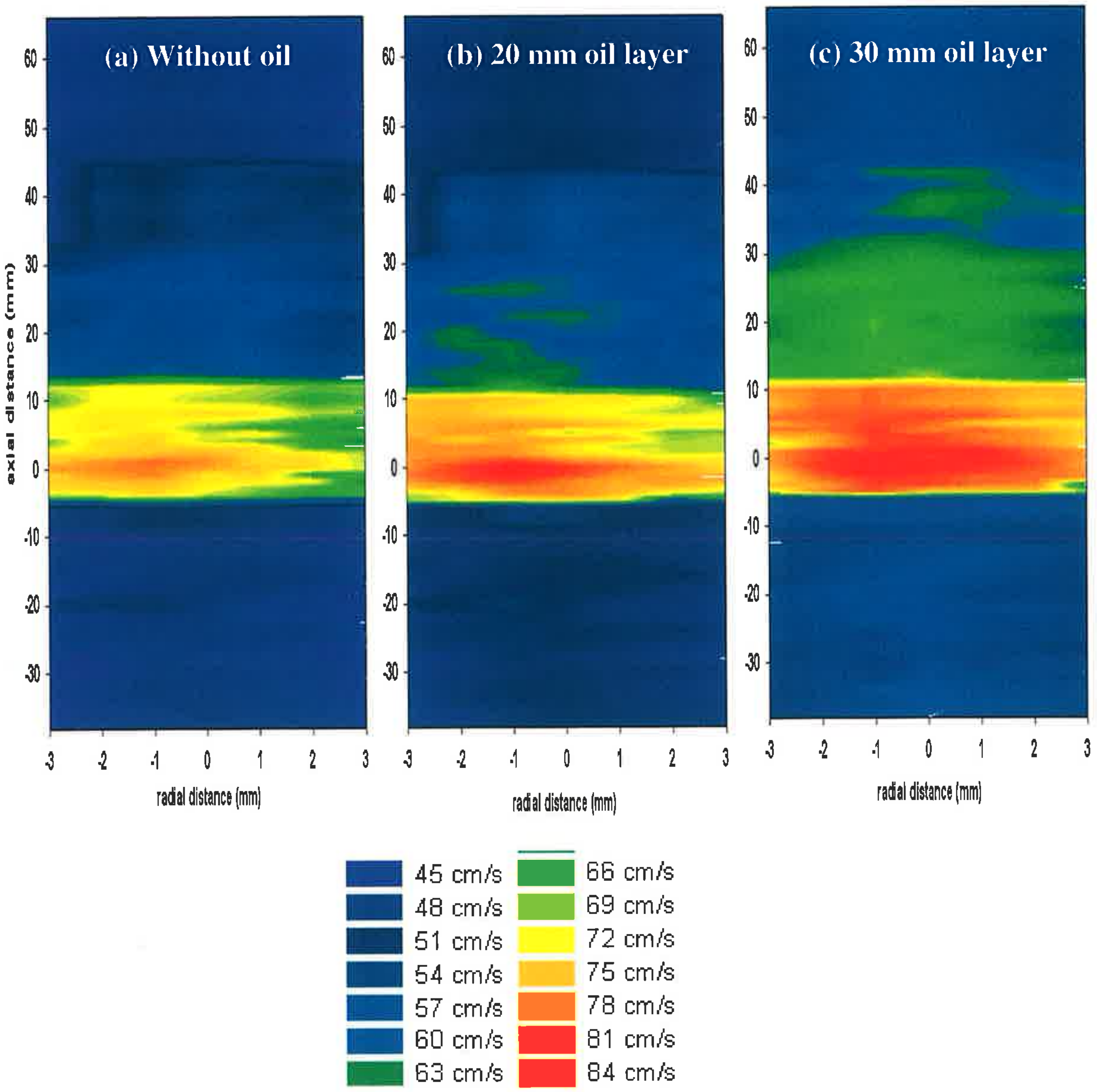

Figure 4.20 Physiological velocity profiles in the 45% asymmetrical stenosis renal flow phantom (a) without fat mimicking layer, (b) with 20 mm thick fat mimicking layer (c) with 30 mm thick fat mimicking layer

4.7 Effect of the fat mimicking layer on the physiological velocity waveform

The effect of the fat mimicking layer of varying thicknesses on the profile of the physiological velocity waveform was analysed using the methodology described in section 3.6. The physiological flow waveform observed under the three experimental conditions (without fat mimicking layer, with 20 mm fat mimicking layer and with

30 mm fat mimicking layer) in the normal, 25% asymmetrical stenosis and 30% symmetrical stenosis renal artery flow phantoms were studied.

Figure 4.21 shows the physiological velocity waveforms captured in the normal renal flow phantom for the three experimental conditions.

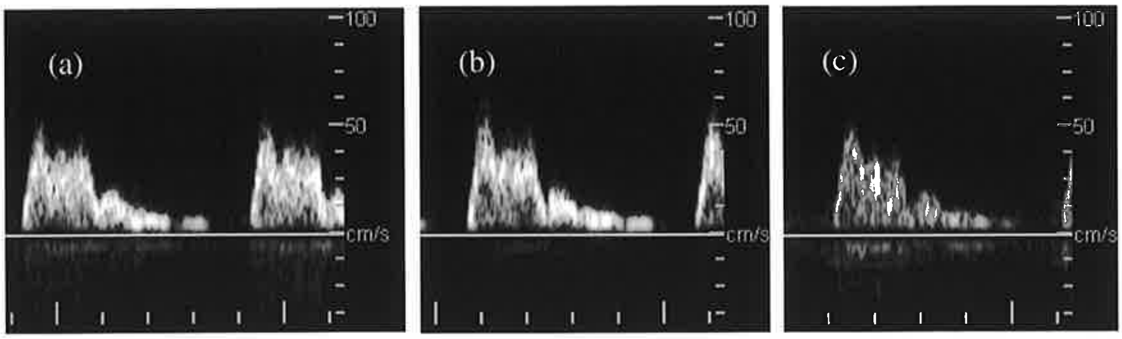

Figure 4.21 Physiological velocity waveform pictures in the normal renal flow phantom (a) without fat mimicking layer (b) with 20 mm thick fat mimicking layer (c) with 30 mm thick fat mimicking layer

Figure [4.22- 4.23] shows the plot of intensity versus velocity of the physiological velocity waveforms observed under the three experimental conditions, in the normal renal artery flow phantom, for region 1 and region 2.

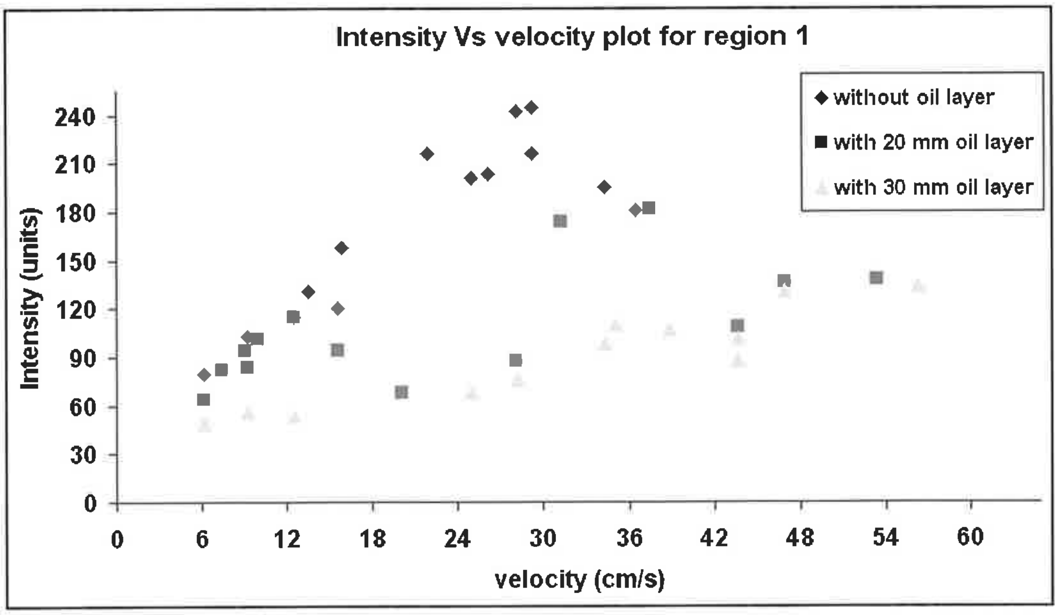

Figure 4.22 Intensity Vs Velocity plot in region 1 of physiological velocity waveforms observed in the normal renal artery flow phantom

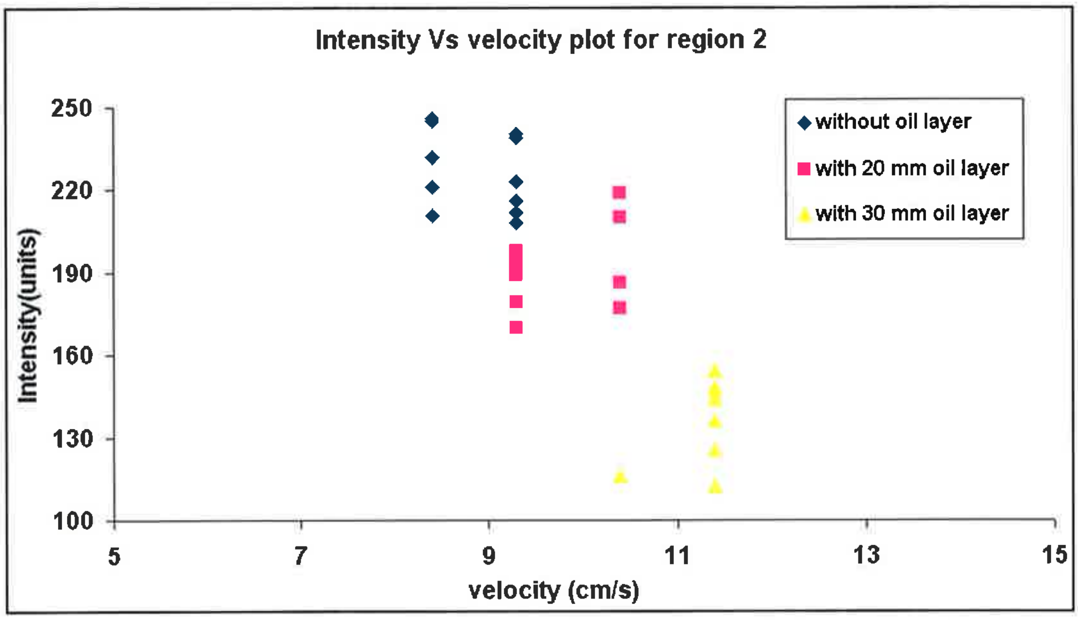

Figure 4.23 Intensity Vs Velocity plot in region 2 of physiological velocity waveforms observed in the normal renal artery flow phantom

In the intensity versus velocity plot of physiological velocity waveform observed in the normal renal artery flow phantom, for region 1 (figure 4.22), a decrease in the intensity values of the velocity data was observed for the 20 mm thick fat mimicking layer compared with the intensity values of the velocity data obtained without a fat mimicking layer. The intensities observed with the 30 mm thick fat mimicking layer were further reduced compared to the intensity values for the velocity data with the 20 mm fat mimicking layer. A slight positive shift in the velocity scale, in the velocities determined in presence of the 20 mm thick fat mimicking layer, was observed when compared with velocities determined without fat mimicking layer. A further positive shift in the velocities was observed in the presence of the 30 mm thick fat mimicking layer when compared to the velocities determined with the 20 mm thick fat mimicking layer. However, the positive shift was prominent only for the peak systolic velocities (48-60 cms^{-1}). In the region 2, (shown in figure 4.23), a prominent decrease in the intensity values for the velocity data for the 30 mm fat mimicking oil layer was observed compared with the intensity values for the velocity data without fat mimicking layer. A very small positive shift in the velocity scale (< 3 cms^{-1}) was observed with introduction of the fat mimicking oil layer. No changes in the shape of the physiological velocity waveforms were observed under the experimental conditions. Figure 4.24 shows the physiological velocity waveform captured in the 30% symmetrical stenosis renal artery flow phantom for the three experimental conditions.

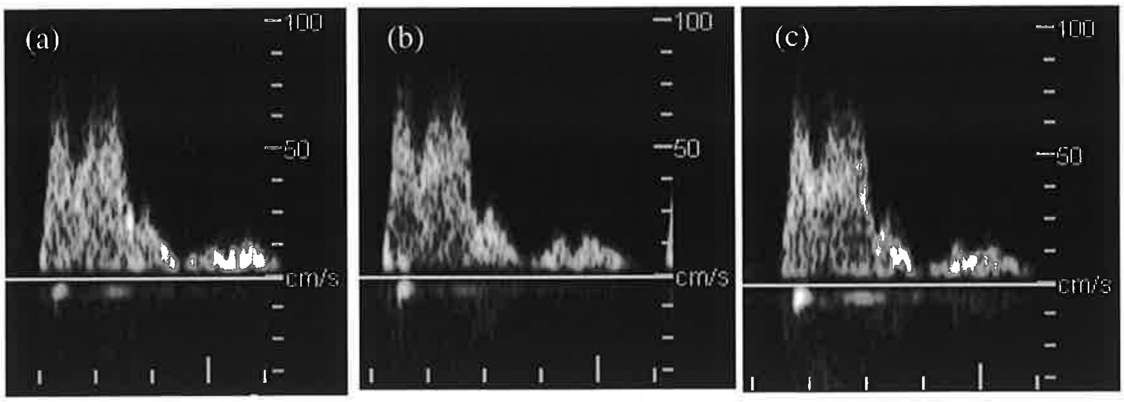

Figure 4.24 Physiological velocity waveform pictures in the 30% symmetrical stenosis renal flow phantom (a) without fat mimicking layer (b) with 20 mm thick fat mimicking layer (c) with 30 mm thick fat mimicking layer

Figure [4.25-4.26] shows intensity Vs velocity plot of the physiological velocity waveforms observed under the three experimental conditions, in the 30% symmetrical stenosis renal artery flow phantom, for region 1 and region 2.

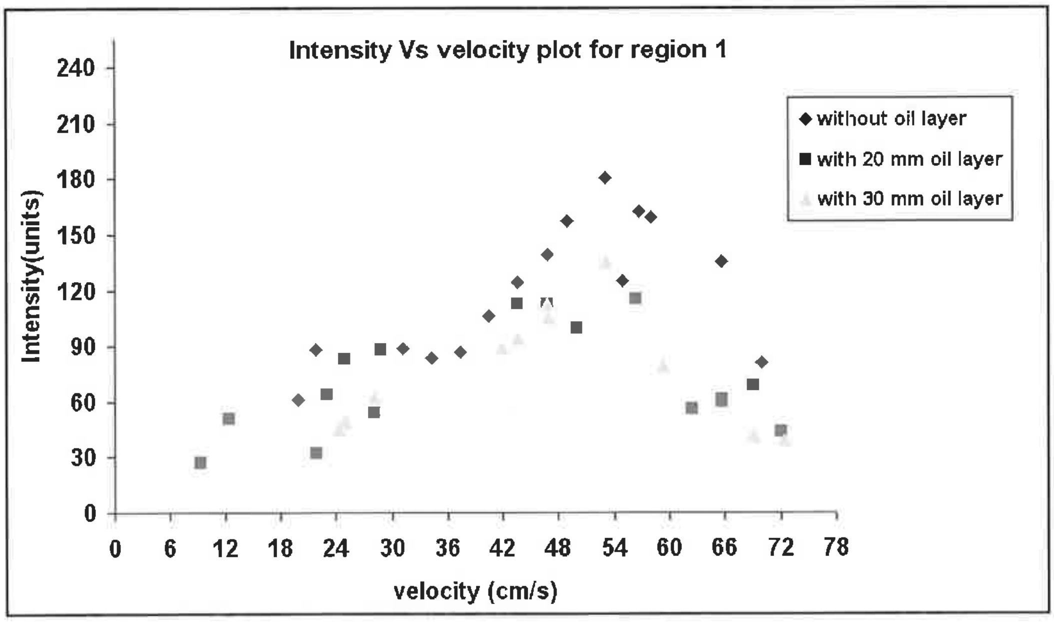

Figure 4.25 Intensity Vs Velocity plot in region 1 of physiological velocity waveforms observed in the 30% symmetrical stenosis renal artery flow phantom

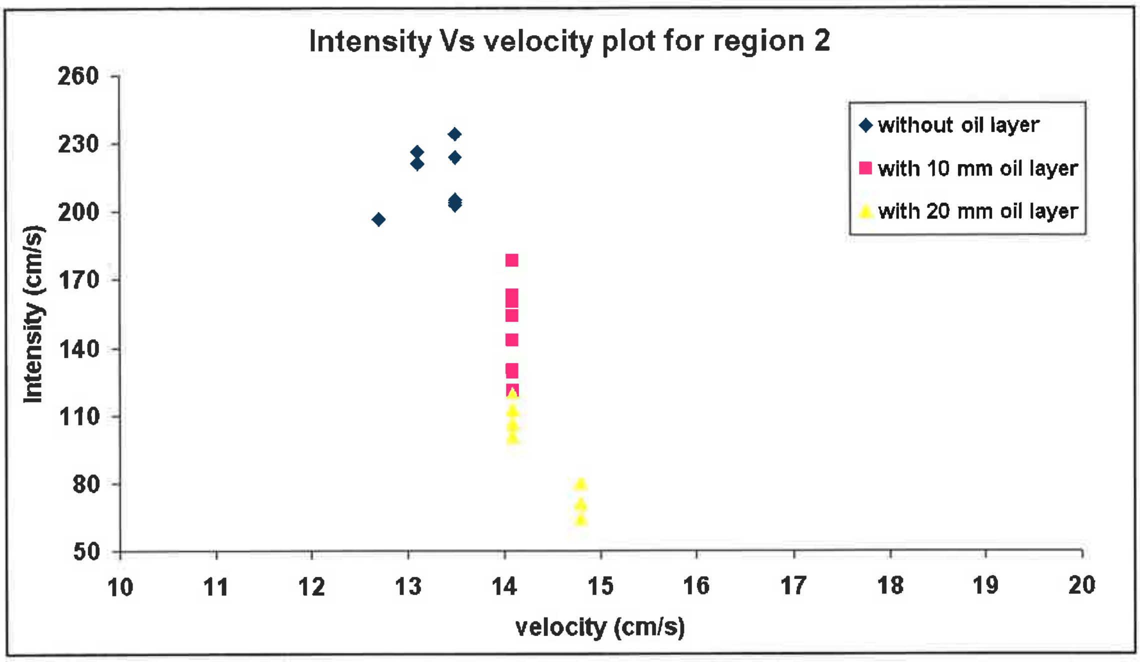

Figure 4.26 Intensity Vs Velocity plot in region 2 of the physiological velocity waveforms observed in the 30% symmetrical stenosis renal artery flow phantom

In the intensity versus velocity plot of physiological velocity waveform observed in the 30% asymmetrical stenosis renal artery flow phantom, for region 1, a similar trend of decrease in the intensity values of the velocity data was observed for the 20 mm thick fat mimicking layer compared with the intensity values of the velocity data obtained without the fat mimicking layer. A further decrease in the intensity values for the velocity data for the 30 mm thick fat mimicking layer was observed compared with the intensity values of the velocity data obtained with 20 mm fat mimicking layer. However, the intensity decrease was slightly smaller/less as compared to the intensity decrease observed in the intensity versus velocity plot for region 1 in case of normal renal artery flow phantom. For region 2, a significant decrease in the pixel intensity values of the velocity data was observed with the introduction of a fat mimicking layer of 20 mm and continued with a further prominent decrease in the intensity values of the velocity data with further increase in the thickness (by 10 mm) of the fat mimicking layer when compared with the intensity values without the fat mimicking layer. A small positive shift in the velocity scale (< 3 cms^{-1}) was also evident with the introduction of a fat mimicking layer. Further, no changes in the shape of the physiological velocity waveforms were observed under the experimental conditions.

Figure 4.27 shows the physiological velocity waveform captured in the 25% asymmetrical stenosis renal artery flow phantom for the three experimental conditions.

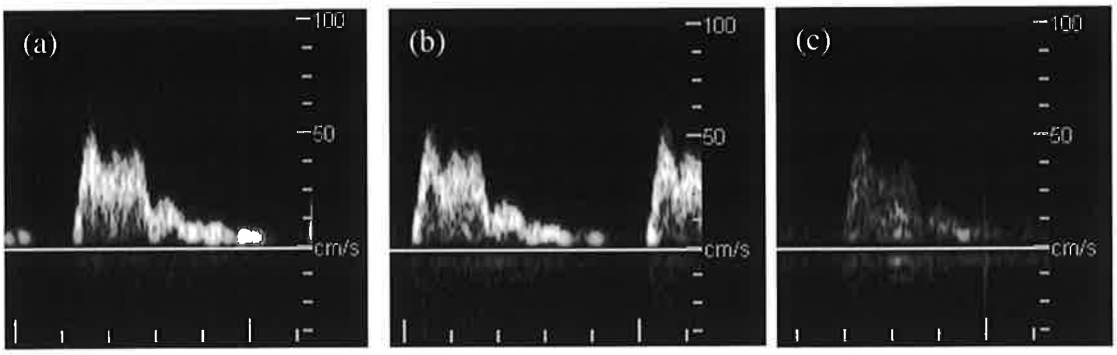

Figure 4.27 Physiological velocity waveform pictures in the 25% asymmetrical stenosis renal artery flow phantom (a) without fat mimicking layer (b) with 20 mm thick fat mimicking layer (c) with 30 mm thick fat mimicking layer

Figure 4.28 and 4.29 shows the plot of intensity versus velocity of the physiological velocity waveforms observed under the three experimental conditions; in the normal renal flow phantom, for region 1 and for region 2 respectively.

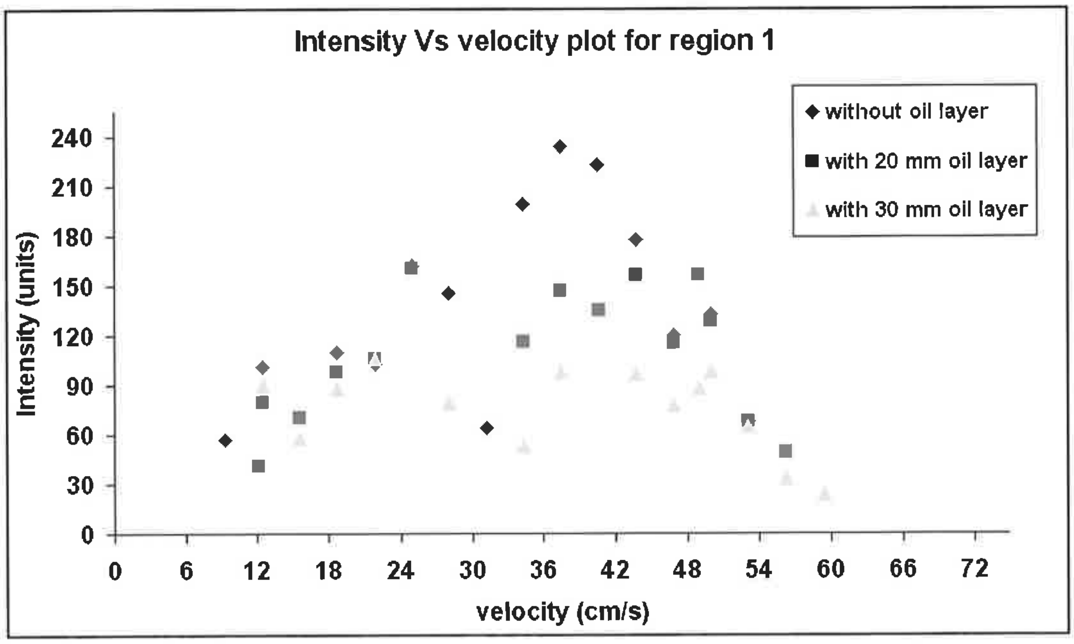

Figure 4.28 Intensity Vs Velocity plot in region 1 of the physiological velocity waveforms observed in the 25% asymmetrical stenosis renal artery flow phantom

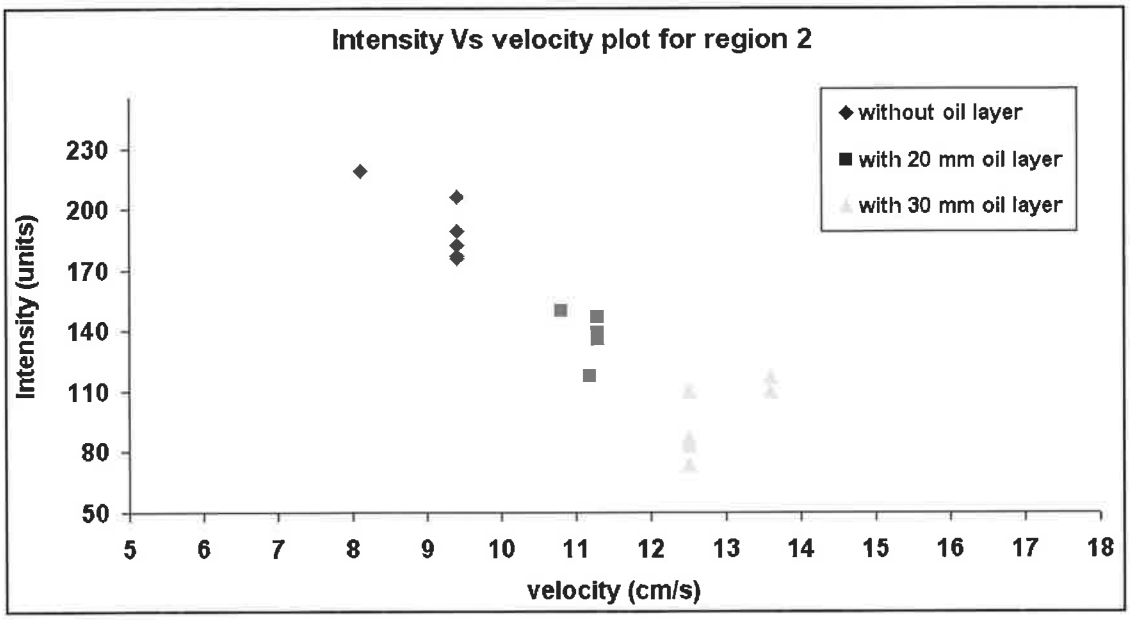

Figure 4.29 Intensity Vs Velocity plot in region 2 of physiological velocity waveforms observed in the 25% asymmetrical stenosis renal artery flow phantom

A similar trend of decrease in the intensity values of the velocity data with a fat mimicking layer compared to the intensity values of the velocity data without a fat mimicking layer was evident for region 1 and more significantly for region 2, in 25% asymmetrical stenosis renal artery flow phantom. Furthermore, no changes in the shape of the physiological velocity waveforms were observed under the experimental conditions in 25% asymmetrical stenosis renal artery flow phantom.

Chapter 5 Discussion

In this chapter the main results of the thesis are discussed. Section 5.1 discusses the results of: a) the development of the straight and the renal artery wall-less flow phantoms; and b) the basic flow experiments performed using these flow phantoms. Section 5.2 discusses the results of the physiological flow experiments in the anatomically realistic renal artery flow phantoms while section 5.3 discusses the results of the physiological flow experiments with the fat mimicking layers.

5.1 Development of the straight and the renal artery wall-less flow phantoms and the basic flow experiments

The normal and 30% symmetrical stenosis straight wall-less flow phantoms were developed following the method described by Ramnarine *et al.* [56]. These flow phantoms were constructed using an agar based TMM. The construction of the flow phantom was found to be relatively simple and the flow phantoms were found to be geometrically accurate. The geometric stability of the agar based straight wall-less flow phantoms with a varying range of stenosis was studied and the potential of these flow phantoms for steady and physiological flow experiments was reported by Ramnarine *et al.* [56]. Based on this knowledge, basic steady and physiological flow experiments were performed in the straight wall-less flow phantoms, with no stenosis and 30% symmetrical stenosis with both the steady and the physiological velocity profiles were investigated. A steady flow velocity of 40 cms^{-1} was used for the steady flow experiments and the velocity profile in normal straight wall-less flow phantom (figure 4.3) was found to be parabolic. The velocities observed were between 50 - 67 cms^{-1} with the highest velocities observed along the central axis and decreasing as a function of diameter, across the radial planes. This type of the behaviour of BMF flow in the straight wall-less flow phantom was also observed in several other experimental and theoretical studies, with this type of flow being described as having a similar behaviour to a Newtonian fluid in a simple long cylindrical rigid tube [29] [12] [17]. In a

Newtonian fluid passing through long rigid cylinder, since the volumetric flow through any cross-section is constant, the fluid layer at the center is accelerated to compensate the deceleration at the vessel walls and produces a parabolic velocity profile. The velocity profile in the 30% stenosis straight wall-less flow phantom (figure 4.3 (b)) was parabolic in nature. The velocity profile, before the stenosis region, exhibited a similar behaviour to that observed in normal straight wall-less flow phantom. At the stenosis, the velocities were found to be elevated up to 87 cms^{-1}. In the entire stenosis region, the highest velocities measured were observed along the central axis in all the radial planes which was an indication of the symmetric nature of the stenosis. The elevated velocities at the stenosis decreased rapidly in the post stenosis region and continued the parabolic flow pattern continued downstream from the stenosis. The elevated velocities at the stenosis region and their accumulation along the central axis and the rapid decrease of the velocities in the post-stenosis region indicated that the type and extent of the stenosis had an effect on the local flow characteristics of the velocity profile. The steady velocity profiles provided a basic understanding of the steady flow behaviour in the normal straight artery as well as in a stenosed straight artery. The study also indicated that the local velocity profiles in the vessel of interest would be useful to understand the flow behaviour in that vessel. The present study was focussed on understanding the flow behaviour in the normal and diseased renal artery. Therefore, the normal and diseased renal vasculature was mimicked using anatomically realistic renal artery flow phantoms. In all, seven renal artery flow phantoms representing a normal renal vessel and a range of symmetrical (30%, 50% and 70%) and asymmetrical (25%, 35% and 35%) stenosis conditions were developed and their corresponding velocity profiles were investigated by performing *in-vitro* flow experimentations in each. Before the flow experimentations were carried out, it was important to ensure that these phantoms were both acoustically and geometrically accurate, therefore both of these were investigated. The acoustic properties in terms of speed of sound and attenuation coefficient (tabulated in table 4.4) were observed to be within the recommended IEC standards for the acoustic properties of the TMM that was used in the study. The results ensured that the renal artery flow phantoms represented the renal vasculature acoustically. The p values determined from the paired t-test, performed to compare the renal artery diameter measured at two stages during the construction process, were found to be greater than 0.05 indicating that there was no statistical difference between the renal artery diameters measured at two stages of their construction. Therefore, the renal artery flow phantoms were geometrically accurate in terms of fabrication and thus mimicked the normal and diseased renal vasculature exactly.

Basic steady flow experiments were performed using the normal and 30% symmetrical stenosis renal artery flow phantoms initially. A steady velocity of 40 cms^{-1} was developed in each phantom for the flow experimentation. The steady flow velocity profile in the normal renal artery flow phantom (figure 4.4 (a)) exhibited a parabolic flow profile similar to the straight wall-less flow phantom, except with a slightly elevated velocities skewed towards the outer vessel wall at the curvature. The velocities observed in normal renal artery flow profile before and at the curvature region were in the range of 50 - 63cms^{-1} and 60 - 73 cms^{-1}, respectively. The diameter of the normal wall-less vessel in the straight wall-less flow phantom was 6.8 mm, similar to the diameter of the renal artery lumen in the anatomically realistic normal renal artery flow phantom and the steady velocity profiles in both of these phantoms were investigated using a steady velocity of 40 cms^{-1} so that a direct comparison of both the velocity profiles could be made. Comparing the steady velocity profile in the normal renal artery flow phantom with the velocity profile in the normal straight wall-less flow phantom, it was observed that that presence of bend or curvature had introduced additional effects such as skewing of the radial velocity profiles towards the outer vessel wall, at the location of the curvature.

In the 30% stenosis renal artery flow phantom, the velocity profile (figure 4.4 (b)) was again parabolic in nature with the velocities observed before the stenosis in the range of 50 - 74 cms^{-1}. At the stenosis, the velocities increased to the range of 76 - 88 cms^{-1}. The effect of the stenosis was only observed locally that is the higher velocities were concentrated only at the stenosis region and then decreased very rapidly in the post-stenosis region with the distribution of flow energy. The steady flow profile in normal and 30% symmetrical stenosis renal artery flow phantoms indicated that both the vessel geometry and the stenosis geometry had an impact on the local characteristics of the velocity profiles.

An in-depth understanding of disease progression in the renal arteries was possible by studying the velocity profiles investigated in renal artery flow phantoms with a range of symmetrical and asymmetrical stenosis. Since the physiological flow is more reflective of the clinical reality, a protocol for physiological flow experimentation in the renal artery flow phantom, which aimed to investigate the physiological velocity profiles in these phantoms, was developed. Clinical studies have indicated that the blood velocity in the renal artery of a healthy person is in the range of 2 - 60 cms^{-1}. Using this clinical information, a physiological velocity range of 2 - 60 cms^{-1} was initially used for the flow experiments. Basic physiological flow experiments were performed in the normal and the 30% stenosis straight wall-less flow phantoms and the physiological velocity profiles were investigated. The physiological velocity profile investigated in the normal straight wall-less flow phantom (figure 4.5 (a)) was flat in nature with the systolic velocities determined to be in the range of 63-75 cms^{-1}. In the 30% stenosis straight wall-less flow phantom, the physiological velocity profile (figure 4.5 (b)) was flat with the systolic velocities determined to be in the range of 63 - 75 cms^{-1}. At the stenosis, the systolic velocities were observed to be elevated up to 85 to 101 cms^{-1}. The velocities in the immediate post-stenosis region were observed in the range of 80 to 96 cms^{-1} and continued to decreased further with increasing distance from the stenosis. The physiological velocity profiles in normal straight wall-less flow phantom indicated that the basic nature of the systolic velocity profile was flat. From the profile of the 30% stenosis straight wall-less flow phantom, it was observed that the presence of stenosis had affected the physiological velocity profile at the stenosis and had also affected the flow behaviour in the post-stenosis region. In case of the renal arteries, as explained earlier, the complex renal vasculature, asymmetrical nature of stenosis and the location of the stenosis in the artery could result in complex renal velocity profiles. These complex physiological velocity profiles were investigated in renal artery flow phantoms with a range of symmetrical and asymmetrical stenosis by physiological velocity experiments. Some initial attempts to carry out the flow experiments in models with higher degrees of stenosis (50% and 70%) with physiological flow velocity between 2 - 60 cms^{-1} resulted in rupturing of the phantom at the curvature due to the high pressure developed during the physiological flow. Therefore, the physiological velocity of between 2 - 40 cms^{-1} was used for the subsequent flow experiments. An assessment of the geometric stability of the stenosis models of the renal artery flow phantoms was performed using the physiological flow velocity varying between 2 - 40 cms^{-1} with the results of the assessment of the geometrical stability of the stenosis models, supporting the use of this physiological velocity range for the flow experiments in all renal artery flow phantoms.

5.2 Physiological velocity profiles in anatomically realistic renal artery flow phantoms

The physiological velocity profile in the normal renal artery flow phantom (figure 4.6 (a)) was flat in nature and the velocities were observed to be in the range of 40 - 60 cms^{-1}. The velocities measured at the boundary walls were between 4 – 6 cms^{-1} lower compared to the velocities measured along the central region of the lumen. This was as expected as the flow near the vessel the wall would experience the boundary-induced frictional or dragging forces through interaction with the vessel walls. The velocities at the vessel curvature were slightly higher by approximately 4 - 6 cms^{-1} and skewed towards the outer vessel wall (figure 4.9 (a)) compared to the velocities in the inlet region. The higher velocities towards the outer wall at the curvature gradually decreased with the axial distance. The same general features were identified in the velocity profile of the 30% symmetrical stenosis renal artery flow phantom, apart from a small increase in the velocities of between of 63 - 76 cms^{-1} at the stenosis region, concentrated along the central axis. The increased velocities were reduced in the post stenosis region. The physiological velocity profile at the stenosis in the 30% stenosis renal artery flow phantom indicated a weak jet effect resulting in an increase in the local velocities. A slight skewing of the profile at the outer vessel wall was observed at the curvature, while further downstream to the curvature, the flat nature of the profile was resumed. There was a further increase in the velocity magnitude observed with the higher degrees of stenosis, for example in the 50% and the 70% symmetrical stenosis renal artery flow phantoms as the jet of flow became more pronounced. In the physiological velocity profile of the 50% symmetrical renal artery flow phantom, the systolic velocities were elevated to a velocity of 96 cms^{-1}, indicating a strong jet of flow. The peak systolic velocities abruptly dropped as the renal lumen resumed to its original (normal) diameter and relatively high rates of shear occurred in the narrow/ stenosed regions between the main jet and the walls in the post stenosis region. A little mixing of the flow was observed near the vessel wall in the post-stenosis region, with the velocity ranging from 60-76 cms^{-1}. The Colour Doppler image, of the inlet region of 50% symmetrical stenosis renal artery flow phantom, also indicated the presence of this mixing type of flow (figure 4.13 (c)). The skewing towards the outer vessel wall, at the curvature, was prominently observed in the physiological velocity profile of the 50% renal artery flow phantom. The skewing effect slowly reduced after approximately

24 mm axial distance further downstream (shown in figure 4.9 (c)). In case of the 70% symmetrical stenosis renal artery flow phantom, the velocities were elevated up to 140 cms^{-1} at the stenosis (figure 4.8 (d)), indicating the presence of a strong jet of flow at the stenosis. Immediately, downstream to the stenosis (figure 4.9(d)) a wide variation in the velocities in the range of 79 to 125 cms^{-1} was observed. The wide variation in the velocities indicated the presence of flow disturbances. The reverse flow and the flow disturbances were observed in the Colour Doppler image of the 70% renal artery flow phantom, shown in figure 4.13 (d). The flow remained disturbed up to an axial distance of 42 mm downstream of the stenosis as shown in figure 4.7 (a) following this the slowly flat nature of the profile was resumed. In the 30%, 50% and 70% symmetrical stenosis models of the renal artery flow phantom the highest velocities observed at the stenosis were along the central axis indicating that the stenosis developed in these phantoms were symmetric in nature. In the physiological velocity profiles in the 25% and 35% asymmetrical stenosis renal artery flow phantoms, the velocities measured at the stenosis were in the range of 51 - 66 cms^{-1} and 57 - 72 cms^{-1}, respectively. The velocities in the inlet region before the stenosis were observed in the range of 40- 60 cms^{-1} in both flow phantoms. The higher velocities at the stenosis were observed to be slightly shifted towards the outer vessel wall in both cases (figure 4.11 (a-b)). The off-axis shift in the maximum velocities at the stenosis indicated the asymmetrical nature of the stenosis. A small skewing of velocities towards the outer vessel wall at the curvature was observed in both of the velocity profiles. The colour Doppler images of the inlet of the 25% asymmetrical stenosis (figure 4.13 (e)) observed an undisturbed physiological flow at the stenosis and a small mixing type of flow immediate after the stenosis in the 35% asymmetrical stenosis renal artery flow phantom (figure 4.13 (f)). In the physiological velocity profile of the 45% asymmetric stenosis renal artery flow phantom, the velocities in the stenosis were elevated to 81 cms^{-1} and the highest velocity at the stenosis was observed to be shifted towards the outer curvature indicating the asymmetrical nature of the stenosis (figure 4.11 (c)). A flow disturbance just beyond the stenosis region was observed. An axial decay in the flow disturbance was observed regaining flat nature of the profile further downstream the curvature. The flow observed in the Colour Doppler image of the 45% asymmetrical stenosis renal artery flow phantom didn't show any signs of disturbances or mixing type of flow.

From the study of physiological velocity profiles investigated in the range of symmetrical and asymmetrical stenosis renal artery flow phantoms, it was evident that the shape and the symmetry of the stenosis of lower grades (≤ 45%) affected the flow profiles. The characteristic features such as skewing of the velocity profiles towards the outer vessel wall, in the presence of asymmetrical stenosis and the elevation in the velocities with the specific magnitudes depending upon the degree of constrictions could be used as an indicator of stenosis. These characteristics also provided an insight to quantify the degree of stenosis based on the magnitude of the velocities and to identify the morphology of the stenosis based on the skewing nature of the profiles. The disturbed flow observed in the immediate post stenosis region in the profiles, along with the flow visualisation in the Colour Doppler mode could be used as an indicator of the presence of the higher grade of stenosis.

In the physiologic flow experimentation studies, the 50% and 70% stenosis renal artery flow phantoms were observed to be rupturing due to the pressure developed by physiologic flow. Therefore, a low range of velocity of between 2-40 cms^{-1} than (2-60 cms^{-1}) observed in clinical studies, in a healthy volunteer, was used in these agar TMM renal artery flow phantoms. The konjac-carragenan gel based TMM is considerably strong than agar TMM and well characterised. While resolving the adhesion problems, this TMM could be used as a substitute to agar TMM for constructing the higher degree (> 50%) renal artery stenosis models. Also, very recently, the PVA-c vessel has been used to construct the walled renal artery flow phantoms with a range of stenosis, as high as up to 85%. The PVA-c vessel has been proven to be mechanically robust. The physiological velocities of 2 – 60 cms^{-1} could be possibly achieved in this walled renal artery flow phantoms and physiologic velocity profiles in the higher (>50%) stenosis model could then be investigated.

5.3 Investigation of the effect of a fat mimicking layer on the physiological flow profiles and the features of the physiological velocity waveforms

The physiological velocity profiles in the renal artery flow phantoms with an overlying fat mimicking layer of varying thicknesses were presented in section 4.6. In general, it was evident that, the overlying fat mimicking layer resulted in an overestimation of the systolic velocities measured in the renal artery flow phantoms. With a fat mimicking layer of 20 mm thickness, the systolic velocities were overestimated by between 5% to 12% and 5% to 13 %, in the normal and 30%

symmetrical stenosis renal artery flow phantoms respectively, in comparison with the systolic velocities measured without a fat mimicking layer. In the 50% symmetrical stenosis renal artery flow phantoms, with an overlying fat layer of a) 20 mm and b) 30 mm thickness, the overestimation in the systolic velocities was measured to be between 4% to 13% and 4% to 17%, respectively compared to the velocities measured without fat mimicking layer. In the case of the 70% symmetrical stenosis renal artery flow phantom, with the overlying fat mimicking layer of 20 mm and 30 mm thickness, the systolic velocities were overestimated by between 4% to 11% and 3% to 16%, respectively. A similar trend of overestimation was observed in the 70% symmetrical stenosis renal artery flow phantoms and the 25%, 35% and 45% asymmetrical stenosis renal artery flow phantoms. An average overestimation of between 4% to 13% and 3% to 17% with the overlying fat mimicking layer of 20 mm and 30 mm thickness respectively was observed.

The subcutaneous fat layer, as explained previously in the theory and literature review chapter, causes attenuation of the ultrasound beam, producing signal distortion, refraction effects and also introduces an error in the velocity estimation. In this study, the olive oil layer represented a simple fat mimicking layer. The fat mimicking layer closely mimicked the acoustic properties of the subcutaneous fat [25]. The anatomically realistic renal artery flow phantoms, as explained earlier, mimicked the renal vasculature acoustically and geometrically. Therefore, the renal artery flow phantoms with the overlying fat mimicking layer represented the *in-vivo* situation more closely. The magnitude of the error in the velocity estimation, introduced by the fat mimicking layer of varying thicknesses, was estimated in the renal artery flow phantoms. Given overestimations reaching up to 13% and 17% for 20 mm and 30 mm thick fat mimicking layers, it is clear that the presence of fat layer produces a non-negligible effect and the magnitude of the error in the velocity estimation significantly increases with the thickness of fat mimicking layer. Consequently, in clinical investigations, the presence of subcutaneous fat could therefore be expected to lead to an overestimation of the systolic velocities measured and thereby could be expected to overestimate the degree of renal artery stenosis than is actually present. This could have a serious impact in the patient management as the decision to forward patients for renovascularisation is largely based on the estimation of the degree of stenosis. The knowledge of the magnitude of such an error in the velocity estimation in presence of fat layer is therefore an important consideration during the clinical investigations.

The effect of the fat mimicking layer on the shape and profile of the physiological Spectral Doppler waveform was also investigated. The analysis of the physiological Spectral Doppler waveforms captured with and without the fat mimicking layer in: a) the normal, b) the 30% symmetrical stenosis and c) the 25% asymmetrical stenosis renal artery flow phantoms was presented in section 4.7. A comparison of the intensity versus velocity plots was obtained for the three experimental conditions in two regions: a) region 1- peak stenosis region and b) region 2- diastolic velocities region.

In region 1, a noticeable/prominent decrease in the pixel intensity values for the velocity data with the introduction of fat mimicking layer of 30 mm thickness was evident in all three renal artery flow phantoms mentioned above, while the decrease in the pixel intensity with the introduction of the fat mimicking layer 20 mm thickness was observed prominently in two renal artery flow phantoms mainly namely i) normal and 2) 25% asymmetrical stenosis renal artery flow phantom. Nevertheless, in all the three renal artery flow phantoms a decrease in the pixel intensity values of the velocity data with introduction of fat mimicking layer was evident in region 1. Further, in region 1, a positive shift in the velocity scale was observed with both the 20 mm and the 30 mm thickness fat mimicking layer in all three renal artery flow phantoms mentioned above.

In region 2, a significant decrease in the pixel intensity was observed with the fat mimicking layer of 20 mm as well as with the 30 mm fat mimicking layer in normal, 30% symmetrical and 25% asymmetrical renal artery flow phantoms. The decrease in the intensity values represented the attenuation of ultrasound waves in presence of fat mimicking layer. The significant decrease in the intensity scale with the overlaying fat mimicking layer observed in region 2 indicated that the diastolic velocities were attenuated more/prominently in presence of the fat mimicking layer.

The interaction of ultrasound with RBCs results in a weak signal. The presence of subcutaneous fat further attenuates the weaker signal and therefore significant clinical information could be lost which is an important clinical consideration. The shape of the Spectral Doppler waveforms in the normal renal artery flow phantom, with and without oil was compared and no variation in the shape was observed. The shape of the spectral Doppler waveform was expected to shift as a result of the difference in the speed of sound of the TMM and the fat mimicking oil layer. A computer algorithm for shape detection would be useful to study the shape differences if any.

An ultrasound beam propagating through the different tissue layers in the body undergoes frequency dependent attenuation. The attenuation reduces the signal amplitude and affects the quality of the image produced. The overlying fat mimicking layer and the TMM in the renal artery flow phantoms both attenuated the ultrasound beam which was clearly observed from all intensity versus velocity plots. The fat layer, as explained in the theory and literature review section, could cause refraction effects, signal distortion, errors in Doppler angle measurement and lead to error in the velocity measurement and thereby could lead to changes in the shape of the spectral Doppler waveform. The offline analysis of the Spectral Doppler waveform in the renal artery flow phantoms proved useful to gain an understanding about the frequency dependent attenuation and its effect on the shape and profile of the spectral Doppler waveform. The study of the physiological velocity profiles with an overlying fat layer and the Spectral Doppler waveform analysis was useful to gain an understanding of some aspects of the impact of subcutaneous fat in renal imaging.

The olive oil used in the study is homogenous and mimicked a simple fat layer in the body. The subcutaneous fat is more complicated in nature consisting of fat globules or cushions and has uneven thicknesses. A subcutaneous pig fat layer would closely mimic this inhomogeneous nature of fat. The pig fat has been reported to have a speed of sound of 1426 $ms^{-1}$and attenuation of 3 dB cm^{-1} at 2 MHz at 37°C in *in-vivo* and *in-vitro* conditions [77]. An extension of this work investigating the effect of such an inhomogeneous fat layer on the physiological flow profiles and Spectral Doppler waveform would be even more representative of the in-vivo situation and would possibly reveal other changes to the Spectral Doppler waveform.

Chapter 6 Conclusions and recommendations for future work

In this project the physiological velocity profiles in anatomically realistic renal artery flow phantoms with a range of symmetrical and asymmetrical stenoses were investigated. These renal artery flow phantoms closely mimicked the *in-vivo* situation. From the physiological flow experiments using these flow phantoms, the knowledge of changes in the systolic velocity measurements and the physiological velocity profiles in the presence of stenosis of different types and degrees was obtained. From these studies, an in-depth understanding of the renal flow behaviour in healthy and diseased conditions was obtained. The magnitude of change in the systolic velocity measurements and velocity profile characteristics in presence of the lower degree stenosis indicated that the systolic velocity profiles can be effectively used to detect the stenoses of lower grades. An early diagnosis of RAS could offer enough time to carry out various drug treatments which are less or non-invasive and thereby reducing risks involved in the surgery.

The effect of the overlying fat mimicking layer on the measured systolic velocities and on the shape and profile of spectral Doppler waveforms was studied. An overlying fat mimicking layer of 20 mm and 30 mm thicknesses resulted in an overestimation of systolic velocities of up to 13% and 17% respectively, in comparison with the systolic velocities measured without fat mimicking layer in anatomically realistic renal artery flow phantoms. The analysis of Spectral Doppler waveform profiles revealed a decrease in the pixel intensity scale with increasing thickness of the fat layer. A positive shift in the velocity scale of both systolic as well as diastolic velocities was also observed. This study has demonstrated that the presence of subcutaneous fat can cause increased complexities in renal imaging by affecting the accuracy in the velocity measurement as well as the features of the spectral Doppler waveforms which may affect the important clinical information used in the diagnosis of RAS.

In conclusion, the work presented in this thesis has contributed to the understanding of the complex flow behaviour in the normal and diseased renal arteries and the effect of varying thicknesses of fat mimicking layers on the measured physiological velocity profiles and the Spectral Doppler waveforms which may be useful while defining the physiological velocity profiles and Spectral Doppler waveforms as clinically important criteria for RAS investigation.

Following from the physiological flow experimentations in the anatomically realistic wall less renal artery flow phantoms with higher (greater than 50 %) degree of stenosis, replacement of the agar based TMM with a more robust TMM or use of vessel mimicking material is recommended. The use of Konjac-cargeenan TMM and PVA-c vessel in the renal artery flow phantoms is suggested while performing the physiological flow experiments. The physiological velocity profiles in such phantoms can then be investigated by mimicking the exact physiological velocities (that are measured in a healthy volunteer) in these phantoms.

Also following from the studies investigating the effect of fat layer on physiological velocity profiles, further understanding in this area can be obtained by repeating the physiological flow experiments in renal artery flow phantoms while using subcutaneous pig fat.

References

1. *Renal Artery Stenosis.* **Safian, R D, Textor S C.** 6, 2001, N Engl J Med, Vol. 344, pp. 431-442.
2. *The utility of duplex ultrasound scanning of the renal arteries for diagnosing significant renal artery stenosis.* **Olin J W, Piedmonte M R, Young J R.** 1995, Ann Intern Med, Vol. 122, pp. 833-838.
3. *Diagnosis and treatment of renovascular stenosis- a cost-benefit analysis.* **Radermacher J, Brunkhorst R.** 1998, Nephrol Dial Transplant, Vol. 13, pp. 2761-2767.
4. *Imaging Modalities for Renal Artery Stenosis in Suspected Renovascular Hypertension: Prospective Intraindividual Comparison of Color Doppler US, CT Angiography, Gd-Enhanced MR Angiography, and Digital Substraction Angiography.* **Rountas, C, Vlychou, M, Vassiou, K, Liakopoulos, V, Kapsalaki, E, Koukoulis, G, Fezoulidis, I V and Stefanidis, I.** 3, 2007, Ren Fail, Vol. 29, pp. 295-302.
5. *Using Doppler Sonography to reveal Renal Artery Stenosis: An evaluation of optical imaging parameters.* **House M K, Dowling R J, King P, Gibson R N.** september 1999, AJR, Vol. 173, pp. 761-765.
6. *Assessment of Renal Artery Stenosis: Side-by-Side Comparison of Angiography and Duplex Ultrasound with Pressure Gradient Measurements.* **Drieghe, B, Madaric, J, Sarno, G, Manoharan, G, Bartunek, J, Heyndrickx, G R, Pijls, N H and De Bruyne, B.** 4, 2008, Eur Heart J, Vol. 29.
7. *Renal Artery Stenosis: Comparative Evaluation of Gadolinium-Enhanced Mra and Dsa.* **Stacul, F, Gava, S, Belgrano, M, Cernic, S, Pagnan, L, Pozzi Mucelli, F and Cova, M A.** 4, 2008, Radiol Med, Vol. 113, pp. 529-546.
8. *A Prospective Comparison of Duplex Ultrasonography, Captopril Renography, Mra, and Cta in Assessing Renal Artery Stenosis.* **Eklöf, H, Ahlstrom, H, Magnusson, A, Andersson, L G, Andren, B, Hagg, A, Bergqvist, D and Nyman, R.** 8, 2006, Acta Radiol, Vol. 47, pp. 764-774.
9. *Renal Artery Duplex Ultrasonography as a Screening and Surveillance Tool to Detect Renal Artery Stenosis: A Comparison with Current Reference Standard Imaging.* **Soares, G M, Murphy, T P, Singha, M S, Parada, A and Jaff, M.** 3, 2006, J Ultrasound Med, Vol. 25, pp. 293-298.
10. *Comparative Accuracy of Renal Duplex Sonographic Parameters in the Diagnosis of Renal Artery Stenosis: Paired and Unpaired Analysis.* **Williams, G J, Macaskill, P, Chan, S F, Karplus, T E, Yung, W, Hodson, E M and Craig, J C.** 3, 2007, AJR Am JRoentgenol, Vol. 188, pp. 798-811.
11. *Blood velocity profiles in the Human Renal Artery by Doppler Ultrasound and Their Relatioship to Atherosclerosis.* **Yamamoto, T, Ogaswara,Y, Kimura, A, Tanaka, H, Hiramatsu, O, Tsujioka, K, Lever, J, M, Parker, K, H, Jones J, H, Caro, C, G, Kajiya, F.** 1996, Arteriosclerosis, Thrombosis and Vascular Biology, Vol. 16, pp. 172-177.

12. **Lieber B B, Sadasivan C.** Hemodynamics, Macrocirculatory. [ed.] Bowlin G. I. Wnek G. E. *Encyclopedia of Biomaterials and Bioengineering.* 2. s.l. : Informa Healthcare USA, Inc., 2008, Vol. 1, pp. 1356-1367.

13. *Assessment of the effect of vessel curvature on Doppler measurements in steady flow.* **Balbis, S, Guiot, C, Roatta, S, Arina, R, Todros, T.** 5, 2004, Ultrasound Med Biol, Vol. 30, pp. 639-645.

14. *The effect of arterial curvature on Doppler velocity blood flow waveform indices.* **Myers L, Capper, W, L.** Chicago : Proceedings of 22nd Annual EMBS International Conference, 2000 (July 23-28).

15. *Numerical studies of physiological pulsatile flow through constricted tube.* **Liao W, Lee T S, Low H T.** 5, 2004, International Journal of Numerical Methods for Heat & Fluid Flow, Vol. 14, pp. 689-713.

16. *Review of the Design and Use of Flow Phantoms In Hoskins, P R, Evans, J A and Sheriff, S (Eds) Testing of Doppler Ultrasound Equipment, IPEM.* **Hoskins, P R.** York : s.n., 1994, pp. 12-29.

17. *Simulation and Validation of Arterial Ultrasound Imaging and Blood Flow.* **Hoskins, P R.** 5, 2008, Ultrasound Med Biol, Vol. 34, pp. 693-717.

18. **D, King.** *Development of renal phantoms for the evaluation of current and emerging ultrasound technology.* School of Physics, Dublin Institute of Technology. 2009. PhD Thesis.

19. *Renal Artery Duplex Ultrasonography as a Screening and Surveillance Tool to Detect Renal Artery Stenosis: A Comparison with Current Reference Standard Imaging.* **Soares, G M, Murphy, T P, Singha, M S, Parada, A and Jaff, M.** 3, 2006, J Ultrasound Med, Vol. 25, pp. 293-298.

20. *The Effect of Refraction and Assumed Speeds of Sound in Tissue and Blood on Doppler Ultrasound Blood Velocity Measurements.* **Christopher, D A, Burns, P N, Hunt, J W and Foster, F S.** 2, 1995, Ultrasound Med.Biol, Vol. 21, pp. 187-201.

21. *Accuracy of Maximum Velocity Estimates made Using Doppler Ultrasound Systems.* **Hoskins, P R.** 818, 1996, Br.J.Radiol., Vol. 69, pp. 172-177.

22. *Effect of Tank Liquid Acoustic Velocity on Doppler String Phantom Measurements.* **Goldstein, A.** 3, 1991, J. Ultrasound Med., Vol. 10, pp. 141-148.

23. *Sources of Error in Maximum Velocity Estimation Using Linear Phased-Array Doppler Systems with Steady Flow.* **Steinman, A H, Tavakkoli, J, Myers, J G, Jr., Cobbold, R S and Johnston, K W.** 5, 2001, Ultrasound Med.Biol, Vol. 27, pp. 655-664.

24. *How Fat Layers affect the Clinical Diagnosis obtained from Doppler Data?* **King, D, K, Moran C, M, Hussey, M, Browne, J, E.** New York, USA : s.n., 2007 (28-31Oct). IEEE Ultrasonics Symposium.

25. *Investigation of the Effect of Subcutaneous Fat on Image Quality Performance of 2D Conventional Imaging and Tissue Harmonic Imaging.* **Browne, J E, Watson, A J, Hoskins, P R and Elliott, A T.** 7, 2005, Ultrasound Med Biol, Vol. 31, pp. 957-964.

26. **Evans, D H and McDicken, W N.** *Doppler Ultrasound: Physics, Instrumental, and Clinical Applications.* s.l. : Wiley, 2000. ISBN 0-471-97001-8.

27. *Colour Ultrasound Imaging of Blood Flow and Tissue Motion.* **Hoskins, P R and McDicken, W N.** 837, 1997, Br.J.Radiol., Vol. 70, pp. 878-890.

28. *Color Flow Mapping.* **Ferrara, K and DeAngelis, G.** 2, 1997, Ultrasound Med.Biol., Vol. 23, pp. 321-345.

29. *Blood Flow in Arteries.* **Ku, D N.** 1997, Annu. Rev. Fluid. Mech., Vol. 29, pp. 399-434.

30. *Blood platelets are concentrated near the wall and redblood cells, in the centre of flowing blood.* **Aarts PAMM, van der Broek SAT, Prins, G, W, Kulken GDC, Sixma J J,Heethar, R, M.** 1988, Arteriosclerosis, Vol. 8, pp. 819-824.
31. *Oscillatory Flow in Arteries: the Constrained Elastic Tube as a Model of Arterial Flow and Pulse Transmission.* **Womersely, J, R.** 1957, Phys. Med. Biol, Vol. 2, pp. 178-187.
32. *Accuracy of Computed Tomographic Angiography and Magnetic Resonance Angiography for Digonising Renal Artery Stenosis.* **Vasbinder, G B, Nelemans, P J, Kessels, A G, Kroon, A A, Maki, J H, Leiner, T, Beek, F J, Korst, M B, Flobbe, K, de Haan, M W, van Zwam, W H, Postma, C T, Hunink, M G, de Leeuw, P W and van Engelshoven, J M.** 9, 2004, Ann.Intern.Med, Vol. 141, pp. 674-682.
33. *Clinical Role of Non-Contrast Magnetic Resonance Angiography for Evaluation of Renal Artery Stenosis.* **Utsunomiya, D, Miyazaki, M, Nomitsu, Y, Komeda, Y, Okigawa, T, Urata, J and Yamashita, Y.** 10, 2008, Circ J, Vol. 72, pp. 1627-1630.
34. *Contemporary Imaging Techniques for the Diagnosis of Renal Artery Stenosis.* **Leiner, T, de Haan, M W, Nelemans, P J, van Engelshoven, J M and Vasbinder, G B.** 11, 2005, Eur. Radiol, Vol. 15, pp. 2219-2229.
35. *Spiral Ct Angiography of Renal Arteries: Comparison with Angiography Eur Radiol,.* **Wittenberg G, Kenn W, Tschammler A, Sandstede J and Hahn D.** 3, 1999, Eur Radiol, Vol. 9, pp. 546-551.
36. *Gadolinium-enhanced magnetic resonance angiography in renal artery stenosis: comparison with digital subtraction angiography.* **Law, Y, M, Tay, K, H, Gan, Y, U, Cheah, F, K, Tan, B, S.** 2008, Hong Kong Med J, Vol. 14, pp. 136-141.
37. *Adverse Reactions to Gadolinium contrast media, A review of 36 cases.* **Murphy, K, J, Brunberg, J, A, Cohan, R, H.** 1996, AJR, Vol. 167, pp. 847-849.
38. *Nephrogenic systemic fibrosis: a serious late adverse reaction to gadodiamide.* **Thomsen, H, K.** 2006, Eur Radiol , Vol. 16, pp. 2619–2621.
39. *Nephrogenic Systemic Fibrosis: Suspected Causative Role of Gadodiamide Used for Contrast-Enhanced Magnetic Resonance Imaging.* **Marckmann, P, Skov, L, Rossen, K, Dupont, A, Damholt, M B, Heaf, J G and Thomsen, H S.** 9, 2006, J Am Soc Nephrol, Vol. 17, pp. 2359-2362.
40. *Acc/Aha 2005 Practice Guidelines for the Management of Patients with Peripheral Arterial Disease (Lower Extremity, Renal, Mesenteric, and Abdominal Aortic): A Collaborative Report from the American Association for Vascular Surgery/Society for Vascular Sur.* **Hirsch, A T, Haskal, Z J, Hertzer, N R, Bakal, C W, Creager, M A, Halperin, J L, Hiratzka, L F, Murphy, W R, Olin, J W, Puschett, J B, Rosenfield, K A, Sacks, D, Stanley, J C, Taylor, L M, Jr., White, C J, White, J, White, R A, Antman, E M, Smith, S C, Jr.** 11, 2006, Circulation, Vol. 113, pp. e463-654.
41. *Update of Renal Imaging.* **Grenier, N, Hauger, O, Cimpean, A and Perot, V.** 1, 2006, Semin.Nucl.Med., Vol. 36, pp. 3-15.
42. *Role of Duplex scanning for the detection of atherosclerotic renal artery disease, Kidbey Int.* **Hoffmann, U, Edwards, JM, Carter, S, Goldman ML, Harley, J D, Zaccardi, M J, Strandness, D E.** 1991, Ultrasound Med Biol, Vol. 39, pp. 1232-1239.
43. *Colour Doppler Ultrasound: a new index improves the diagnosis of renal artery stenosis.* **Souza de Oliveria, I, Widman A, Lazlo, J, Fukushima, J, Praxedes, J, Cerri, G.** 2000, Ultrasound Med Biol, Vol. 26, pp. 41-47.
44. *Duplx scan sonography of renal artery stenosis.* **Rabbia, C, Valpreda, S.** 2, 2003, Int Angiol., Vol. 22, pp. 101-115.

45. *Diagnostic role of new Doppler index in assessment of renal artery stenosis.* **Chain, S, Luciardi, H, L, Feldman, G, Berman, S,G, Herrera, R,N, Ochoa, J, Muntaner, J, Escudero, E,M, Ronderos, R.** 4, 2006, Cardiovascular Ultrasound, Vol. 4, pp. 1-24.
46. *Evaluation of renal artery stenosis with hemodynamic parameters of Doppler Sonography.* **Li, J C, Jiang, Y X, Zhang, S,Y, Wang, L, Ouyang, Y, S, Qi, Z, H.** 2, 2008, J Vascular Surgery, Vol. 48, pp. 322-328.
47. *Evaluation of Renal Artery Stenosis with Velocity Parameters of Doppler Sonography.* **Li, J C, Wang, L, Jiang, Y X, Dai, Q, Cai, S, Lv, K and Qi, Z H.** 6, 2006, J Ultrasound Med, Vol. 25, pp. 735-742. quiz43-44.
48. *IPEM (2004) Vascular Laboratory Practise Manual IPEM.* York : s.n., 2004.
49. *IEC (2001) Ultrasonics - Flow Measurement Systems: Flow Test Object International Electrotechnical Commission.* Geneva, Switzerland : s.n.
50. *Anatomical Flow Phantoms of the Nonplanar Carotid Bifurcation, Part Ii: Experimental Validation with Doppler Ultrasound.* **Meagher, S, Poepping, T, L, Ramnarine, K V, Black, R, A and Hoskins, P, R.** 2, 2007, Ultrasound Med Biol, Vol. 33, pp. 302-310.
51. *Development of an Example Flow Test Object and Comparison of Five of These Test Objects, Constructed in Various Laboratories.* **Teirlinck, C J, Bezemer, R A, Kollmann, C, Lubbers, J, Hoskins, P, R, Ramnarine, K V,Fish, P, Fredeldt, K E and Schaarschmidt, U G.** 1-5, 1998, Ultrasonics, Vol. 36, pp. 653-660.
52. *Liquid or Solid Ultrasonically Tissue-Mimicking Materials with Very Low Scatter.* **Madsen, E L, Frank, G R and Dong, F.** 4, 1998, Ultrasound Med Biol, Vol. 24, pp. 535-542.
53. *Physical Properties of Tissues Relevant to Arterial Ultrasound Imaging and Blood Velocity Measurement.* **Hoskins, P R.** 10, 2007, Ultrasound Med Biol, Vol. 33, pp. 1527-1539.
54. *A simple tissue-like ultrasound phantom material.* **Lerski, A, R, Duggan, T, C, Christie, J.** 1982, Br.J.Radiol, Vol. 15, pp. 87-94.
55. *A Wall-Less Vessel Phantom for Doppler Ultrasound Studies.* **Rickey, D W, Picot, P A, Christopher, D A and Fenster, A.** 9, 1995, Ultrasound Med Biol, Vol. 21, pp. 1163-1176.
56. *Construction and Geometric Stability of Physiological Flow Rate Wall-Less Stenosis Phantoms.* **Ramnarine, K V, Anderson, T and Hoskins, P R.** 2, 2001, Ultrasound Med Biol, Vol. 27, pp. 245-250.
57. *Assessment of the Acoustic Properties of Common Tissue-Mimicking Test Phantoms.* **Browne, J E, Ramnarine, K V, Watson, A J and Hoskins, P R.** 7, 2003, Ultrasound Med Biol, Vol. 29, pp. 1053-1060.
58. *Poly(Vinyl Alcohol) Cryogel Phantoms for Use in Ultrasound and MR Imaging.* **Surry, K J, Austin, H J, Fenster, A and Peters, T M.** 24, 2004, Phys Med Biol, Vol. 49, pp. 5529-5546.
59. *Performance tests of Doppler ultrasound equipment with a tissue and blood mimicking phantom.* **Boote, E, J, Zagzebski, J,A.** 1988, Ultrasound Med Biol, Vol. 7, pp. 137-147.
60. *On the Design and Evaluation of a Steady Flow Model for Doppler Ultrasound Studies.* **Law, Y F, Johnston, K W, Routh, H F and Cobbold, R S.** 5, 1989, Ultrasound Med Biol, Vol. 15, pp. 505-516.
61. *A geometrically accurate vascular phantom for comparative studies of x-ray, ultrasound, and magnetic resonance vascular imaging: Construction and geometrical verification.* **Frayne R, Gowman LM, Rickey DW, Holdsworth DW, Picot PA,**

Drangova M, Chu KC, Caldwell CB, Fenster A, Rutt BK. 1993, Med Phys, Vol. 20, pp. 415-425.

62. *Design and Characterisation of a Wall Motion Phantom.* **Dineley, J, Meagher, S, Poepping, T L, McDicken, W N and Hoskins, P R.** 9, 2006, Ultrasound Med Biol, Vol. 32, pp. 1349-1357.

63. *An in-Vitro System for Doppler Ultrasound Flow Studies in the Stenosed Carotid Artery Bifurcation.* **Poepping, T L, Nikolov, H N, Rankin, R N, Lee, M and Holdsworth, D W.** 4, 2002, Ultrasound Med Biol, Vol. 28, pp. 495-506.

64. *Assessmentof arterial stenosis in a flow model with power Dopplerangiography: Accuracy and observations on blood echogenicity.* **Cloutier G, Qin Z, Garcia D, Soulez G, Oliva V, Durand LG.** 2000, Ultrasound Med Biol, Vol. 26, pp. 1489-1501.

65. *A Multimodality Vascular Imaging Phantom with Fiducial Markers Visible in DSA, CTA, MRA, and Ultrasound.* **Cloutier, G, Soulez, G, Qanadli, S D, Teppaz, P, Allard, L, Qin, Z, Cloutier, F and Durand, L G.** 6, 2004, Med Phys, Vol. 31, pp. 1424-1433.

66. *Geometric Characterization of Stenosed Human Carotid Arteries.* **Smith, R F, Rutt, B K, Fox, A J, Rankin, R N and Holdsworth, D W.** 11, 1996, Acad Radiol., Vol. 3, pp. 898-911.

67. *A Thin- Walled Carotid Vessel Phantom for Doppler Ultrasound Flow Studies.* **Poepping, T L, Nikolov, H N, Thorne, M L and Holdsworth, D W.** 8, 2004, Ultrasound Med Biol, Vol. 30, pp. 1067-1078.

68. *A Real Vessel Phantom for Flow Imaging: 3-D Doppler Ultrasound of Steady Flow.* **Dabrowski, W, Dunmore-Buyze, J, Cardinal, H N and Fenster, A.** 1, 2001, Ultrasound Med Biol., Vol. 27, pp. 135-141.

69. *Experimental Flow Studies in Exact-Replica Phantoms of Atherosclerotic Carotid Bifurcations under Steady Input Conditions.* **Bale-Glickman, J, Selby, K, Saloner, D and Savas, O.** 1, 2003, J Biomech Eng, Vol. 125, pp. 38-48.

70. *Influence of Tissue Preservation Methods on Arterial Geometry and Echogenicity.* **Wilhjelm, J E, Vogt, K, Jespersen, S K and Sillesen, H.** 7, 1997, Ultrasound Med Biol., Vol. 23, pp. 1071-1082.

71. *Flow Dynamics in a stenosed carotid bifurcation model-part1:Basic velocity measurements.* **Fei D Y, Billian C, Rittgers S E.** 1, 1988, Ultrasound in Med. & Biol., Vol. 14, pp. 22-31.

72. *Doppler Ultrasound compatible plastic material for use in rigid flow models.* **Wong E Y, Thorne M L, Nikolov H N, Poepping T L, Holdsworth W.** 11, 2008, Ultrasound in Med. & Biol., Vol. 34, pp. 1846-1856.

73. *Testing ultrasonic pulsed Doppler instruments with a physiologic string phantom.* **Phillips, D, J, Hossack, J, Beach, K, W, Strandeness, D,E.** 8, 1990, J. Ultrasound Med., Vol. 19, pp. 429-436.

74. **Bamber, J C.** Attenuation and Aborption. [book auth.] C R, Bamber, J C and Ter Haar,G R Hill. *Physical Principles of Medical Ultrasonics.* 2. s.l. : Wiley, 1997, pp. 93-166.

75. **Duck, F A.** *Physical Properties of Tissue: A Comprehensive Reference Book.* London : Academic Press Inc, 1990.

76. *Methods for specifying acoustic properties of tissue mimicking phantoms and objects.* s.l. : American Institute of Ultrasound in Medicine, 1990. Stage I. AIUM, Laurel.

77. *In-Vivo Ultrasonic measurements of tissue properties.* **Lewin P A, Busk H.** 1982. Preceedingin of the IEEE Ultrasonics Symposium. p. 3.

78. **Quaia, E.** *Physical Basis and Principles of Action of Microbubble-Based Contrast Agents In Contast Media in Ultrasonography: Basic Principles and Clinical Applications.* Berlin Heidelberg New York : Springer, 2005.
79. *Effect of curvature and stenosis on wall shear stress patterns in coronary artery model with phasic flow.* **Nosovitsky, V, A, Ilegbusi, O, J, Jiang, J, Stone, P, H, Feldman, C,L.** 1995, Computers in cardiology, pp. 685-688.
80. *Choice of moving target for a string phantom: II. On the performance testing of Doppler ultrasound systems.* **Hoskins, P, R.** 8, 1994(a), Ultrasound Med Biol, Vol. 20, pp. 781-789.
81. *Flow dynamics in a stenosed carotid bifurcation model- part I: Basic flow measurements.* **Fei, D,Y, Billian, C, Ritgers, S, F.** 1, 1988, Ultrasound Med Biol., Vol. 14, pp. 21-33.
82. *Renal Artery Stenosis: Value of Contrast-EnhancedUltrasonography.* **Drelich-Zbroja, A, Jargiello, T, Drelich, G, Lewandowska-Stanek, H and Szczerbo-.** 4, 2004, Abdom.Imaging, Vol. 29, pp. 518-524.
83. *The Kidney: Imaging with Microbubble Contrast Agents.* **Correas, J M, Claudon, M, Tranquart, F and Helenon, A O.** 1, 2006, Ultrasound, Vol. 22, pp. 53-66.
84. *Guidelines for Contrast Enhanced Ultrasound (CEUS)--Update 2008.* **Correas, J M, Tranquart, F and Claudon, M.** quiz 39-40, 2009, J Radio.l, Vol. 90(1 Pt 2).
85. *Duplex Imaging and Renal Artery Stenosis.* **Beattie, D K, Golledge, J, Cuming, R, Greenhalgh, R M and Davies, A H.** 1997, Journal of Vascular Investigation, 3(1), 9.
86. *A Prospective Comparison of Duplex Ultrasonography, Captopril Renography, MRA, and CTA in Assessing Renal Artery Stenosis.* 2006, **Eklöf, H, Ahlstrom, H, Magnusson, A, Andersson, L G, Andren, B, Hagg, A, Bergqvist, D and Nyman, R** Acta Radiol,47(8), 764-774.
87 *Frequency of severe renal artery stenosis in patients with severe thoracic aortic plaque.* **H. Reynolds,H, Tunick,P, Benenstein, R, Nakra,N, Shah,A, Spevack,D, Kronzon,I.** The American Journal of Cardiology, Vol.94(6), pp 844-846.
88. *Correction of Intrinsic Spectral Broadening Errors in Doppler Peak Velocity Measurements Made with Phased Sector and Linear Array Transducers.* **Winkler, A J and Wu, J.** Ultrasound in Med. Biol., 1995, Vol. 21(8), pp 1029-1035.
89. *Three-dimensional power Doppler imaging: a phantom study to quantify vessel stenosis.* **Guo,Z, Fenster,A.** Ultrasound in Med. Biol., 1996, Vol. 22(8), pp 1059-69.
90. *Rapid 3-D imaging of contrast flow: application in a perfused kidney phantom.* **Chen N G, Fowlkes J B, Carson P L, Schipper M J, LeCarpenter G L.** Ultrasound in Med. Biol., 1995, Vol. 35(5), pp 813-828.
91. *Advances in Ultrasound.* **Claudon M, Tranquart F, Evans D H, Lefevre F, Correas J M.** Eur. Radiol 2002, Vol 12 pp 7-18.
92. *3-D Ultrasound Imaging: A review.* **Fenster A, Downey D B**, IEEE Engineering in Med. Biol., 1996,Vol 15, pp 41-51.

Publications and presentations

List of presentations:

1. 'Investigation of velocity profile in anatomically realistic flow phantoms using Doppler ultrasound' **Deepa Chari**, Deidre King, Andrew Fagan and Jacinta Browne. Annual Scientific Meeting 2009, Association of Physical Scientists in Medicine, kilkenny, Ireland, 27 Feb 2009 (oral presentation)

2. 'An investigation of velocity profiles by physiological flow experimentation' **Deepa Chari**, Deidre King, Andrew Fagan and Jacinta Browne. Spring Weekend Meeting 2009,IOP, Waterford, Ireland, 3-5 April 2009 (poster presentation)